Electronic and magnetic properties of alkali and alkaline earth metals doped AlN: bulk to surfaces

SANDHYA CHINTALAPATI

(M.Sc; University of Hyderabad)

A THESIS SUBMITTED

FOR THE DEGREE OF DOCTOR OF PHILOSOPHY

DEPARTMENT OF PHYSICS

NATIONAL UNIVERSITY OF SINGAPORE

2015

DECLARATION

I hereby declare that the thesis is my original work and it has been written by me in its entirety. I have duly acknowledged all the sources of information which have been used in the thesis.

This thesis has also not been submitted for any degree in any university previously.

Chintalapati Sandhya

05 May 2015

Acknowledgements

I would like to express my profound gratitude to my supervisor **Prof. Feng Yuan Ping** for his professional guidance, support and encouragement throughout my research. Prof. Feng gave me an opportunity to explore my research interest and provided a lot of help and valuable suggestions during my Ph.D. It is a fortune for me to do research under the guidance of Prof. Feng and that great experience would definitely helps me in my future career.

I gratefully acknowledge Prof. Shu Ping Lau for the experimental support and earlier motivation he had provided us to start this project. I am thankful to Dr. Zhang Chun for his valuable suggestions in the group meetings. Special thanks to Dr. Shen Lei and Dr. Yang Ming for their help in the past few years. I would like to thank all my current and previous labmates for the wonderful moments and the support in several aspects: Dr. Wu Rongqin, Dr. Cai Yongqing, Dr. Zhou Miao, Dr. Bai Zhaoqiang, Dr. Zeng Minggang, Dr. Lu Yunhao, Dr. Wu Qingyun, Dr. Li Suchun, Mr. Zhou Jun, Mr. Le Quy Duong, Ms. Linghu Jiajun, Ms. Zhang Meini, Mr. Wu Di, Mr. Deng Jiawen, Mr. Luo Yongzheng, Mr. Liu Yang, Dr. Qin Qian and Ms. Ting Ting.

It is my honor to thank my masters project advisor Prof. K. P. N. Murthy for his constant encouragement in my academics. Special thanks to my friends Mr. Balagangadhar Addanki, Mrs. Lavanya Kunduru, Mrs. Sireesha Edala and Mr. Rakesh Roshan for

their incredible moral support and encouragement. I would like to thank all my friends, room mates and my meditation society people for providing me wonderful and happy moments with them.

Finally, I would like to express my deepest gratitude to my parents Rambabu and Sailaja for their love, support and care. Thanks a lot to my elder sister Mrs. Madhuri and my younger brother Mr. Siva Santosh Ravi Varma for being nice and enlightening with me from my childhood. Thanks to all my teachers, relatives and colleagues for their involvement in this wonderful journey.

I acknowledge National University of Singapore for the research scholarship, which makes my research activities smooth and enables me to finish my thesis.

Table of Contents

Summary

The fascinating discovery of room temperature ferromagnetism in non-magnetic elements doped semiconductors grabbed the researchers′ attention in recent years for potential spintronic applications. However, the origin and mechanism of ferromagnetism in non-magnetic element doped semiconductors remain under debate over many years and constrain its applications. Especially, in the view of miniaturization of devices, various experimental studies rely on low-dimensional systems of semiconductors such as nanowires, thin films and surfaces/interfaces etc. Nevertheless, the nature and origin of magnetism are unclear at the low-dimension of non-magnetic element doped semiconductors. The theoretical aspect of magnetism in this direction is limited and requires a great attention in identifying the capability of non-magnetic element doped semiconductors for practical applications.

In order to identify the origin and magnetic phenomena in non-magnetic element doped semiconductors especially at the low-dimension, I have considered the largest wide band gap semiconductor AlN as a prototype material, and investigated the mechanism of magnetism of various alkali and alkaline earth metals doped AlN from bulk to low-dimension such as different surfaces using first-principles calculations. The focus my systematic investigation is to understand the electronic and magnetic properties of Mg doped AlN

from bulk to different surfaces such as non-polar, polar and semi-polar surfaces. The hole introduced by Mg doping in the substitution of Al, results in a magnetic moment of $1\ \mu B$. The magnetic moments are mainly localized on N atoms surrounding Mg (Mg-N cluster). Interestingly, the magnetic interaction between Mg-N clusters always favors ferromagnetic ground state from bulk to any surface orientation of Mg doped AlN. The existence of virtual charge hopping between partially filled minority spin states of Mg-N clusters, stabilizes the ferromagnetism from bulk to different surfaces of Mg doped AlN. However the stability of ferromagnetism has been changed from one surface to another surface due to various surface effects. The interplay among different factors such as localization of magnetic moments, energy level splitting and the hopping interaction between Mg-N clusters is analyzed systematically in each surface orientation to understand the variation in the stability of ferromagnetism. In most of the surfaces, ferromagnetic state is found to be more stable than antiferromagnetic state with an energy difference greater than the thermal energy at room temperature. The present results strongly support the robust nature of ferromagnetism and the prospect of room temperature ferromagnetism in bulk as well as at the low-dimension of Mg doped AlN. Furthermore, the study of surface magnetism of Mg doped AlN paves a way to attain a strong ferromagnetism in Mg doped AlN by tuning the surface effects.

The proposed mechanism of magnetism in Mg doped AlN has been successfully extended for the other alkali and alkaline earth metals doped AlN systems such as Be and K doped AlN systems, and analyzed the nature of magnetism in those systems from bulk to different surface orientations. The magnetism in Be doped AlN is not an intrinsic property and it is identified as the surface effect. In case of K doped AlN, even though

ferromagnetic ground state is observed at the surface of K doped AlN, the formation energy of doping K in AlN is found to be high. Unlike the other dopants, the observation of lower formation energies and the robust nature of ferromagnetism in Mg doped AlN indicate the capability of using Mg doped AlN for future spintronic applications.

Publications

[1] Chintalapati Sandhya, Yang Ming, Lau Shu Ping and Feng Yuan Ping "Surface Magnetism of Mg doped AlN : a first principle study", J. Phy. Conds. Matter. **26**, 435801 (2014).

[2] Cai Yongqing, Bai Zhaoqiang, Chintalapati Sandhya, Zeng Qingfeng and Feng Yuan Ping, "Transition Metal Atoms Pathways on Rutile TiO2 (110) surface : Distribution of Ti3+ states and Evidence of Enhanced Peripheral Charge Accumulation", J. Chem. Phys. **138**, 154711 (2013).

[3] "Mechanism of Ferromagnetism in *sp* based systems : Mg doped AlN non-polar, polar and semi-polar surfaces" (in preparation).

[4] "Electronic and magnetic properties of Be doped AlN: Influence of surface effects" (in preparation).

[5] "Stability of Ferromagnetism in K doped AlN : Bulk to surfaces" (in preparation).

[6] "Stable ferromagnetic state in Si doped AlN with cation vacancies : Ab-initio study" (in preparation).

[7] “Magnetism in Phosphorene : Interplay between vacancy and strain” (in preparation).

[8] Ch. Sandhya, K. Hima Bindu, K. P. N. Murthy, and V. S. S. Sastry, “Phase transition in bond fluctuating linear polymer”, American Institute of Physics Conference Proceedings, 1349, 117 (2011).

AWARDS:

[1] Best Poster Award in ACCMS-7 conference (2013); Chintalapati Sandhya, Yang Ming, Cai Yongqing , Lau Shu Ping and Feng Yuan Ping, “ Surface magnetism of Mg doped AlN”.

[2] Best Poster Award in ICCP-9 conference (2015); Chintalapati Sandhya, Shen Lei and Feng Yuan Ping, “ Influence of surface orientation on the magnetism of non-magnetic element doped semiconductors”.

List of Tables

List of Figures

Chapter 1

Introduction

The discovery of Si based complementary metal oxide semiconductor (CMOS) in the 19^{th} century is one of the breakthroughs for the semiconductor technology and witnessed as a great success for microelectronic applications. In the past few years, size scaling had been used for the Si based devices to improve the performance of existing electronics. However, as the trend of minimization of the device continues, it triggers various problems such as quantum and thermal effects, short channel effect, and also large leakage current. Thus, the current semiconductor technology based on Si CMOS cannot be down scaled further and this urges new materials and technologies for the potential applications. In this direction, the discovery of semiconductor spintronics has emerged as one of the promising technologies.

In the recent decades, the research on semiconductor based spintronics is rapidly increasing in the view of developing novel applications and replacing the conventional

electronics. The traditional electronics make use of charge freedom of electrons in semiconductors and develop the charge based devices such as integrated circuits, transistors and high frequency devices. These devices play a crucial role in information processing and communication in the semiconductor technology. On the other side, spin based devices such as magnetic tapes and hard disks have been developed by manipulating spin freedom of electrons. Spin based devices are beneficial for information storage or magnetic recording. These devices mostly rely on the spontaneous magnetic ordering of the spins in magnetic materials, and the applications in this direction are limited for the information storage. Instead of considering separately the charge property of electrons in semiconductors and spin freedom of electrons in magnetic materials, the semiconductor spintronic technology has emerged with an idea of utilizing both charge and spin freedom of an electron in a single material [1]. Such a material should have both semiconducting and ferromagnetic behaviors to render the exciting prospect of integrating conventional semiconductor electronics and nonvolatile magnetic storage in a single device. Unfortunately, semiconductors that are prominently dominated in the present conventional electronics are non-magnetic in nature and the natural ferromagnetic materials utilized for spin based devices are metallic. Due to the large mismatch between existing natural semiconducting and ferromagnetic materials, it is rather difficult to combine those materials and attain both semiconducting and ferromagnetic behaviors.

The prerequisite of combining the ferromagnetic and semiconducting properties in a single material has been expected to be resolved with an idea of doping magnetic transition metals (TM) in a dilute limit into a semiconductor, which is further defined as dilute magnetic semiconductor (DMS). DMS would facilitate the possibility to get high

spin polarization by injecting magnetic semiconductor rather than ferromagnetic material into a non-magnetic semiconductor. One of the ultimate goals of DMS is to understand the spin-spin interaction in the solid state environment of semiconducting material, and provides a felicitous way to achieve electrically controllable ferromagnetism at the room temperature. In this direction, intense efforts have been put from past few years in achieving ferromagnetism in semiconductors by doping different transition metals in a dilute limit. A brief review on the progress of room temperature ferromagnetism in TM doped non-magnetic semiconductors will be discussed in the following section.

1.1 Magnetism in transition metal doped semiconductors

The prospect of ferromagnetism in semiconductors through doping of TM ions was first realized in III-V based semiconductor GaAs by doping Mn in the substitution of Ga [2]. In this experiment, the maximum Curie temperature of 60 K was obtained in (Ga,Mn)As. Various groups had achieved the maximum Curie temperatures up to 173 K in (Ga,Mn)As at different possible Mn concentrations [3, 4]. This fascinating discovery of ferromagnetism in (Ga,Mn)As invigorated the possibility to achieve ferromagnetism in semiconductors by doping TM dopants. Nevertheless, since the Curie temperature of (Ga,Mn)As is lower than the room temperature, it may not be reliable for the applications at room temperature. But the emerging phenomena of magnetism observed in Mn doped GaAs motivated further to procure high Curie temperatures. The importance of Mn substitution is that it can introduce local magnetic moments and itinerant holes

in the valence band and that are mutually coupled through *p-d* hybridization. Mn has been doped in different materials to quest for high Curie temperatures. Especially, from the theoretical study of Dietl *et al* [5], it was perceived that the wide band gap semiconductors such as GaN and ZnO etc. could be the potential materials to accomplish high Curie temperatures by *p*-type doping. For instance, a Curie temperature of 373 K was realized in Mn doped GaN [6] and the responsible mechanism behind the origin of ferromagnetism is the double exchange interaction between defect states [7]. Similarly, Curie temperature of 700 K was observed in Mn doped ZnO thin films by P. Sharma *et al* [8]. The origin of strong ferromagnetism in wide band gap semiconductors is due to the existence of strong localization of defect states, which can be usually achieved by suitable *p*-type doping. Several studies reinforce the possibility of high Curie temperature ferromagnetism [9–14] in TM ion doped nitride and oxide based semiconductors.

1.2 *sp/d*^{0} magnetism in non-magnetic element doped semiconductors

Despite the ferromagnetism in TM doped semiconductors, the origin of ferromagnetism in some of the TM doped semiconductors remains under debate [12, 15–18]. It is unclear whether the ferromagnetism in TM doped semiconductors is intrinsic or due to the cluster formation of TM dopants in host semiconductor [16, 17]. To avoid the problem of magnetic precipitates due to TM dopants, various research groups have tried to get magnetism in semiconductors by doping non-magnetic atoms rather than magnetic TM ions. Cu doped ZnO is one of such non-magnetic element doped semiconductors and a

room temperature ferromagnetism was observed [19, 20] for doping Cu in the substitution of Zn. With this motivation, high Curie temperatures have been realized in various non-magnetic element doped nitride and oxide based semiconductors [19–24]. The observation of ferromagnetism in non-magnetic element doped semiconductors grabbed the researchers′ attention in identifying the fundamental magnetism in those semiconductors and finding the potential practical applications for spintronics. The strong *p*-*d* hybridization between Cu-*d* and O-*p* orbitals is identified as the origin of strong ferromagnetism in Cu doped ZnO [19]. The various experimental as well as theoretical studies also showed a possibility of room temperature ferromagnetism in Cu doped GaN [21, 22]. The theoretical study predicted that the origin of ferromagnetism [21] in Cu doped GaN is due to the strong *p*-*d* hybridization between *d* orbital of Cu and *p* orbital of N atoms similar to the case of Cu doped ZnO.

According to the Zener model, the *d* shell of dopants in magnetic semiconductors is partially filled and well localized in the host as atomic like behavior. These *d* electrons of dopants with their localized nature play a crucial role in attaining a magnetic order especially in TM doped semiconductors. Interestingly, the recent fascinating discovery of ferromagnetism in C doped ZnO [25] indicates the possibility of attaining ferromagnetism through light element dopants with no *d* electrons. The Curie temperature of above 400 K was achieved in C doped ZnO with a doping concentration of 2.5% [25]. The magnetic moments are prominently derived from C atoms and the origin of ferromagnetism in C doped ZnO is due to the strong coupling between C-*p*, O-*p* and Zn-*d* orbitals. The *p*-*p* interaction between C and anions of the host ZnO semiconductor similar to the *p*-*d* hybridization in TM doped semiconductors, stabilizes the ferromagnetic

ground state in C doped ZnO. The 2*p* electrons of anions in nitrides and oxides have similar localized nature as *d* electrons and thus strong ferromagnetism has been expected in nitride and oxide based semiconductors through doping of suitable light elements. The magnetism that arises due to d^0 electrons is considered as *sp/d*^{0} magnetism. The fascinating discovery of room temperature ferromagnetism in C doped ZnO and the work of Dietl $et.al$ [5] motivated further to achieve ferromagnetism in a series of light element doped wide band gap semiconductors [26–30]. However, compare to 3*d* bands of TM ions, the 2*p* bands of the light elements are generally full in ionic states and provide no space for unpaired spins. How these light element dopants introduce the magnetic order in non-magnetic semiconductors is one of the challenging issue for the fundamental magnetism and it remains in debate over the half decade. The obscure origin and nature of high Curie temperature ferromagnetism in light element doped semiconductors constrain their practical applications for future spintronics. On the other hand, some of the experimental studies realized magnetism in undoped semiconductors at the low-dimension [31–35], and the origin of magnetism in those systems is believed to be due to surface defects. Thus it is necessary to understand whether the magnetic order is due to the dopants or surface defects at the low-dimension of magnetic semiconductors. Moreover, it is essential to understand the stability of magnetic order with the surface effects at the low-dimension for practical applications. In fact, several studies noticed the significant changes in the electronic and magnetic properties of magnetic semiconductors at the low-dimension due to surface effects.

1.3 sp/d^0 magnetism in non-magnetic element doped semiconductors at the low-dimension

In the past few years, several theoretical studies on magnetic semiconductors mainly dealt with bulk systems to quest for room temperature ferromagnetism and understand the origin of magnetism. On the other hand, many of the experimental observations rely on low-dimensional systems such as surface/interfaces, nanowires and nanostructures etc. to obtain room temperature ferromagnetism for spintronic nanodevice applications. Usually at the low-dimension, surface aggregation of the dopants may greatly influence the effectiveness of the diluted doping. Therefore, the change in the magnetic property could be possible from bulk to low-dimension of magnetic semiconductors. The dissimilarity between experimental and theoretical results is observed in some systems [6, 18, 36, 37] due to the different chemical environment from bulk to low-dimension. Especially, at the low-dimension, surface effects have a strong influence on the electronic and magnetic properties, which has been realized in several magnetic semiconductors [6, 7, 38–44]. One of the fascinating examples in this direction is Mn doped GaN [6, 7, 38, 43, 45]. Theoretical study on Mn doped GaN predicted room temperature ferromagnetism in its bulk structure, and realized that the strong *p-d* hybridization between *d* orbitals of Mn atoms and *p* orbitals of N atoms favors the ferromagnetic ground state with a very high Curie temperature [6, 7]. Whereas, antiferromagnetism was observed on Mn doped GaN thin films experimentally [45]. These theoretical and experimental observations showed a different magnetic order in Mn doped GaN due to a different chemical environment between the bulk and at the low-dimension. The obscure

origin of different magnetic order in Mn doped GaN was later resolved from the theoretical studies of magnetism on Mn doped GaN surfaces [38, 43]. According to these studies, the antiferromagnetic state is stabilized on the surface of Mn doped GaN due to the bond length contraction between Mn atoms on surface, and that could be reason antiferromagnetism was observed experimentally in Mn doped GaN thin films [45]. In fact, the theoretical work on Mn doped GaN thin films [38, 43] predicted that the ferromagnetism favors if Mn atoms located in the innermost layers of a slab during crystal growth, and if Mn atoms migrate to surface, antiferromagnetism favors due to the bond length contraction between Mn atoms on surface.

Due to a difference in the chemical environment between surface and the bulk, often a non-magnetic bulk material can become magnetic at the surface [31–35]. If there is any variation in the electron occupation on the surface, magnetic moment might be enhanced or reduced compared to that of bulk. The lower coordinated atoms at the surface can affect the band structure and also the surface magnetic moment. Since atoms at the surface are generally lower coordinated compared to those in bulk, surface atoms will be relaxed more than atoms in bulk, and introduce the variation in the bond lengths and hybridization between the atoms from bulk to surface. For example, the effect of lower coordination and different surface environment change the stability of ferromagnetism in case of Co doped ZnO and Mn doped ZnO [39, 40, 42]. The different doping location and dopant-dopant interaction at the surface might change the nature of magnetism. Due to a different bonding environment from bulk to surface, the change in the magnetic order that is from ferromagnetic to antiferromagnetic states has been observed in Cr doped ZnO [46]. In the case of Cr doped ZnO surface, the site preference of Cr exhibits different magnetic ground states.

The influence of surface effects on the magnetism is also observed for the case of non-magnetic element doped semiconductors. For instance, C doped SnO_2 [47] is non-magnetic at its bulk structure, but it becomes ferromagnetic at its surface. Due to the surface effects, there could be a change in the magnetic ground state at the low-dimension that is from ferromagnetic to antiferromagnetic states or vice versa compared to that of bulk. In fact, a few theoretical studies on magnetic semiconductors have shown significant changes in the formation energies, doping concentration and spin polarization energies etc. at the low-dimension compared to that of bulk [39, 48–50]. In most of the cases, formation energies are found to be less at the low-dimension than that of bulk, and indicates the possibility of high doping concentration at the low-dimension. The change in the magnetic property was also predicted in the nanowires of magnetic semiconductors [49] because of a large surface area to volume ratio. These several observations increasing the evidence of strong influence of surface effects on the electronic and magnetic properties of magnetic semiconductors at the low-dimension. Thus to identify the origin of magnetism and enhance the applications of magnetic semiconductors, the theoretical understanding of magnetism in the bulk systems is not sufficient. It is essential to know the influence of surface effects and the affect of diluted doping on the magnetism of semiconductor surfaces.

1.4 Physics of magnetism in dilute magnetic semiconductors

Even though there is no unified theory to explain the magnetism in DMS, several models were proposed to illustrate and understand the origin of magnetism in DMS.

1.4.1 Direct exchange interaction

Direct exchange interaction is an interaction between magnetic impurities through their direct overlap of the wave functions as shown in Fig. 1.1(a). In such a type of interaction, Pauli exclusion principle and Coulomb repulsion play a crucial role to decide the magnetic ground state. If two electrons have the same spin, then the Pauli exclusion principle prohibits those two electrons to appear on the same quantum state simultaneously. Thus for small interatomic distances, the anti-ferromagnetic coupling favors and it can be observed in Cr and Mo atoms etc. [51]. However, if the distance between the atoms increases, then electrons of the atoms prefer the parallel alignment of spins to minimize the electron-electron repulsion energy. This type of ferromagnetic direct exchange interaction can be found in $3d$ metals such as Fe, Ni, Co etc. For very large distances, the paramagnetic state will occur due to the lack of overlap between the wave functions.

The direct overlap of the wave functions of the dopants is possible in magnetic semiconductors only if the distance between dopants is close enough. Thus it might not be suitable to understand the long range magnetic order that was observed in various

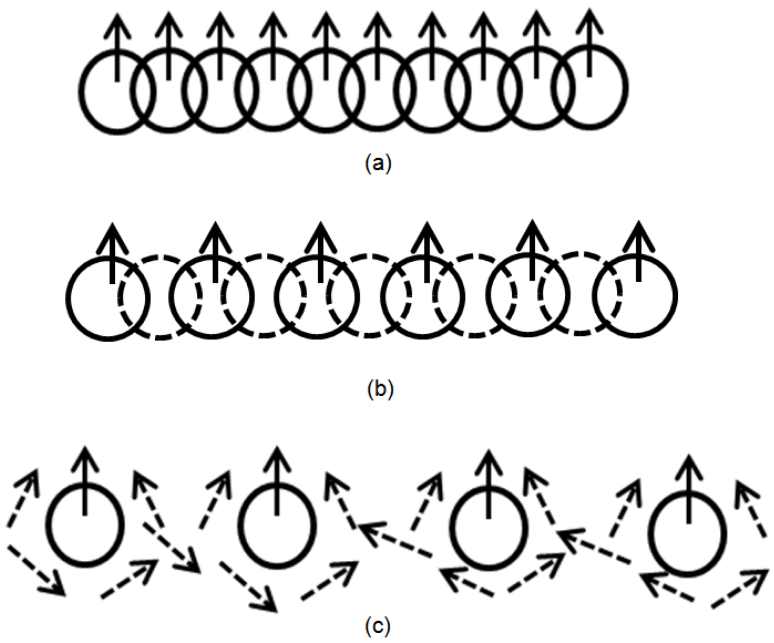

Figure 1.1: Schematic energy level diagrams of direct exchange interaction (a), super exchange interaction (b), and RKKY interaction (c).

magnetic semiconductors. In many of the DMSs, the distance between the impurities is larger than the nearest neighbor distance. So the effect of direct exchange interaction is weak and it is unlikely considerable for the long range type of magnetic interactions. The long range nature of magnetism that was identified in some of the magnetic semiconductors is due to the indirect exchange interaction, in which transition metal ions mediated through non-magnetic ions or conduction electrons (charge carriers). The different types of indirect exchange interactions will be discussed in the following sections.

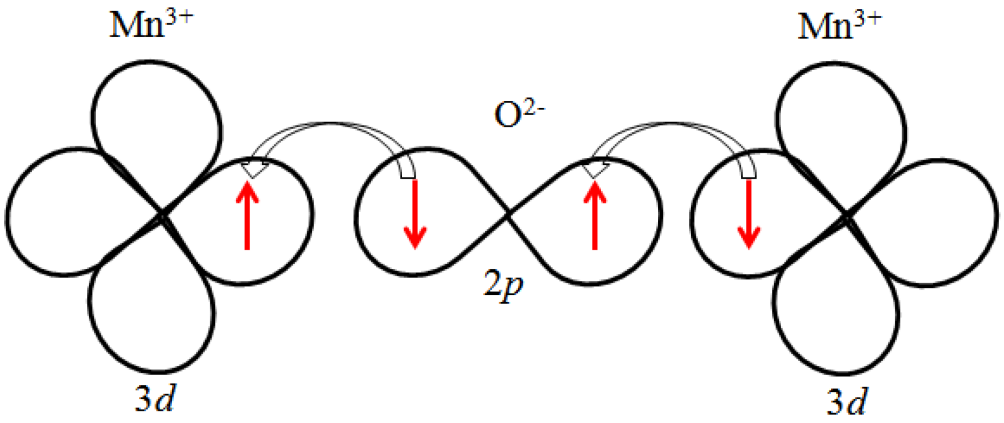

Figure 1.2: Schematic orbital diagram of super exchange interaction between Mn^{3+} ions mediated through O atom in MnO.

1.4.2 Super exchange interaction

Super exchange is an indirect exchange interaction, in which magnetic impurities are mediated through non-magnetic atoms [52] as shown in Fig. 1.1(b). For example, consider two Mn^{3+} ions with an electronic configuration of $3d^4$ in MnO. The transition metal ions Mn^{3+} interact each other through a non-magnetic O atom as shown in Fig. 1.2. Here *d* orbitals of Mn^{3+} ions are half filled and interact with *p* orbital of O atoms. Because of *p-d* hybridization, there is a possibility of charge hopping from O to Mn atoms. According to the Hund′s rule, spin up electron of O atom will hop to one of the Mn^{3+} ion and spin down electron of O atom hop to another Mn^{3+} ion. Therefore, charge hopping between Mn and O ions mediated through *p-d* hybridization favors the antiferromagnetic ground state. The similar mechanism has been realized in a number of oxides and fluorides such as CaO, NiO and MnF_2 etc.

1.4.3 RKKY interaction

The mechanism which involves in the interaction between magnetic atoms mediated through charge carriers or band electrons is defined as Ruderman-Kittel-Kasuya-Yosida (RKKY) model [53] as shown in Fig. 1.1(c). If the states of magnetic ions are more localized, the direct exchange interaction between the ions is negligible or the coupling between them is weak. However, these ions interact through itinerant carriers and attain either ferromagnetic or antiferromagnetic ground state.

The RKKY exchange coupling constant J_{ij} is proportional to $F(2k_F R)$, where $F(x) = \frac{xcosx - sinx}{x^4}$ and $R = |R_j - R_i|$ is the distance between magnetic ions. The coupling constant J_{ij} has an oscillating behavior and it varies with the distance between magnetic atoms. Therefore, the coupling can be ferromagnetic or antiferromagnetic depends on the distance between the magnetic atoms.

1.4.4 Double exchange interaction

Zener double exchange mechanism is useful to understand the magnetism in semiconductors due to dopants of same chemical nature but different charge states [54]. For example, consider d^3 and d^4 metal ions of Mn mediated through non-magnetic atoms as shown in Fig. 1.3. The electrons are filled in the t_{2g} and e_g orbitals of each metal ion based on the Hund′s rule. Due to a difference in the valence states of metallic ions, one *d* electron of e_g orbital hops from one ion to the other ion through *p* orbital of non-magnetic atoms. Different from super exchange interaction, there is a possibility of virtual charge hopping of same spin electron between the defect levels that invokes

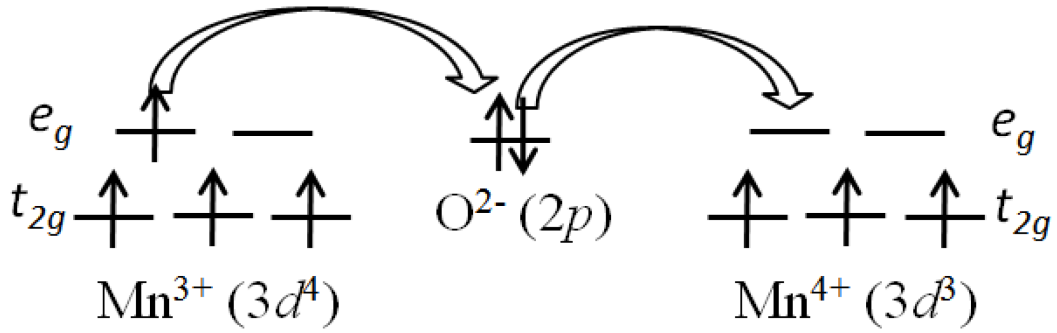

Figure 1.3: Schematic energy level diagram of double exchange interaction between Mn ions at different charge states.

the energy gain in ferromagnetic arrangement. This indicates that the double exchange mechanism stabilizes mostly a ferromagnetic state. The origin of ferromagnetic coupling between Mn^{2+} and Mn^{3+} ions in Mn doped ZnO etc [12] is well understood using Zener double exchange mechanism.

1.4.5 Kinetic exchange interaction

Kinetic exchange interaction involves in the magnetic ordering by virtual hopping of an electron from one site to another neighboring site. This charge hopping is mainly driven by the kinetic energy of electrons. The probability of charge hopping from one site to another neighboring site determines the strength of the magnetic interaction. The *p-d* hybridization which usually appears in Mn-based II-VI DMS can be thought of as a virtual charge hopping of an electron between *p* orbital of non-magnetic host anions and *d* orbital of Mn atoms. However, based on the ordering of spin of transition metals, the hopping interaction between the defects favors either antiferromagnetic or ferromagnetic configuration. For instance, the *d* orbitals of Mn atoms in MnO are half filled and the

energy levels split into e_g and t_{2g} levels [55]. By following the Hund′s rule, which favors in increasing the spin, the *d* electrons of each Mn^{2+} ion occupy in e_g and t_{2g} orbitals. In this case, the virtual charge hopping of electrons between Mn and O atoms mediated through *p-d* hybridization decreases the total spin based on the Pauli exclusion principle and favors the antiferromagnetic arrangement. Different from Mn^{2+}, if one of the orbitals is empty, then Pauli exclusion principle does not favor any spin direction and thus it prefers to increase the spin based on Hund′s rule. For instance, in case of Sc^{2+} and Ti^{2+} ions [55], at least one of the orbital is empty and the hybridization favors ferromagnetic interaction.

The magnetic ordering in many of the solids is a result of competition between different exchange mechanisms. For instance, in case of Fe_3O_4, the double exchange mechanism favors ferromagnetic coupling between Fe^{3+} and Fe^{4+} ions at octahedral sites and super exchange interaction favors antiferromagnetic coupling between Fe^{3+} ions located at octahedral and tetrahedral sites. The competition between double and super exchange interactions results in a ferromagnetic ground state in Fe_3O_4. Similarly, the interplay between different exchange mechanisms decides the magnetic ground state in several oxide and nitride based magnetic semiconductors [12]. This indicates that a single mechanism is not adequate to understand the magnetic nature in DMSs, and it is crucial to consider the competition among different exchange mechanisms. On the other hand, it is rather complex to identify the competition between different mechanisms in DMSs. Recently, several studies on magnetic semiconductors have succeeded in understanding the magnetic phenomena by considering energy level diagrams and charge hopping between defect levels, and map with a simple Hubbard or Heisenberg models [56–58]. For instance, the stability of magnetic ground state in GaN due to Ga vacancy is well

understood from the analysis of energy level diagrams and charge hopping mechanism between the defect levels [56]. In case of a Ga vacancy at a neutral state, since spin down states are completely empty in the energy level diagram, charge hopping is only possible in antiferromagnetic arrangement and thus gives the antiferromagnetic ground state. However, upon adding an extra charge to the vacancy (negative charged state), ferromagnetism favors to be in a ground state due to the possibility of direct charge hopping between partially filled states of parallel spin. In case of antiferromagnetic coupling, parallel spins are at different energy levels and result in less energy gain compared to that of ferromagnetic coupling. Similar mechanism is also realized in ZnO due to defects [57]. Moreover, the latest theoretical studies resolved the nature of magnetism in N doped MgO by examining the charge hopping mechanism between N and O atoms [58]. From these studies, it is realized that the knowledge of proper energy level diagrams and the charge hopping mechanism between defects are some of the crucial factors to understand the nature of local magnetic order especially in non-magnetic element doped semiconductors. Similarly, there are different models like band coupling model [59] and molecular orbital theory [60] can also be employed to understand the magnetism in many of the DMSs. Here it is important to notice that all these models indirectly involve the competition between different exchange mechanisms.

1.5 Motivation and scope for the present work

Over the course of years, several theoretical and experimental studies on magnetic semiconductors have mainly dealt with obtaining ferromagnetism in $3d$ or $4f$ based semiconductors by doping non-magnetic ions. However, there are a few studies realized

magnetism in *sp* based systems [58, 61–63]. Among those, AlN is one of the largest wide band gap III-V based semiconductor with many applications in opto electronics and high energy devices [64–69]. In addition, room temperature ferromagnetism was predicted recently in Mg doped AlN by doping Mg in the substitution of Al (Mg_{Al}) [62], which shows a possibility to integrate optoelectronics with spintronics. Based on the work of Dietl *et.al* [5], Mg doped AlN meets the requirement of wide band gap and light element Mg doping, which further supports the possibility to attain strong ferromagnetism in Mg doped AlN. The latest experimental observations [70–72] increase the evidence of room temperature ferromagnetism in Mg doped AlN. One of the experimental groups [70] successfully grown the Mg doped Zigzag nanowires (ZNWs) of AlN as shown in Fig. 1.4, observed the room temperature ferromagnetism. It was expected that the $(10\bar{1}1)$ surface orientation may play a crucial role in obtaining ferromagnetism in Mg doped Zigzag AlN nanowires. The subsequent experimental studies [71] realized the room temperature ferromagnetism in normal nanowires of Mg doped AlN by increasing the crystal growth temperature. The present existing theoretical and experimental results indicate the intrinsic nature of ferromagnetism in Mg doped AlN, which is not the general trend in many of the room temperature ferromagnetic semiconductors such as Mn doped GaN, Cr doped ZnO or Co doped ZnO etc. [6, 7, 38–44]. The growing evidence of intrinsic nature of ferromagnetism in Mg doped AlN should need considerable attention for future spintronic applications. In fact, as of our knowledge, till now there are no controversial results against the ferromagnetism in Mg doped AlN.

However, the origin and mechanism of ferromagnetism in AlN due to Mg_{Al} is unclear. Even though room temperature ferromagnetism was predicted theoretically in Mg doped bulk AlN and observed experimentally in Mg AlN nanowires, how Mg_{Al} introduces the

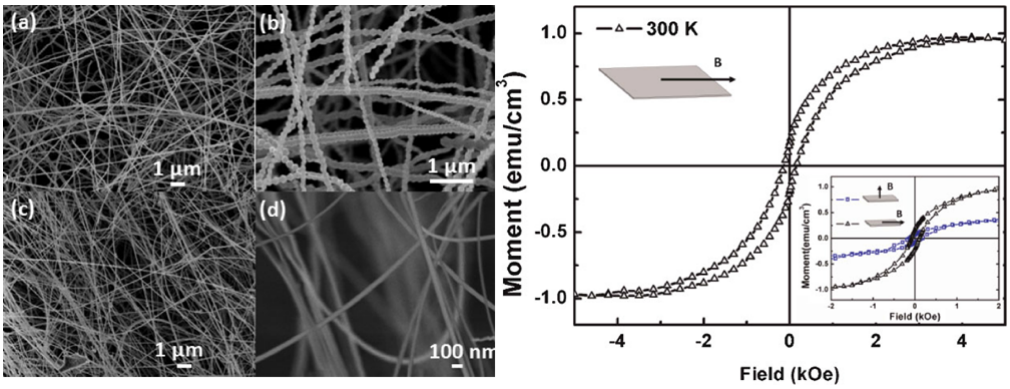

Figure 1.4: The SEM image of Mg doped AlN zigzag nanowires and the corresponding magnetic hysteresis loop are shown in left and right side of the figure respectively [70].

magnetic moments and why these moments favor the ferromagnetic arrangement rather than antiferromagnetic arrangement is unknown. The Mg doping in AlN contains only *s* and *p* electrons and introduces the *sp* magnetism. The observation of ferromagnetism in Mg doped AlN that involve with only *s* and *p* electrons is one of the fascinating discovery for the fundamental science and practical applications. Moreover, it is known that surface effects have vital role on the magnetism of several magnetic semiconductors at the low-dimension. Therefore, to identify the origin of ferromagnetism and enhance the applications of Mg doped AlN for future spintronic nanodevices, it is essential to understand the influence of surface effects on the ferromagnetism introduced by *s* and *p* electrons of Mg doped AlN. The studies are limited in understanding the magnetism of non-magnetic element doped III-V based semiconductors especially at the low-dimension.

In order to reveal the nature of magnetism and enhance the potential applications of

Mg doped AlN for future spintronic nanodevices, I investigate the electronic and magnetic properties of Mg doped AlN from bulk to different surface orientations using first-principles calculations based on the density functional theory. Several surface orientations such as non-polar, polar and semi-polar surfaces of Mg doped AlN have been considered to find out the dominant contribution of magnetism from each surface orientation and the influence of surface effects on the magnetism. Similarly, I also investigate the prospect of magnetism in other alkali and alkaline earth metals doped AlN from bulk to various surfaces. To find out the nature of magnetism from bulk to low-dimension, several factors have been explored as follows (1) mechanism of the magnetic property due to single Mg defect in AlN, (2) the effect of Mg doping on magnetism of different surfaces, (3) the influence of surface effects on the magnetism of Mg doped AlN surfaces, (4) origin and stability of ferromagnetism on various Mg doped AlN surfaces and (5) the applicability of observed magnetic phenomenon in Mg doped AlN for the case of other alkali and alkaline earth metals doped AlN. With this notion, this thesis is organized as follows. In chapter 2, the theory of first-principles calculations has been introduced, which helps to investigate the electronic and magnetic properties of alkali and alkaline earth metals doped AlN. In chapter 3, the electronic and magnetic properties have been discussed for Mg and other alkali (earth) metals doped AlN. In chapters 4, 5 and 6; the electronic and magnetic properties have been studied for non-polar, polar and semi-polar surfaces of Mg doped AlN respectively. In chapter 7, the electronic and magnetic nature of other alkali (earth) metals doped surfaces have been explored. Finally, the summary and outlook of this project are concluded in chapter 8.

Chapter 2

First-principles calculations

The electronic and magnetic properties of materials are calculated by first-principles calculations using density functional theory (DFT) implemented in VASP [73] software package. The fundamental properties of materials can be determined if we can resolve the Schrödinger equation for many body problem. However it is difficult to solve the Schrödinger equation of many body problem due to the complexity of interaction between very large number of electrons (10^{23}) and nucleus. Several approximations have been made to address many body problem such as Born-Oppenheimer approximation, Hartree, and Hartree-Fock etc. DFT has been the dominant quantum mechanical modelling method to simplify the problem by considering density functional instead of wave function. First-principles calculations based on DFT was quite successful to understand the basic properties of various materials. In this chapter, a brief introduction about earlier approximations and theories that were led up to DFT will be discussed.

2.1 Born-Oppenheimer approximation

In quantum mechanics, the Schrödinger equation for many body system is described as,

$$H\Psi = E\Psi \ , \tag{2.1}$$

where $\Psi = \Psi(r_1, r_2, r_{3,.....}r_n)$ is the wave function, E is the energy eigen value and the Hamiltonian operator $\hat{H}$ is given by,

$$\hat{H} = \sum_{i=1}^{N}(\frac{P_i^2}{2m_i}) + \frac{1}{2}\sum_{i\neq j}^{N}(\frac{q_i q_j}{|r_i - r_j|}) \ , \tag{2.2}$$

where summation is over all electrons including nucleus and m_i is the mass of the nucleus or electron, q_i is their corresponding charge. The Hamitonian $\hat{H}$ of many body problem includes the electron-electron interaction, electron-ion interaction and ion-ion interaction, which can be written as,

$$\begin{aligned}\hat{H} &= -\sum_l \frac{\hbar^2}{2m_e}\nabla_l^2 - \sum_k \frac{\hbar^2}{2M_N}\nabla_k^2 + \frac{1}{2}\sum_{l\neq j}\frac{e^2}{|r_l - r_j|} + \frac{1}{2}\sum_{k\neq j}\frac{e^2}{|R_k - R_j|} - \sum_{k\neq l}\frac{e^2}{|R_k - r_l|} \\ &= T_e + T_N + V_{e-e} + V_{N-N} - V_{N-e} \ ,\end{aligned} \tag{2.3}$$

where T_e, T_N are the kinetic energies of electron and ion respectively ; V_{e-e}, V_{N-N} and V_{N-e} are the potential energies of electron-electron, ion-ion and ion-electron interactions. It is almost impossible to solve many body Schrödinger Eq. (2.2) as it includes all those interactions. Hence it much requires several approximations to simplify the problem.

The first approximation that was made to simplify the many body problem is Born-Oppenheimer approximation [74]. According to this approximation, since the nucleus is much heavier than electrons, the kinetic energy of nucleus can be neglected compared to

that of electrons. Hence we can assume that the nuclei are at fixed positions and electrons to be in equilibrium with them adiabatically. This adiabatic environment reduces the many body problem into a system of interacting electrons moving in an external potential V(r) formed by a frozen-in ionic configuration of nuclei. So in the Eq. (2.3), the nuclei part can be handled using classical approach. The Hamiltonian $\hat{H}$ for the electronic part according to Born-Oppenheimer approximation can be written as,

$$\hat{H} = T_e + V_{e-e} + V(r) \; . \tag{2.4}$$

Even though Born-Oppenheimer approximation greatly simplifies the problem, the electron-electron interaction in the Hamiltonian which involves a large number of electrons (10^{23}) still remains a difficulty in solving the Schrödinger equation.

2.2 Density functional theory

DFT of Hohenberg and Sham [75, 76] showed an efficient method to simplify the many body problem and describes the electron-electron interaction. Considering charge density $\rho(r)$ as the fundamental variable instead of a wave function makes DFT remarkable and it gives a great conceptual simplification of many body problem. The ground state electron density uniquely determines the ion-electron interaction potential, which will give information about all ground state properties and thus electron density is considered as a basic variable in DFT. There are two important theorems form the basis for DFT.

Theorem 1: The ground state density $\rho(r)$ uniquely determines the external potential V(r) to within an additive constant. Instead of wave function, this theorem proves that the ground state electron density can be considered as a fundamental quantity. Since

the number of electrons and external potential are feasible to determine by the electron density $\rho(r)$, it also determines the Hamiltonian and all other ground state electronic properties of a system.

The total energy in-terms of electron density is written as,

$$\begin{aligned} E = E\left[\rho(r)\right] &= T\left[\rho(r)\right] + U_{ee}\left[\rho(r)\right] + \int \rho(r)V(r)dr \ , \\ &= F_{HK}\left[\rho(r)\right] + \int \rho(r)V(r)dr \ , \end{aligned} \tag{2.5}$$

where the elctron-electron interaction energy $U_{ee}\left[\rho(r)\right]$ contains the coulomb interaction $U_{cou}\left[\rho(r)\right]$ which is given by:

$$U_{cou}\left[\rho(r)\right] = \frac{e^2}{2}\iint \frac{\rho(r)\rho(r')}{|r-r'|}drdr' \ . \tag{2.6}$$

Theorem 2 : The ground state electron density $\rho(r)$ minimizes the energy functional $E(\rho(r))$ through variational method. The global minimum of $E(\rho(r))$ can be possible to obtain by varying the electron density $\rho(r)$ using variational principle. For a trail electron density $\rho(r)$, there exists

$$E_0 = E\left[\rho_0(r)\right] \leq E\left[\rho(r)\right], \tag{2.7}$$

where E_0 is the ground state energy corresponding to the ground state electron density $\rho_0(r)$. Therefore if we know the approximate energy functional $E(\rho_0(r))$, the ground state energy can be determined by varying the $\rho_0(r)$.

However, the explicit form of $F_{HK}\left[\rho(r)\right]$ is hard to get due to the fact that the accurate calculational implementations of DFT are not easy to achieve. On the other side, Hohenberg-Kohn theorem stated that the ground state energy of many body problem

can be obtained by using electron density alone, but it does not provide any useful computational scheme. Kohn and Sham showed that it is possible to map the many-body problem with a set of non interacting single electron equations [76, 77]. They suggested the functional $F[\rho(r)]$ for any many body interacting system can be separated as,

$$\begin{aligned} F[\rho(r)] &= T[\rho(r)] + U_{ee}[\rho(r)] \ , \\ &= T_{non}[\rho(r)] + U_{cou}[\rho(r)] + E_{xc}[\rho(r)] \ , \end{aligned} \tag{2.8}$$

where,

$$T_{non}[\rho(r)] = \sum_i < \Psi_i \left| -\frac{\hbar^2}{2m_e}\nabla_i^2 \right| \Psi_i > \ , \tag{2.9}$$

$$U_{cou}[\rho(r)] = \frac{1}{2}\int \frac{\rho(r)\rho(r')}{|r-r\prime|} dr dr' \ , \tag{2.10}$$

and

$$E_{xc}[\rho(r)] = T[\rho(r)] - T_{non}[\rho(r)] + U_{ee}[\rho(r)] - U_{cou}[\rho(r)] \ , \tag{2.11}$$

where $T_{non}[\rho(r)]$, $U_{cou}[\rho(r)]$, and $E_{xc}[\rho(r)]$ are the non interacting kinetic energy, coulomb energy and exchange-correlation energies respectively.

The electron density of non interacting systems can be written as,

$$\rho(r) = \sum_{s=\pm 1/2} \sum_{i=1}^{N/2} |\Psi_i(r,s)|^2 \tag{2.12}$$

At the global minimum energy functional, one has to satisfy

$$\delta \left\{ F[\rho(r)] + \int V(r)\rho(r) dr + \lambda \left[N - \int \rho(r) dr \right] \right\} = 0 \ , \tag{2.13}$$

where λ is the Lagrange multiplier to make sure that $\delta\rho(r)$ is performed at constant particle number N. If we plug Eq. (2.8) in the above equation Eq. (2.13), then we can get,

$$\lambda = \frac{\delta T_{non}}{\delta\rho(r)} + \int \frac{\rho(r')}{|r-r\prime|} dr' + \frac{\delta E_{xc}}{\delta\rho(r)} + V(r) \ , \tag{2.14}$$

$$\lambda = \frac{\delta T_{non}}{\delta \rho(r)} + V_{KS}(r) \ , \tag{2.15}$$

where $V_{KS}(r)$ is the Kohn-Sham effective potential and it is defined by,

$$V_{KS}(r) = \int \frac{\rho(r')}{|r - r\prime|} dr' + \frac{\delta E_{xc}}{\delta \rho(r)} + V(r) \ . \tag{2.16}$$

Therefore in the case of non interacting electron system, the equation for the particle wave function is just the Schrödinger equations,

$$\left[-\frac{\hbar^2}{2m} \nabla_i^2 + V_{KS}(r_i) \right] \Psi(r_i) = \varepsilon_i \Psi(r_i); i = 1, 2....N \tag{2.17}$$

and it is defined as Kohn-Sham equation. Since $V_{KS}(r)$ and $\rho(r)$ are related recursively, the above equation needs to be resolved self consistently. At the end, the total energy of interacting system of N particles can be written as,

$$E = \sum_i \varepsilon_i - U_{cou}\left[\rho(r)\right] + E_{xc}\left[\rho(r)\right] - \int \frac{\delta E_{xc}}{\delta \rho(r)} \rho(r) dr \ , \tag{2.18}$$

where

$$\begin{aligned} \sum_i \varepsilon_i &= \sum_i < \Psi_i \left| -\frac{\hbar^2}{2m} \nabla_i^2 + V_{KS}(r) \right| \Psi_i > \ , \\ &= T_{non}\left[\rho(r)\right] + \int V_{KS}(r) \rho(r) dr \ . \end{aligned} \tag{2.19}$$

In the above equations all terms are treated exactly except the precise form of exchange correlation functional $E_{xc}\left[\rho(r)\right]$ is unknown.

2.2.1 LDA and GGA

Kohn and Sham proposed Local density approximation (LDA) [76] to overcome the problem of unknown exchange correlation functional. In LDA, it is assumed that the

electron density at a point r of a system of slowly varying density can be considered as if it is homogenous in a small region. So the exchange correlation energy $\varepsilon_{xc}(r)$ at point r is assumed as the exchange correlation energy of homogeneous gas at point r. It can be calculated as,

$$E_{xc}\left[\rho(r)\right] \approx \int \varepsilon_{xc}(r)\rho(r)dr \ , \tag{2.20}$$

where $\varepsilon_{xc}(r) = \varepsilon_{xc}^{homo}(\rho(r))$ and $\varepsilon_{xc}^{homo}(\rho(r)$ contains the contribution of both correlation and exchange energies which can be further split into,

$$\varepsilon_{xc}^{homo}(\rho(r) = \varepsilon_{c}^{homo}(\rho(r) + \varepsilon_{x}^{homo}(\rho(r) \ . \tag{2.21}$$

The exchange energy $\varepsilon_{x}^{homo}(\rho(r)$ is simplified by Hartree-Fock description of electron gas and it is proportional to $\rho(r)^{4/3}$. However, in LDA it is important to notice that it neglects the surrounding inhomogeneities of electron density at point r. Even though, there is an inexact nature of the approximation, LDA was proved as a good approach in calculating vibrational frequencies, electronic structures, elastic moduli and stability of phase. On the other side, there are several problems arise with LDA. For example, the band gaps and lattice constants are underestimated in LDA for several semiconductors and insulators. Moreover the magnetic properties using LDA are not well appreciated by several studies.

Since in LDA, homogenous electron density has been considered, it is not suitable to calculate exchange correlation energy in case of non-uniform charge density problems. But the deviations of charge density can be calculated by considering the gradient of total charge density. The improvement of LDA is GGA, in which the gradient of electron density was also considered to better approximate the exchange correlation functional at point r. So in GGA, there is an explicit dependence of exchange correlation functional

on both charge density and its gradient at point r which can be written as,

$$\varepsilon_{xc}^{GGA}[\rho(r)] = \int f(\rho, \nabla\rho)dr \ . \tag{2.22}$$

There are several forms for gradient approximations, among GGA proposed by Perdew $et\ al$ [78–80] has been widely used and proved to be successful in calculating various properties such as mechanical, electronic, optical and magnetic properties. At least in case of system of light elements, GGA is assumed to be the proper approach to calculate different properties. The electronic and magnetic properties in several studies were found to be accurate by using GGA proposed by Perdew $et\ al$ [78–80].

2.2.2 Bloch theorem and supercell approach

In Density functional theory, many body problem was quite simplified by mapping the Schrödinger equation with a system of non interacting single electron Kohn-Sham equations. However, it is difficult to handle an infinite number of non-interacting electrons within a static potential of infinite number of nuclei or ions. To resolve this issue, firstly the wave function of each electron in the system needs to be calculated. Secondly, the infinite basis function to expand wave function is required. Fortunately, these problems can be reduced in case of periodic systems based on Bloch theorem. In a perfect crystal, the electrons move in a periodic potential of regular arranged arrays of ions, so the external potential can be written as $V(r + R) = V(r)$, where R is the lattice vector in real space.

According to Bloch theorem, if the electron moves in a periodic potential, then the

corresponding wave function can be defined as:

$$\Psi_k(r + R) = e^{iK.R} u_k(r) \tag{2.23}$$

Therefore, according to the Bloch theorem, the wave function of any atom in a periodic lattice can be rewritten as a product of the wave function $u_k(r)$ and its corresponding plane wave. Similarly, the k-point outside the 1^{st} Brillouin zone can always be mapped to the k-point in the 1^{st} Brillouin zone. So in the context of electronic structure calculations, the wave function Ψ_k can also be folded into the 1^{st} Brillouin zone due to periodic behavior of the energy.

However, many real systems such as surfaces, interfaces, nanotubes and nanowires etc are not periodic along all the three dimensions. There are two approaches to study the properties, cluster model and periodic supercell model. In a cluster model, system is modeled with a cluster of atoms. In a periodic supercell model, the periodic symmetry is considered on the aperiodic dimension. For non periodic systems, for example, in case of defects and surface calculations, a periodic supercell method has been proved to be one of the quite efficient method. This method is implemented in surface/interface calculations by modeling surface or interface with periodically arranged slabs that are separated by vacuum layers. The artificial coulomb interaction between neighboring slabs can be minimized by considering a sufficient thickness of vacuum layer. Depend on the inter layer spacing in a slab, the thickness of vacuum layer changes. Usually, vacuum layer should be thicker for a slab with a smaller inter layer spacing.

2.2.3 K-point sampling

Electronic states are allowed only at a particular set of k-points. Therefore, it can be determined by the boundary conditions that are applied to the bulk solid. The density of k-points changes depending on the volume of the solid. In a solid, we have an infinite number of k-points for the infinite number of electrons. Bloch theorem resolves the problem of calculating an infinite number of electronic wave functions to the one of calculating a finite number of electronic wave functions at an infinite number of k points. So only a finite number of electronic states will be occupied at each k-point. Since the occupied electronic states at each k-point contribute to the electronic potential in a solid, it requires an infinite number of calculations to compute the potential. However, if the k-points are close together, then the change in the electronic wave function $\Psi_{n,k}$ with k becomes negligible and a great simplification is possible by calculating at finite number of k-points which is called k-point sampling. For k-points sampling, various methods [81, 82] were proposed by Monkhorst-pack method, Blochl-Jepsen-Andersen, Lehmann-Taut, Muller-Wilkins, Methfessel and coworkers etc. Among them the Monkhorst-Pack method [82] is the mostly used method for calculations. The basic idea of this method for sampling k-points is to construct equally spaced k-points $(N_1 \times N_2 \times N_3)$ in the first Brillouin using the following expression.

$$k = \frac{n_1 + 1/2}{N_1} b_1 + \frac{n_2 + 1/2}{N_2} b_2 + \frac{n_3 + 1/2}{N_3} b_3, \tag{2.24}$$

where n_1, n_2 and $n_3 = 0, ...N_i - 1 (i = 1 \sim 3)$. Based on the symmetry, it is possible to map the equivalent k-points to each other, which further reduce the total number of k-points significantly generated by the above equation. If we use more number of k-points, the error due to k-point sampling reaches to zero and the total energy will converge. Especially, for metallic systems, more number of k-points are required to determine the

Fermi surface. However, computational cost is high to perform at very dense k-points sampling. In such cases, k.p perturbation method is one of the preferable method, which reduces the computational cost of performing at very dense k-points.

2.2.4 Plane wave basis sets

Based on Blochs theorem, the single electron wave function Ψ_j and the potential V_j can be expressed using plane wave basis $exp(iG.r)$:

$$\Psi_j = \sum_G C_j(G) exp(iG.r) \ , \tag{2.25}$$

$$V_j = \sum_G V_j(G) exp(iG.r) \ , \tag{2.26}$$

and the correponding kinetic energy at a k-point can be defined as :

$$E_{cut} = \frac{\hbar^2}{2m} \left| k + G_{cut} \right|^2 \ , \tag{2.27}$$

where the plane waves $exp(iG.r)$ are confined within a sphere of radius G_{cut}. One of the advantage in working with a plane wave basis set is that the kinetic part of Kohn-Sham can be easily computed as:

$$\frac{\hbar^2}{2m} \nabla^2 \Psi_j = \frac{\hbar^2}{2m} \sum_G \left| G \right|^2 C_j(G) exp(iG.r) \tag{2.28}$$

From the preceding ideas, the Kohn-Sham equation can be reduced to the secular equation:

$$\sum_{G\prime} \left[\frac{\hbar^2}{2m} \left| k + G \right|^2 \delta_{GG'} + V(G - G') + V_H(G - G') + V_{xc}(G - G') \right] c_{n,k+G'} = \varepsilon_{n,k} c_{n,k+G} \tag{2.29}$$

In principle, we need an infinite plane wave basis set to expand infinite electronic wave function. But the advantage of plane wave basis set is that the coefficients $c_{n,k+G}$ for the plane wave with small kinetic energy $\frac{\hbar^2}{2m}|k+G|^2$are more important than with larger kinetic energy. So the plane wave basis set can be truncated to include only plane waves that have kinetic energies lesser than particular cutoff energy E_{cut}. But the total energy might not accurate due to the truncation of plane wave basis set. However, the accuracy of total energy can be improved by considering high E_{cut}. Normally, we should choose a particular cut off energy which will converge the total energy.

2.2.5 Pseudo potential approximation

As seen earlier in the above sections, the Bloch theorem and plane wave basis set greatly simplifies the problem of Kohn-Sham equations of an infinite solid. However in the core region, the ionic potential is very strong and thus requires a large number of plane waves to describe the rapid oscillations of wave functions of the valence electrons in the core region. This would cause all electron calculations to be expensive and even make it impractical for large systems. Fortunately the problem can be resolved by pseudo potential approximation [83–85] which allows the expansion of electronic wave functions with much smaller number of plane wave basis sets.

Usually in solids, most of the physical properties of materials are mainly determined by the valence electrons and the properties have negligible dependency on the bound core electrons. For instance, the nature of bonding involves only the valence electrons but not the core electrons. In the pseudo potential approximation, the effect of bound core electrons is treated together with nuclei and the strong ionic potential, which is replaced

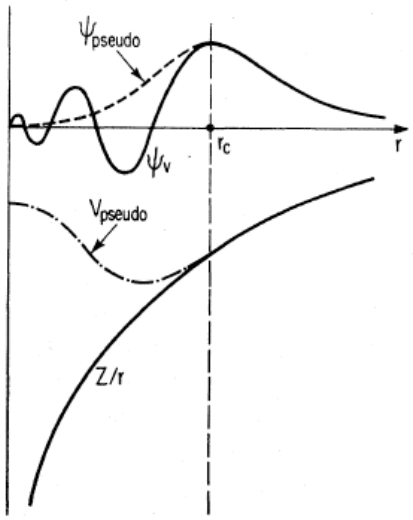

Figure 2.1: Schematic illustration of all electron (solid lines) and pseudo electron (dash lines) potentials and their corresponding wave functions.

by a weaker pseudo potential (V_{pseudo}). This pseudo potential acts on pseudo wave functions rather than real wave functions as shown in Fig. 2.1 [86]. The pseudo potential is approximated in such a way that outside the cutoff radius (r_c), the pseudo potential and pseudo wave functions are similar to the real electron wave function, whereas there are no radial nodes in the pseudo valence states in the core region.

The general form of pseudo potential is :

$$V_{pseudo} = \sum_{lm} |lm > V_l < lm| \,, \tag{2.30}$$

where $\mid lm >$ are the spherical harmonics and V_l is the pseudo potential for angular momentum l.

In the first-principles calculations, the frequently used pseudo potentials are norm-conserving and ultrasoft pseudo potentials. The norm-conserving potentials are discovered by Bachelet

et al [87]. In these potentials, even though the pseudo wave functions differ from real valence wave functions inside (r_c), the norm is constrained to be same as the real valence states. The corresponding wave function is defined as :

$$\int_0^{r_c} \left|\Psi^{ps}_{n,k}(r)\right|^2 dr = \int_0^{r_c} \left|\Psi_{n,k}(r)\right|^2 dr. \tag{2.31}$$

The norm conserving potential is found to be accurate for the solids which contains *s*, *p*-bond main group elements. But in case of 2*p* second row elements, 3*d* transition metals and rare earth elements, norm-conserving pseudo potentials are less effective due to the highly localized valence states in those elements. It requires a large number of planes waves to describe such valence states. Vanderbleit proposed ultra soft pseudo potential to overcome this problem [88]. In this potential, the plane wave cutoff required for the calculations is greatly reduced by removing the norm conserving constrain and makes the pseudo wave functions inside r_c as smooth as possible. However, compare to ultrasoft pseudo potentials, projector augmented wave (PAW) method developed by Blöchl [89] is found to be more accurate and it requires smaller radial cutoffs (core radii) than in ultrasoft pseudo potentials. In PAW method, the valence wave function with all nodes in the core region is exactly reconstructed and it makes PAW to be more accurate than ultrasoft pseudo potentials and the computational cost using PAW potentials is not more expensive.

2.2.6 Kohn-Sham energy functional minimization

The electronic states corresponding to the minimized Kohn-Sham (KS) energy functional are important for the total energy pseudo potential calculations. However, the

indirect approach of getting self consistent KS Hamiltonian may lead to instability due to discontinuous changes of KS hamiltonian from iteration to iteration. To avoid the instability, the direct minimization of KS energy functional is the proper way because the KS energy functional normally has a single well defined energy minimum. Therefore, an efficient method is necessary to minimize the KS energy functional in an accurate way for the calculations.

The conjugate gradient (CG) is one of such techniques which provides a simple procedure to minimize the KS energy functional. To locate the minimum of the energy, the negative of the gradient is considered as the initial search direction in CG technique at the starting point. A subsequent search direction is then constructed from the linear combinations of new gradient and the previous direction that minimizes the functional. This way CG technique provides an efficient procedure to minimize the functional. However, CG method needs to be implemented in the direction of maximizing the computational speed and minimizing the memory requirement. This criteria was fulfilled using the CG method developed by Teter $et\ al$ [90].

2.3 VASP Code

Vienna Ab-initio simulation package (VASP) [73] is one of the efficient software packages to perform first-principles calculations based on DFT. It uses pseudo potentials such as PAW or ultrasoft and plane wave basis set. VASP can be used for both static and dynamic simulations. It gives an information about forces, stresses and total energies of an atomic systems. VASP uses the efficient matrix diagnolization schemes and an efficient

pullay/Broyden density mixing. The atoms can be relaxed to their ground state from the known information of forces and stress factors calculated by VASP. Various properties of materials such as electronic, mechanical, optical and magnetic properties etc. can be calculated by using VASP.

VASP has a wide usage in the theoretical community in the field of spin polarized DFT calculations and magnetism. In this thesis, VASP is used to calculate the electronic and magnetic properties of alkali and alkaline earth metals doped AlN systems.

Chapter 3

Electronic and magnetic properties of alkali and alkaline earth metals doped AlN

3.1 Introduction

The prospect of room temperature ferromagnetism in wide band gap semiconductors by doping non-magnetic elements has been paid great attention in recent years for potential spintronic applications, and the progress of those systems is discussed briefly in chapter 1. ZnO and GaN are two such wide band gap semiconductors in which high Curie temperature (T_c) ferromagnetism was attained by doping various non-magnetic elements. Besides ZnO, GaN; AlN is another largest wide band gap semiconductor in group III-V based semiconductors. The discovery of very high T_c of 900 K in Cr doped AlN [91–93]

indicates the possibility of high T_c ferromagnetism in AlN for future spintronic applications. Nevertheless, since there is a problem of magnetic clusters due to TM ions at high concentrations, recently non-magnetic elements have been attracted to achieve high T_c ferromagnetism in AlN [94–98]. The existence of wide band gap and localized nature of 2*p* orbital of N atoms near the valence band of AlN, could provide the magnetism for suitable acceptor doping. Among the non-magnetic element doped AlN systems, Mg doped AlN is one of the fascinating *sp* system and it has already emerged as a crucial technology for optoelectronics device applications. If ferromagnetism exists in such systems, it could be possible to integrate spintronics with opto electronics. According to the work of Dietl $et\ al.$ [5], high Curie temperature ferromagnetism is expected to be feasible in wide band semiconductors for the proper doping of light elements. With this motivation, Wu $et\ al.$ [62] predicted room temperature ferromagnetism in Mg doped AlN by doping Mg in the substitution of Al. Furthermore, the latest experimental observations on Mg doped AlN growing an evidence of room temperature ferromagnetism in Mg doped AlN [70–72], which is discussed briefly in chapter 1. Even though, the theoretical and experimental studies show a strong evidence of ferromagnetism in Mg doped AlN, the origin and nature of ferromagnetism in Mg doped AlN is unclear and it requires great attention to enhance its potential applications for future spintronics. In this chapter, a systematic investigation has been done to identify the origin and mechanism of ferromagnetism in Mg doped bulk AlN. Furthermore, the feasibility of stable magnetic order has been examined for the other alkali and alkaline earth metals doped AlN such as Be doped AlN and K doped AlN, and understand the magnetic phenomena in those systems compared to the magnetic phenomena in Mg doped AlN.

3.2 Computational details

The electronic and magnetic properties of alkali and alkaline earth metals doped AlN have been investigated using first principle calculations based on density functional theory that was implemented in VASP package [73, 99, 100]. PAW potentials are used to account for the interactions between atomic core and the valence electrons. GGA implemented in PBE is adopted for the exchange correlational functional [80]. $3s^2 3p^1$, $2s^2 2p^3$, $3s^2 3p^0$, $2s^2 2p^0$ and $3s3p4s$ electrons are treated as valence electrons for Al, N, Mg, Be and K respectively. The electron wave function is expanded using plane waves with a cutoff energy of 500 eV. A Gamma centered K-point mesh of $4 \times 4 \times 4$ is used for a $3 \times 3 \times 2$ AlN wurtzite supercell to sample the irreducible Brillouin zone. Calculations on $3 \times 3 \times 2$ and $4 \times 4 \times 3$ supercells of Mg doped AlN are produced the same energy difference between the spin polarized and non-spin polarized states and the same magnetic moment. Thus a supercell of $3 \times 3 \times 2$ is found to be sufficient for the study magnetism of Mg doped AlN. Moreover, it was noticed that several studies have successfully reported the magnetism of various semiconductors by using a $3 \times 3 \times 2$ supercell [25, 101, 102]. The positions of all atoms are fully relaxed using the conjugate gradient algorithm [103] until the maximum force on a single atom is less than 0.01 eV/Å. The calculated optimized lattice constants a = 3.13 Å and c = 5.01 Å for the wurtzite AlN are consistent with previous studies [62, 104]. The optimized AlN wurtzite structure with a single dopant X (X = Mg, Be or K) is modelled as shown in Fig. 3.1. The electronegativities of Al, Mg, Be and K are 1.6, 1.3, 1.6 and 0.8 respectively. The formation energy for doping X (X = Mg, Be or K) in the substitution of Al in AlN is calculated from Eq. (3.1).

$$E_{Form} = E_{Dope} - E_{Ideal} + n(\mu_{Al} - \mu_X) \tag{3.1}$$

where E_{dope} and E_{Ideal} are the total energies of doped and undoped AlN respectively. n is the number of X atoms added, or equivalently the number of Al atoms removed. μ_X and μ_{Al} are the chemical potentials of X and Al atoms respectively. The chemical potential of X is considered from its bulk phase as $\mu_X = \mu_X^{Bulk}$. The chemical potential of Al is calculated from the relation,

$$\begin{aligned} \mu_{AlN}^{Bulk} &= \mu_{Al} + \mu_N \ , \\ \mu_{Al} &= \mu_{AlN}^{Bulk} - \mu_N \ , \end{aligned} \tag{3.2}$$

where, $\mu_N = \frac{1}{2}\mu_{N_2}$ and $\mu_{Al} = \mu_{AlN}^{Bulk} - \frac{1}{2}\mu_{N_2}$ [105] at the N-rich condition. Here μ_{AlN}^{Bulk} is considered as the total energy of bulk AlN per unit cell and μ_{N_2} is the total energy of N_2 molecule.

3.3 Results and discussion

3.3.1 Mg doped AlN

A single Mg dopant has been introduced in the substitution of Aluminium (Mg_{Al}), which was predicted as the most stable form [105] compare with the other forms, and some studies noticed the favorability of Mg_{Al} doping in AlN to attain a magnetic ground state [62, 70]. Mg_{Al} is doped in a $3 \times 3 \times 2$ AlN supercell of 72 atoms as shown in Fig. 3.1. Due to the large ionic radius and lower electronegativity of Mg than that of Al, the N atoms surrounding Mg are relaxed outward. This results in a bond length expansion between Mg and its surrounding N atoms N1 (basal) and N2 (c-axis). The bond lengths between Mg to N1 and Mg to N2 are 2.04 Å and 2.06 Å respectively. Whereas in

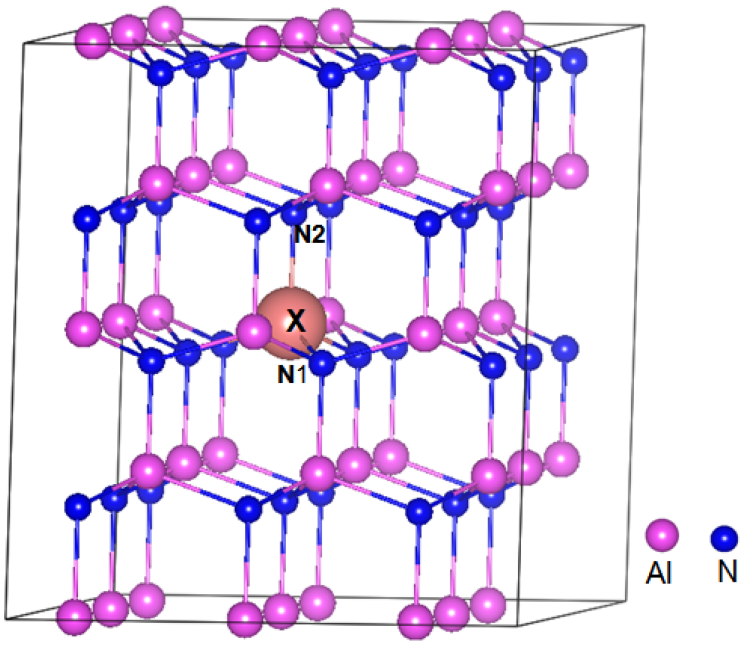

Figure 3.1: The optimized wurtzite AlN $3 \times 3 \times 2$ supercell for a single dopant X (X= Mg, Be or K). Dopant X is highlighted with a big ball irrespective of its atomic size. Aluminium (nitrogen) atoms are shown in pink (blue) color. N1 and N2 are the nitrogen atoms surrounding X at the basal plane and along c-axis respectively.

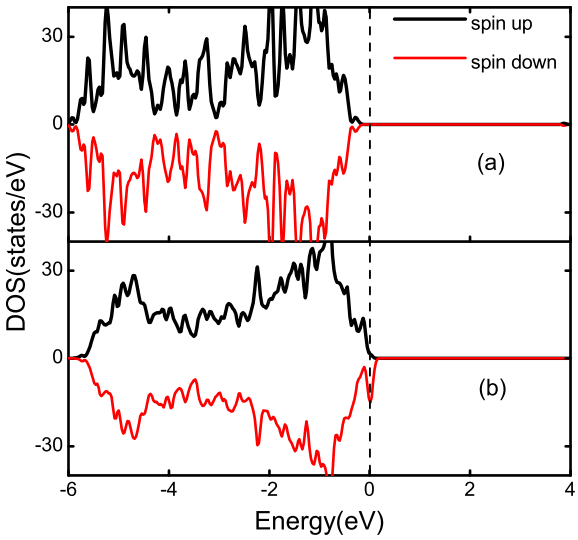

Figure 3.2: Total DOS of ideal AlN (a) and total DOS of Mg doped AlN (b).

ideal AlN, the corresponding bond lengths Al-N1 and Al-N2 are 1.90 Å and 1.91 Å respectively. The changes in the bond lengths due to Mg_{Al} are in good agreement with previous studies [106]. From the total energy calculations, the energy of spin polarized state is found to be 280 meV lower than the energy of non-spin polarized state, indicates the stability of magnetic state in Mg doped AlN. The formation energy of Mg doping in the substitution of Al is calculated from Eq. 3.1 and it is found to be 0.37 eV. This indicates the easiness of doping Mg in AlN. The total density of states (DOS) of both ideal AlN and Mg doped AlN are shown in Fig. 3.2 (a) and 3.2 (b) respectively. The symmetric spin up and spin down states in total DOS of AlN (Fig. 3.2 (a)) shows a non-magnetic behavior. The band gap of AlN is found to be 4.2 eV consistent with the previous studies. Whereas, an imbalance between spin up and spin down states of Mg doped AlN as shown in Fig. 3.2 (b) clearly reveals the magnetic nature of Mg doped

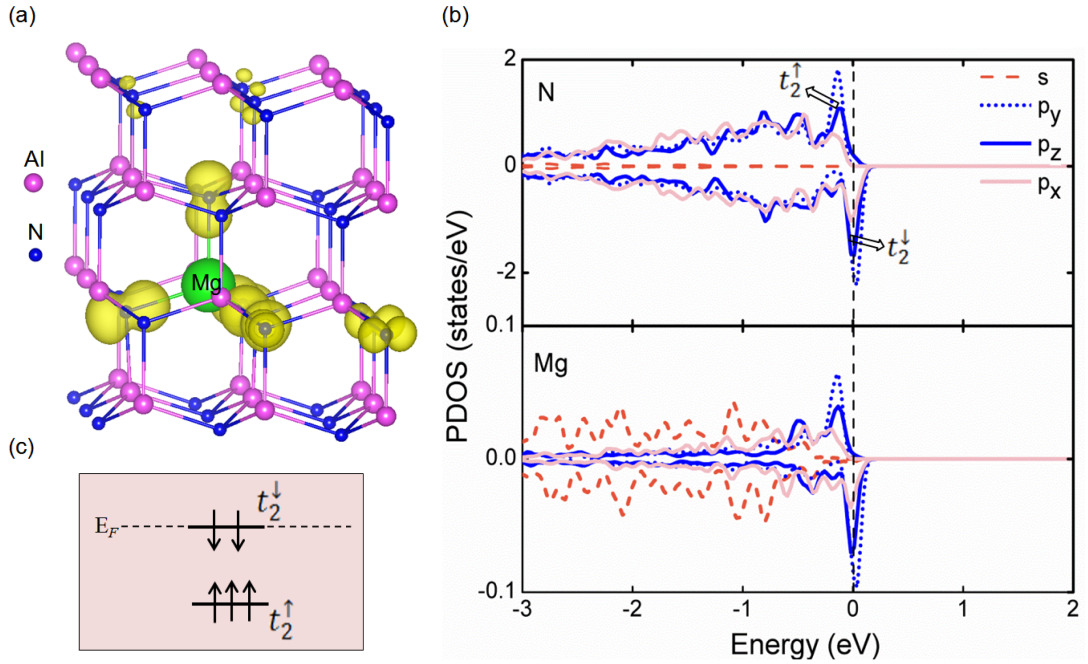

Figure 3.3: Isosurface spin density plot of Mg doped AlN, yellow color represents the net spin density (a), PDOS of sum of N atoms surrounding Mg and Mg atom (b), and schematic energy level diagram of defect levels of Mg-N cluster (c).

AlN. The band gap of Mg doped AlN has been reduced compared to that of AlN due to the defect levels introduced by doping of Mg atom. The Mg_{Al} defect in AlN acts as an acceptor, and gives rise to a magnetic moment of 1 μB due to the hole introduced by Mg. Unlike the other systems [19, 21, 25, 47] in which magnetic moment is mainly contributed by dopant, magnetic moments in Mg doped AlN are prominently dominated by host anions surrounding Mg (Mg-N cluster) as shown in isosurface spin density plot Fig. 3.3 (a). Negligible contribution arises from Mg. From the partial density of states (PDOS) of N and Mg atoms as shown in Fig. 3.3 (b), the defect states around the Fermi level are mainly derived from 2*p* orbitals of N atoms, among which spin down states are partially filled due to the hole introduced by Mg. Furthermore, the overlap of the peaks of N and Mg atoms indicates a kind of *sp-p* interaction between Mg and N atoms, and that interaction prompts the localized magnetic moments on N atoms surrounding Mg.

Although local magnetic moments are realized on Mg-N cluster, it may not necessarily results in the collective magnetism. The magnetic interaction between Mg-N clusters has been analyzed by introducing a pair of Mg atoms at a distance of 5.42 Å. From the calculations, it is realized that the interaction between Mg-N clusters favors ferromagnetic (FM) configuration than antiferromagnetic (AFM) configuration. The energy difference between AFM and FM configuration ($\triangle$E) is found to be 43 meV. The magnetic interaction between Mg-N clusters has been analyzed by examining the energy level diagram of Mg doped AlN with the help of PDOS as shown in Fig. 3.3 (b). The crystal field symmetry in Mg doped AlN is found to be C_{3v} symmetry and it is in agreement with previous study [106]. According to the C_{3v} symmetry of Mg doped AlN, the energy levels split into singly occupied a_2, a_1 states and doubly degenerate *e* state. The a_2 state is mainly derived from *s* orbital, which is occupied and located deep in the valence band.

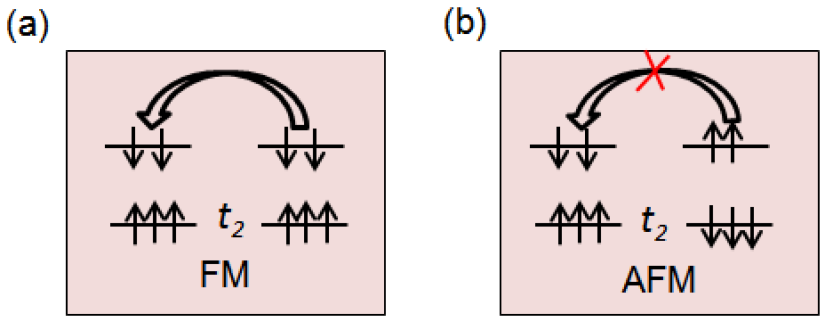

Figure 3.4: Schematic energy level diagrams for ferromagnetic coupling (a) and antiferromagnetic coupling (b) of Mg doped AlN.

Thus we considered that the a_2 state has negligible effect on magnetism. The states a_1 and e are mainly derived from 2p orbitals and located around the Fermi level. Since p_x, p_y and p_z orbitals are almost at the same energy level as shown in Fig. 3.3 (b), we have considered the negligible splitting between a_1 and e states and take it as triply degenerate t_2 state in Fig. 3.3 (b). The spin up t_2 state is completely occupied and spin down t_2 state is partially filled around the Fermi level. The corresponding energy level diagram is shown in Fig. 3.3 (c). Spin up t_2 state is occupied by the three spin up electrons of p_x, p_y and p_z orbitals and spin down t_2 state is partially filled due to the hole introduced by Mg_{Al}.

The interaction between Mg-N clusters has been analyzed based on energy level diagram and hopping mechanism between the defects. From the energy level diagram of Mg doped AlN as shown in Fig. 3.3 (c), the schematic energy level diagrams of the FM and AFM arrangement of Mg-N clusters for the uniform doping of Mg atoms are drawn as shown in Fig. 3.4 (a) and Fig. 3.4 (b) respectively. In the FM coupling, it is realized that the partially filled spin down t_2 states of both Mg-N clusters are degenerate as shown in Fig. 3.4 (a). Since spin down t_2 states are partially filled and degenerate in the FM

coupling, it allows the direct charge hopping between Mg-N clusters and gives the more energy gain than that of AFM coupling. In case of AFM coupling, since parallel spin states are at different energy levels as shown in Fig. 3.4 (b), there is no possibility of direct charge hopping between the parallel spin states, and thus it gives the less energy gain. The possibility of direct charge hopping between degenerate partially filled spin down states of Mg-N clusters, favors the FM ground state in Mg doped AlN. The similar magnetic phenomenon has been noticed in a few systems [56–58], in which the hopping mechanism and energy level splitting among the defect states decide the FM or AFM ground state. The observed magnetic phenomena in Mg doped AlN is expected to be applicable for other alkali (earth) elements doped AlN. The prospect of magnetism in AlN due to the other alkali (earth) metal dopants such as K doped AlN and Be doped AlN will be discussed briefly in the following sections.

3.3.2 K doped AlN

The alkali metal K is introduced in the substitution of Al (K_{Al}) in a $3 \times 3 \times 2$ supercell of AlN similar to the case of Mg doped AlN. Only K_{Al} defect has been considered to analyze the magnetic nature of K doped AlN compared to that of Mg_{Al}. The doping of K_{Al} in AlN introduces an expansion in the bond lengths between K and its surrounding N atoms due to the large ionic radius of K than that of Al. The bond lengths between K-N1 and K-N2 are 2.34 Å and 2.40 Å respectively. The bond lengths between K and N atoms are enhanced than the bond lengths between Mg and N atoms due to the large ionic radius of K compared to the ionic radius of Mg. From the total DOS of K doped AlN as shown in Fig. 3.5 (a), the imbalance between spin up and spin down states

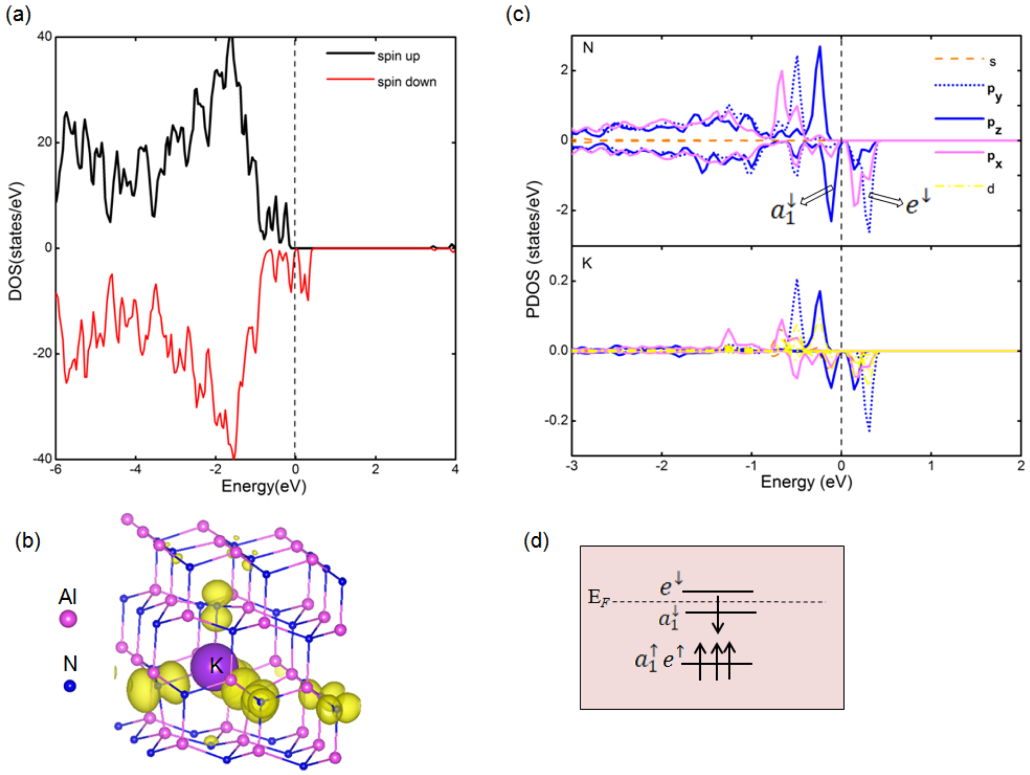

Figure 3.5: Total DOS of K doped AlN (a), isosurface spin density plot (b), PDOS of sum of N atoms surrounding K and K atom (c), and schematic energy level diagram of defect levels of K-N cluster (d).

indicates the magnetic behavior of K doped AlN. A single K_{Al} introduces two holes in AlN and that results in a magnetic moment of 2 μB. The isosurface spin density plot in Fig. 3.5 (b) shows the prominent magnetic contribution of N atoms surrounding K (K-N cluster) and negligible contribution from K. From the PDOS of N and K atoms as shown in Fig. 3.5(c), the states around the Fermi level are mainly derived from 2*p* orbitals of N atoms. The overlap of the peaks between *s* and *p* orbitals of K and 2*p* orbitals of N atoms indicates the existence of *sp*-*p* interaction between K and N atoms similar to the case of Mg doped AlN.

The magnetic interaction among K-N clusters has been examined by introducing a pair of K atoms at a distance of 5.42 Å similar to the case of Mg doped AlN. From the calculations, FM state is found to be more favorable than AFM state with an energy difference of 12 meV. The energy difference between AFM and FM states in K doped AlN is lower compared to that of Mg doped AlN ($\triangle E$ = 43 meV). The magnetic interaction and low stability of ferromagnetism in K doped AlN are analyzed by employing the proposed mechanism that is discussed in the case of Mg doped AlN. For that purpose, the energy level splitting in single K doped AlN is examined with the help of PDOS (Fig. 3.5(c)) and the corresponding schematic energy level diagram is shown in Fig. 3.5(d). Since the ionic radius of K is larger than the ionic radius of Al, noticeable splitting is observed between a_1 and e states in K doped AlN as shown in PDOS (Fig. 3.5(c)).

The splitting between a_1 and e states in K doped AlN has been analyzed from the bonding nature of K atom with its surrounding N atoms. The bond length expansion between K and N2 atoms (N2 atom shown in Fig. 3.1, which is along c-axis) is found to be increased by 2% compared to the bond length expansion between K and N1 atoms (N1 atom shown in Fig. 3.1 and it is in the basal plane). This indicates the strong hybridization between K and basal N atoms compared to the hybridization between K and N2 atom. The p_x, p_y orbitals near the Fermi level shown in Fig. 3.5(c) are mainly derived from the basal N atoms, and the p_z orbital is derived from the N2 atom. Due to the strong hybridization between K and basal N atoms, large splitting is observed between e states derived from p_x, p_y orbitals. While, the splitting is found to be less between a_1 states derived from p_z orbital related to N2 atom. From the analysis of PDOS, a_1 and e states are represented at different energy locations in the energy level diagram as shown in Fig. 3.5(d). The spin up a_1, e states are completely filled and located at the lower

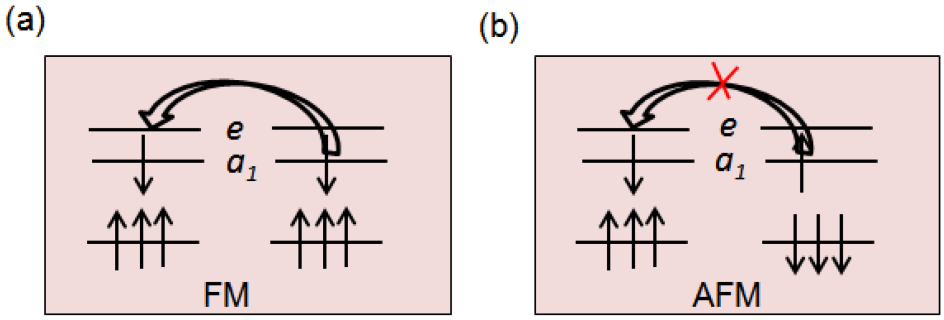

Figure 3.6: Schematic energy level diagrams of ferromagnetic coupling (a) and antiferromagnetic coupling (b) of K doped AlN.

energetic level than the partially filled spin down a_1, e states. Among those spin down states, a_1 state is filled with one electron and located at the lower energetic level of spin down e state. The holes introduced by K are occupied in doubly degenerate spin down e state and results in a magnetic moment of 2 μB. Since spin down a_1, e states are at different energy levels, in FM coupling as shown in Fig. 3.6 (a), it should require some energy to hope the charge from occupied spin down a_1 state to empty spin down e state. On the other hand, there is no possibility of charge hopping between spin up a_1 state to empty spin down e state in AFM coupling as shown in Fig. 3.6 (b). However, the possibility of indirect charge hopping between the other non-degenerate energy levels in AFM coupling, increases the competition between FM and AFM interactions in K doped AlN. Therefore it results in a weak stable FM state ($\triangle$E = 12 meV) in K doped AlN compared to that of Mg doped AlN. The highest energy level is partially filled and degenerate in the case of Mg doped AlN.

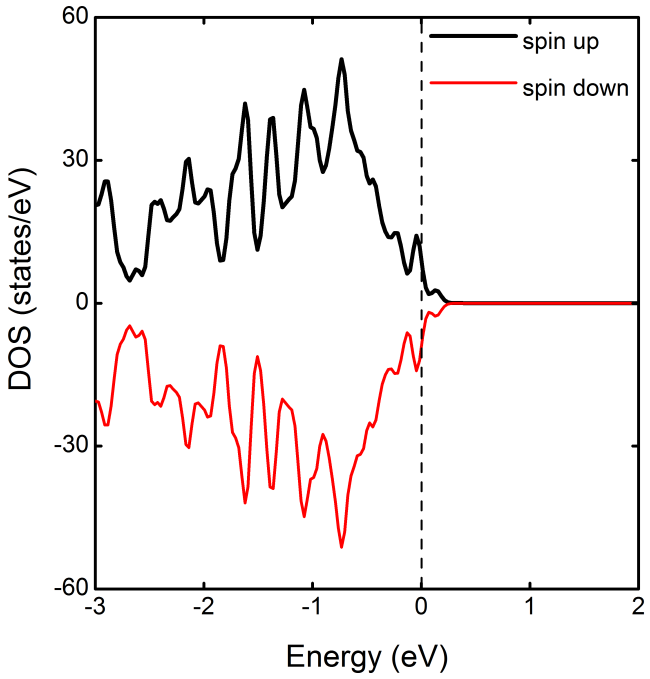

Figure 3.7: Total DOS of Be doped AlN.

3.3.3 Be doped AlN

The similar size of supercell and doping location of Mg in AlN are employed to study the nature of magnetism in case of Be doped AlN. Be is introduced in the substitution of Al (Be_{Al}) and the corresponding bond lengths Be - N1 (basal plane) and Be - N2 are 1.83 Å and 1.89 Å respectively. These bond lengths are found to be short compared to the respective Al-N bond lengths due to the small ionic radius of Be than that of Al. The total DOS of Be doped AlN are shown in Fig. 3.7. The symmetric spin up and spin down states clearly indicates the non-magnetic nature of Be doped AlN, which is different from the case of Mg or K doped AlN systems. The electronegativity and ionic radius of Be play a crucial role for non-magnetic nature in Be doped AlN. Since the electronegativity of Be is same as the electronegativity of Al, Be is also strongly bond

with N like Al. Due to the small ionic radius of Be compared to the ionic radius of Al, the bond length Be-N shrinks upon structural relaxation and forms a strong bonding between Be and N atoms in the valence band. The strong binding of Be atom with N atoms forms the bonding and antibonding states within the host valence band and conduction bands of AlN respectively. Thus there are no gap states allowed in Be doped AlN and that results in no spin polarization. The crucial role of electronegativity and ionic radius of dopants in achieving the magnetic order is seen in various semiconductors [101, 107]. In Mg and K doped AlN systems, Mg and K atoms are weakly interact with N atoms due to the lower electronegativities and also larger ionic radii than that of Al, results in gap states around the Fermi level.

Among Mg, K and Be dopants, the spin polarized states have been realized in AlN due to doping of Mg_{Al} and K_{Al}. The formation energies of doping Mg in AlN and doping of K in AlN are found to be 0.37 eV and 6.13 eV respectively. Since the ionic radius of K is larger than ionic radius of Al and K_{Al} introduces more unpaired electrons to its surrounding N atoms compared to that of Mg_{Al}, the formation energy of doping K in AlN is found to be higher than the formation energy of doping Mg in AlN. The simple comparison of formation energies indicates that Mg is more preferable to be doped in AlN than doping of K in AlN. From the previous studies [108, 109], it was also noticed that the formation energies of doping of Ca or Na atoms in the substitution of Al are found to be high compared to that of doping of Mg_{Al} defect. The large ionic radii of Ca and Na atoms compared to that of Mg atom, and more holes introduced by Na_{Al} defect leads to the high formation energies for the case of Na or Ca doped AlN compared to that of Mg doped AlN. A strong ferromagnetism is also noticed in Mg doped AlN compared to that of K doped AlN. In addition, the latest experimental

observations showed an evidence of room temperature ferromagnetism in Mg doped AlN nanowires and thin films [70–72], which further indicates the intrinsic nature of ferromagnetism in Mg doped AlN. Nevertheless, the theoretical studies are limited and it is challenging to understand the mechanism of magnetism in Mg doped AlN at the low-dimension. Since surface effects play a vital role at the low-dimension, the electronic and magnetic properties of different Mg doped AlN surface orientations such as non-polar, polar and semi-polar surfaces have been systematically investigated and it will be discussed in the subsequent chapters.

3.4 Chapter summary

The holes introduced by Mg_{Al} defect and the existence of partially filled degenerate states derived from Mg-N cluster, stabilize the ferromagnetic ground state in Mg doped AlN. The charge hopping between partially filled spin down states of Mg-N clusters favors ferromagnetic ground state. The magnetic phenomenon that is proposed in the case of Mg doped AlN has been further extended to understand the magnetic behavior of other alkali (earth) metal doped AlN systems. The localized nature and energy level splitting vary from Mg doped AlN to Be and K doped AlN systems due to the different ionic sizes and electronegativities of Mg, K and Be dopants. The energy level splitting in K doped AlN favors weak stable ferromagnetic state compared to that of Mg doped AlN. Unlike Mg and K dopants, Be_{Al} gives zero magnetic moment in AlN due to the strong interaction between Be and host anions in the valence band. The same electronegativity and small ionic radius of Be compared to that of Al, a non-magnetic state has been realized in Be doped AlN. Compare to other dopants, since Mg_{Al} introduces the well

localized nature of defect states, low formation energy and the strong ferromagnetism; Mg doped AlN could be beneficial for future spintronic applications.

Chapter 4

Electronic and magnetic properties of Mg doped AlN non-polar surfaces

4.1 Introduction

In this chapter, electronic and magnetic properties of Mg doped AlN non-polar surfaces have been extensively studied using first-principles calculations. Generally, crystal growth along non-polar semiconductor surfaces is preferable for various applications to avoid the affect of polarization induced by the electric fields. For spintronic applications, several efforts have been put to acquire room temperature ferromagnetism in various semiconductors. Many of the theoretical studies on magnetic semiconductors, examined the origin and nature of magnetism by considering the bulk systems. On the other hand, experimental studies mainly deal with the magnetism at the low-dimension such as

nanostructures, thin films, interfaces/surfaces and nanowires etc. Therefore the theoretical and experimental observations might often give different results on the magnetism and it is illustrated briefly in chapter 1. One of the fascinating example in this direction is Mn doped GaN. The initial theoretical observation was predicted ferromagnetism in Mn doped GaN bulk system [6, 7]. Whereas, experimental observations realized AFM in Mn doped GaN thin films [45]. The dissimilarity between theoretical and experimental observations has been revealed from the theoretical prediction of AFM on Mn doped GaN surface [38, 43]. These theoretical studies predicted that the experimentally observed AFM in Mn doped GaN thinfilms is due to the bond length contraction between Mn atoms on non-polar GaN $(11\bar{2}0)$ surface. With this motivation, several studies considered various non-polar surface orientations of Mn doped GaN and showed the vital role of non-polar surface orientation on the magnetism of Mn doped GaN. Similarly, the contribution of non-polar surface orientation on the magnetism of several magnetic semiconductors was investigated and found the significant changes compared to their bulk structures [38, 43, 47, 50, 110–112]. These studies growing an evidence of crucial role of non-polar surface orientation in the magnetism of magnetic semiconductors at the low-dimension. However, most of the investigations predominantly deal with the influence of surface effects on the magnetism of TM doped semiconductors. To our knowledge, there are no theoretical studies on the magnetism of non-polar surfaces of *sp* based semiconductors such as Mg doped AlN.

The origin and nature of ferromagnetism in Mg doped AlN can be cleared if we able to explore the influence of surface effects on the magnetism of Mg doped AlN. In this chapter, my aim is to identify the origin of magnetism and investigate the crucial role

of non-polar surface orientation on the ferromagnetism of Mg doped AlN. For that purpose, two low indexed non-polar Mg doped AlN surfaces has been considered such as Mg doped AlN $(10\bar{1}0)$ and Mg doped AlN $(11\bar{2}0)$ surfaces. The electronic and magnetic properties of each surface are investigated systematically by consider the following. (1) The electronic structure and mechanism of magnetism due to single Mg dopant on both AlN $(10\bar{1}0)$ and AlN $(11\bar{2}0)$ surfaces, (2) the influence of surface effects on the magnetism of Mg doped AlN along the non-polar surface orientation, and (3) the combined affect of Mg doping and surface factors on the origin and stability of ferromagnetism.

4.2 Computational details

The optimized wurtzite AlN structure with lattice constants a = 3.13 Å and c = 5.014 Å is employed to model the slab of $(10\bar{1}0)$ and $(11\bar{2}0)$ surfaces. All surfaces discussed in the thesis are cleaved from the optimized bulk AlN wurtzite structure. Surface atoms preferred to be relaxed to minimize the surface energy due to breaking of bonds at the surface. All calculations are done by including the structural relaxation of atoms on the surface. A slab model with a thickness of 10 atomic layers and a 2×2 supercell of $(10\bar{1}0)$ surface are adopted for single Mg dopant, which corresponds to a surface Mg coverage of 25%. Similarly, a 2×1 supercell of $(11\bar{2}0)$ surface with a slab of 10 atomic layers is used for doping one Mg and that corresponds to a surface Mg coverage of 25%. A vacuum of 15 Å is set to avoid the interaction between the repeated slabs. The electron wave function is expanded using plane waves with a cutoff energy of 500 eV. A Gamma centered $6 \times 6 \times 1$ K-point mesh is used to sample the irreducible Brillouin zone. Atoms in the bottom four layers of both surfaces are fixed during relaxation process, and the

positions of other atoms are fully relaxed using the conjugate gradient algorithm [103] until the maximum force on a single atom is less than 0.01 eV/Å. A bulk like behavior is attained at the central layers of AlN surfaces, which is defined as the bulk like position in the subsequent discussions. The region immediately below the first atomic layer of the surface is considered as the subsurface location for all surface studies considered in this thesis. A 3×2 and a 2×2 supercells are considered for both Mg doped $(10\bar{1}0)$ and Mg doped $(11\bar{2}0)$ surfaces respectively to study the magnetic interaction between two Mg-N clusters which corresponds to a $\sim$33% surface Mg coverage.

The formation energy of Mg doped AlN surfaces is calculated from Eq. (4.1) [48].

$$E_{Form} = E_{Dope} - E_{Ideal} + n(\mu_{Al} - \mu_{Mg}) \tag{4.1}$$

where E_{Dope} and E_{Ideal} are the total energies of doped and undoped surfaces respectively. n is the number of Mg atoms added, or equivalently the number of Al atoms removed. μ_{Mg} and μ_{Al} are the chemical potentials of Mg and Al atoms respectively. The chemical potential of Mg is considered from its bulk phase as $\mu_{Mg} = \mu_{Mg}^{Bulk}$ and chemical potential of Al is calculated from $\mu_{Al} = \mu_{AlN}^{Bulk} - \frac{1}{2}\mu_{N_2}$ [105]. Here μ_{AlN}^{Bulk} is the total energy of bulk AlN per unit cell and μ_{N_2} is the total energy of N_2 molecule.

4.3 Results and discussion

4.3.1 Pristine AlN non-polar surfaces

A pristine AlN non-polar $(10\bar{1}0)$ surface is shown in Fig. 4.1(a). It has one Al-N pair per surface unit cell and its pristine structure is stable due to the equal number of cations

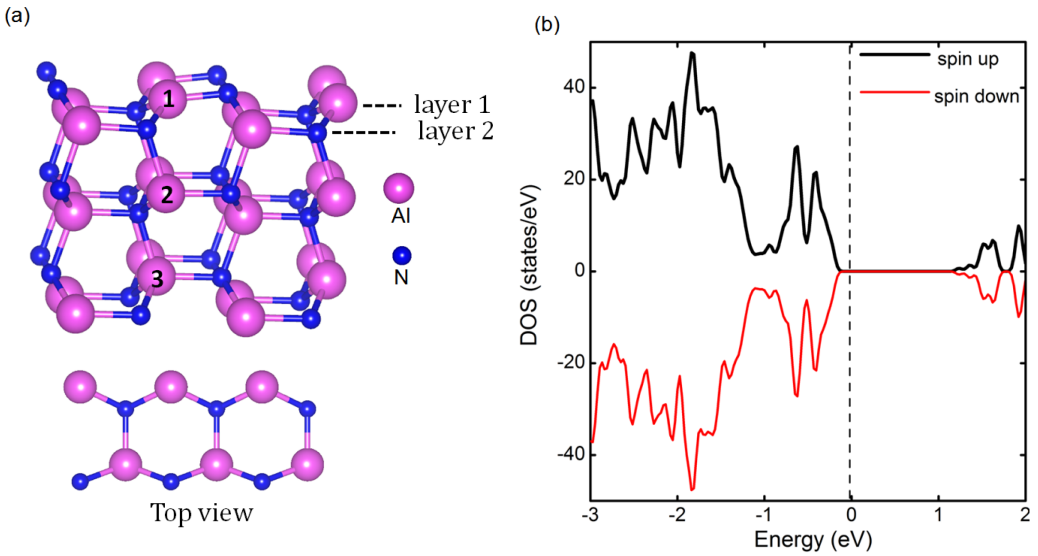

Figure 4.1: Modelling of $(10\bar{1}0)$ surface with different doping locations of Mg represented in numbers and its top view (a), and total DOS of pristine surface (b). Fermi energy is set at zero.

and anions on the surface [113]. Each atom at the surface has three nearest neighbors (three coordinated), and atoms at the central layers (bulk like position) have four nearest neighbors (four coordinated). Surface atoms have large structural relaxation and the bond lengths between Al-N on surface are contracted by 7.4% compare to that of bond lengths at the bulk like position. Upon relaxation, surface N atoms move outward and Al atoms move inward similar to the observation in the previous studies [113]. The existence of equal number of Al and N atoms on pristine $(10\bar{1}0)$ surface neutralizes the charge and results in a non-magnetic behavior. The corresponding total DOS in Fig. 4.1(b) exhibits the symmetric spin up and spin down states. The states near the valence band top are mainly derived from 2*p* orbitals of N atoms.

In case of $(11\bar{2}0)$ surface as shown in Fig. 4.2(a), surface atoms are three coordinated and

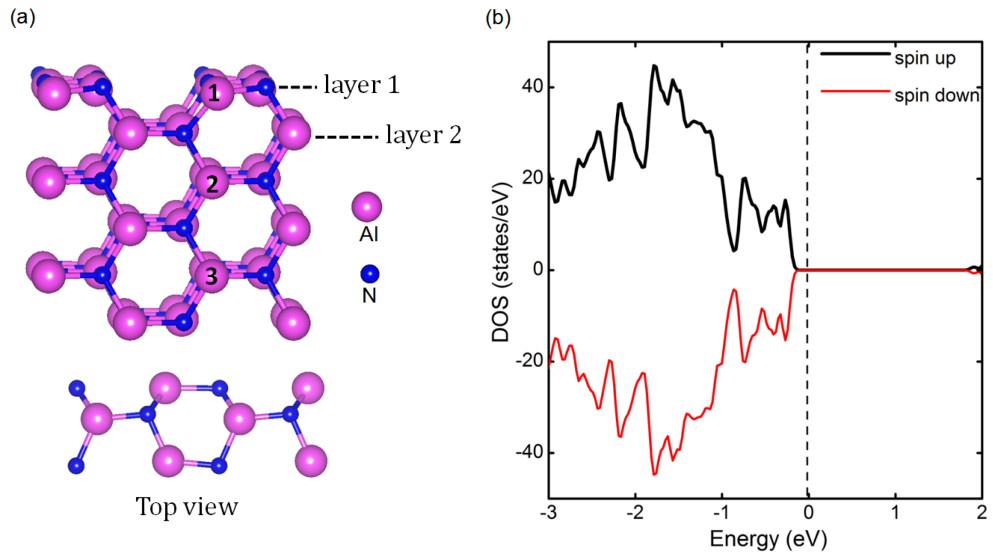

Figure 4.2: Modelling of $(11\bar{2}0)$ surface with different doping locations of Mg represented in numbers and its top view (a), and total DOS of pristine surface (b). Fermi energy is set at zero.

it contains two Al-N pairs on the surface per unit cell. Upon relaxation, the bond length between Al and N atoms on surface contracted by 6% similar to that of $(10\bar{1}0)$ surface. Since $(11\bar{2}0)$ surface has equal number of cations and anions on surface similar to the case of $(10\bar{1}0)$ surface, the charge neutralization results in a non-magnetic behavior. The DOS in Fig. 4.2(b) shows the symmetric spin up and spin down states and reveals the non-magnetic nature of $(11\bar{2}0)$ surface. However these non-magnetic $(10\bar{1}0)$ and $(11\bar{2}0)$ surfaces become spin polarized by doping Mg in the substitution of Al (Mg_{Al}). Interestingly, the energy of FM state is found to be lower than the energy of AFM state for both the Mg doped AlN non-polar surfaces. The electronic and magnetic properties of each Mg doped AlN non-polar surface will be discussed briefly in the following sections.

4.3.2 Mg doped AlN $(10\bar{1}0)$ surface

The 2×2 supercell of AlN $(10\bar{1}0)$ surface is considered for single Mg_{Al} defect. In a slab, Mg_{Al} defect is introduced at different locations such as at surface, subsurface and at the bulk like position as shown in Fig. 4.1(a). The corresponding sites are represented as site 1, site 2 and site 3 respectively. The relative energies for doping Mg at different sites 1, 2 and 3 with respect to site 3 are -1.22 eV, -0.36 eV and 0 eV respectively. The total energy comparison shows that Mg prefers to be doped on surface (site 1). The corresponding formation energy for doping Mg on surface is calculated from Eq. (4.1) and it is found to be -1 eV. The formation energy of introducing Mg_{Al} on AlN surface is found to be lower than that of Mg doping in bulk AlN (E_{form}=0.37 eV) as mentioned in chapter 1. These formation energy values indicate that it is easy to dope Mg on surface compared to that of bulk due to the weak chemical bonding between anions and cations on surface. The spin polarized state on Mg doped $(10\bar{1}0)$ surface is favorable with an energy 260 meV lower than the energy of non-spin polarized state. From DOS as shown in Fig. 4.3 (a), the spin imbalance between spin up and spin down states around the Fermi level exhibits the magnetic nature of Mg doped AlN $(10\bar{1}0)$ surface. Mg_{Al} acts as an acceptor and introduces a hole in AlN that results in a magnetic moment of $0.99\ \mu B$. The magnetic moments are mainly derived from N atoms (N1, N2, N3) surrounding Mg (Mg-N cluster) as shown in Fig. 4.3 (b). The same isosurface density level is applied for all surfaces discussed in the thesis. The change in the valence charge and magnetic moment of N1, N2 and N3 atoms due to the effect of Mg_{Al} are calculated from the bader charge analysis and it is listed in Table (4.1). The less valence charge and more local magnetic moment are realized on surface nitrogen (N1) atom compare to that of other nitrogen atoms (N2, N3). The structural relaxation on Mg doped AlN $(10\bar{1}0)$ surface

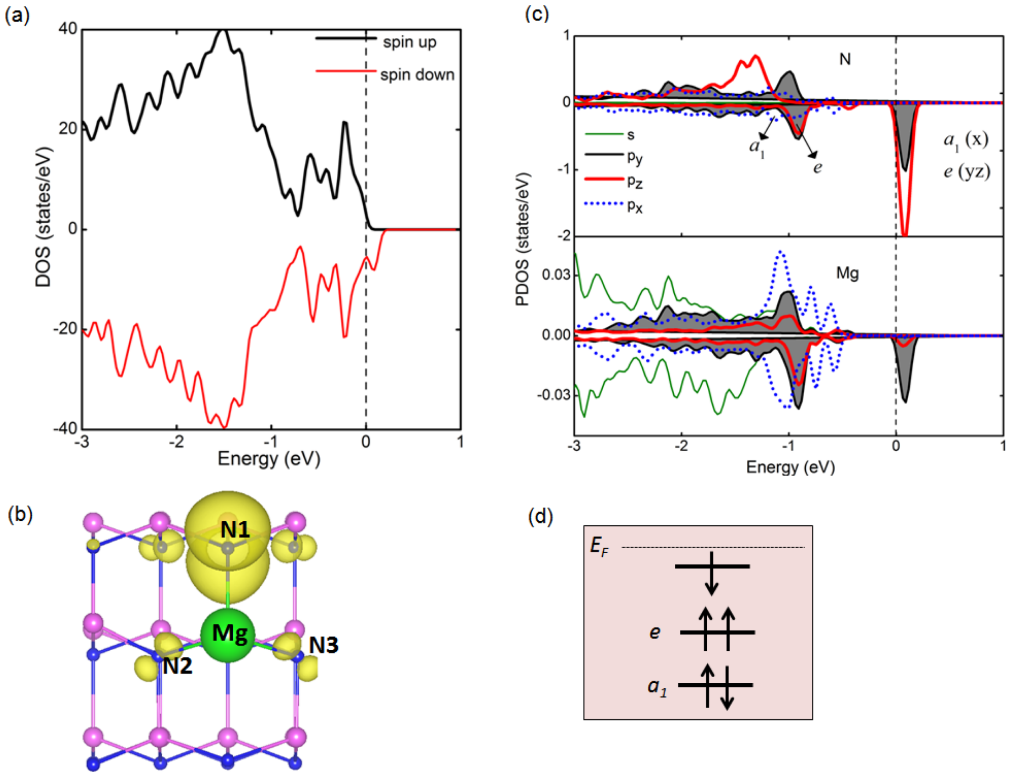

Figure 4.3: Total DOS (a), net spin density plot (b), PDOS of sum of N atoms surrounding Mg and Mg atom (c), and schematic energy level diagram (d) of Mg doped AlN $(10\bar{1}0)$ surface.

expands the bond length between Mg and surface atom N1 by 14.7% and Mg to N2 atom by 7% with respect to corresponding bond lengths between Al and N atoms on pristine AlN surface. This clearly indicates that Mg_{Al} doping strongly influences the surface N1 atom and causes the strong localization of magnetic moment on N1 atom than that of other N2, N3 atoms. As a result, magnetic moments are unequally distributed on Mg doped $(10\bar{1}0)$ surface as shown in Fig. 4.3(b). While in Mg doped bulk AlN, magnetic moments are equally distributed on N atoms surrounding Mg as seen in the previous chapter. In Mg doped AlN $(10\bar{1}0)$ surface, the PDOS of sum of surface N atoms and Mg atom as shown in Fig. 4.3(c), indicates that the defect states are mainly derived from 2*p* orbitals of surface N atoms, and a very less contribution arises from Mg. Moreover, the overlap between the peaks of 2*p* orbitals of N atoms and the *sp* orbital of Mg atom around the Fermi level shows an evidence of *sp-p* interaction between Mg and N atoms, which introduces the local magnetic moments on N atoms.

Although local magnetic moments are realized on Mg doped AlN $(10\bar{1}0)$ surface, it may not necessarily result in the collective magnetism. In order to look at the magnetic interaction between the defects, a pair of Mg atoms are introduced in a 3×2 supercell of $(10\bar{1}0)$ surface that corresponds to a surface Mg coverage of 33%. Since Mg prefers to be doped at the surface, the magnetic interaction between Mg atoms has been investigated around the surface region that is at the top two layers of a slab. The representation of 1^{st} and 2^{nd} layers of a slab is shown in Fig. 4.1(a). The similar type of layer notation is followed for all surfaces considered in this thesis, but the large supercell size is take into account to study the magnetic coupling. On the 1^{st} layer of Mg doped $(10\bar{1}0)$ surface, a pair of Mg atoms are introduced at nearest neighbor distance of 3.13 Å and at next nearest neighbor distance of 5.04 Å. The doping of Mg atoms at a distance of 3.13

Å on the 1st layer, favors the FM ground state with an energy of 12 meV lower than the energy of AFM state. On the same layer, if the Mg atoms doped at a distance of 5.04 Å, the strength of ferromagnetism is further reduced and the corresponding energy difference between FM and AFM states ($\triangle E$) is found to be 3 meV. Interestingly, a strong ferromagnetism is observed in a 2nd layer with $\triangle E$ of 50 meV for a pair of Mg atoms at a 3.13 Å distance. These results indicate the sensitivity of FM stability on Mg doped AlN $(10\bar{1}0)$ surface, and it depends on the distance between Mg atoms and the location of the dopants. In the present study, the doping of one Mg on 1st layer and another Mg on 2nd layer is not considered, because its total energy is 99 meV higher than that of doping of two Mg atoms on 1st layer. This reveals that the doping of two Mg atoms on surface is more favorable than doping of one Mg on 1st layer and another Mg on 2nd layer.

The origin and mechanism of FM stability on Mg doped $(10\bar{1}0)$ surface have been analyzed from the energy level diagram of single defect as shown in Fig. 4.3(d). According to the C_{3v} symmetry of Mg doped AlN, energy levels split into singly occupied a_2, a_1 states and doubly degenerate *e* state. Among those states, a_2 state is mainly derived from *s* orbital and it is located very deep in the valence band. Thus we assume that a_2 state has negligible effect on the magnetism of Mg doped $(10\bar{1}0)$ surface. Whereas, a_1 and *e* states are derived from 2*p* orbitals of N atoms. The a_1 state is occupied by the electrons of p_x orbital, while the doubly degenerate *e* state derived from p_y and p_z orbitals is partially filled as shown in Fig. 4.3(c). Due to the spin polarization effect, *e* state splits into spin up and spin down states. The spin up *e* state is completely occupied and spin down *e* state is partially filled as shown in Fig. 4.3(c). The corresponding schematic energy level diagram is shown in Fig. 4.3(d). Since spin down *e* state is partially filled, there

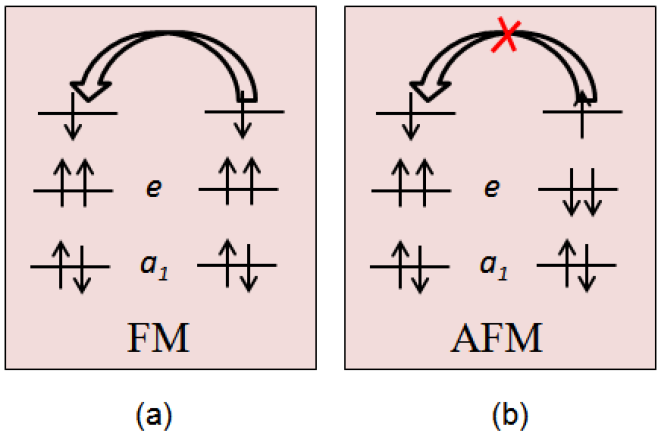

Figure 4.4: Schematic energy level diagrams of ferromagnetic coupling (a) and antiferromagnetic coupling (b) of Mg doped AlN $(10\bar{1}0)$ surface.

is a possibility of direct virtual charge hopping between spin down *e* states in the FM arrangement of Mg-N clusters as shown in Fig. 4.4(a), and thus it results in a more energy gain than that of AFM arrangement. Whereas, in the AFM coupling, parallel spins are at different energy levels as shown in Fig. 4.4(b) and thus it gives less energy gain compare to the case of FM coupling. Hence ferromagnetism is found to be stable than antiferromagnetism on Mg doped AlN $(10\bar{1}0)$ surface at nearest neighbor distance of Mg atoms. Since the defect states are highly localized on Mg doped AlN $(10\bar{1}0)$ surface as shown in Fig. 4.3(b), hopping strength becomes weak as the distance between dopants increases. As a result, a very weak stable FM state is found for the case of Mg atoms at a distance of 5.04 Å, and indicates the short range nature of ferromagnetism on Mg doped $(10\bar{1}0)$ surface.

However, if there is no structural relaxation (unrelaxed) of the atoms on surface, ferromagnetism is found to be more stable on Mg doped $(10\bar{1}0)$ surface with $\triangle E$ of 31 meV for two Mg atoms at 3.13Å distance. Here it is important to notice that the unrelaxed

structure of $(10\bar{1}0)$ surface is a surface cleaved from the bulk AlN, in which atomic relaxation is not considered at the surface. Therefore, the bond lengths between atoms on unrelaxed structure of $(10\bar{1}0)$ surface are analogous to that of bulk AlN. Since the value of $\triangle E$ in the case of unrelaxed structure is different from the $\triangle E$ of relaxed case ($\triangle E$ = 12 meV), both the unrelaxed and relaxed structures of Mg doped $(10\bar{1}0)$ surfaces have been considered to analyze the nature of structural relaxation on the magnetic interaction in Mg doped AlN. The corresponding spin density plots of FM coupling between Mg-N clusters on the 1^{st} layer of Mg doped $(10\bar{1}0)$ surface for the case of relaxed and unrelaxed structures are shown in Fig. 4.5(a) and Fig. 4.5(b) respectively. In the relaxed structure of Mg doped $(10\bar{1}0)$ surface, the bond length between Mg and N atoms on surface is expanded by 4% compared to that of unrelaxed case. The corresponding low spin density overlap region between Mg-N clusters in the relaxed case can be seen in Fig. 4.5(a) compared to that of unrelaxed case in Fig. 4.5(b). The spin density at the overlap region between Mg-N clusters reduces as the distance between Mg atoms increases, which implies that the *sp-p* interaction between Mg-N clusters becomes weak as the distance between Mg atoms increases. Since in the relaxed case, the bond length between Mg and N atoms is expanded by 4% compared to that of unrelaxed case, *sp-p* interaction becomes weaken in the relaxed case than that of unrelaxed case. Therefore, a weak stable FM state ($\triangle E$ = 12 meV) is observed in the relaxed case compared to that of unrelaxed case ($\triangle E$ = 31 meV) on Mg doped AlN $(10\bar{1}0)$ surface. This analysis clearly indicates the sensitivity of magnetic interaction between Mg-N clusters with structural relaxation or with the change in the distance between Mg atoms.

Interestingly, strong ferromagnetism is noticed on the 2^{nd} layer of Mg doped $(10\bar{1}0)$ surface with $\triangle E$ of 50 meV for Mg atoms at 3.13Å distance. This value of $\triangle E$ is high

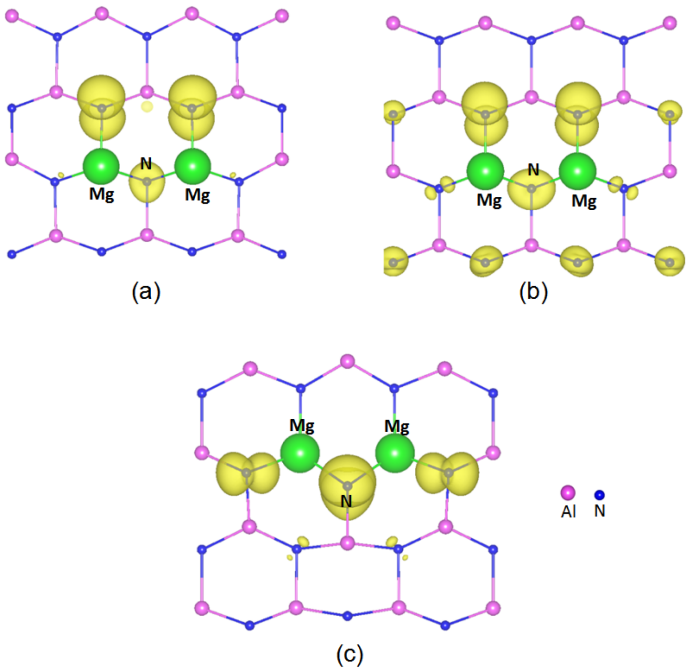

Figure 4.5: Top view of net spin density plot of ferromagnetic coupling between Mg-N clusters on surface with relaxation (a) and without relaxation (b), and Mg-N clusters at subsurface with relaxation (c).

compare to that of 1st layer ($\triangle E$ = 12 meV). The origin of different stable FM states in the 1st and 2nd layers is analysed from the net spin density plots as shown in Fig. 4.5(a) and Fig. 4.5(c) respectively. The Mg-N clusters in the 1st layer are connected by a N atom of low spin density region as shown in Fig. 4.5(a) compare to that of 2nd layer as shown in Fig. 4.5(c). In the 2nd layer, Mg-N clusters are connected by a surface N atom of high spin density and indicates a strong *sp-p* interaction between Mg-N clusters. The strong *sp-p* interaction favors the strong FM state on the 2nd layer than that of 1st layer. The existence of low spin density overlap region or weak *sp-p* interaction between Mg-N clusters results in a weak stable FM state at the 1st layer. This emphasis that the stability of ferromagnetism on Mg doped AlN $(10\bar{1}0)$ surface is not only depends on the distance between Mg atoms but also rely on the way the defects connected to each other. The high to low spin density overlap regions between Mg-N clusters are mainly occurred due to surface effects.

Table 4.1: Charge and magnetic moment (μ) of high spin polarized N atoms surrounding Mg of both Mg doped AlN $(10\bar{1}0)$ and Mg doped AlN $(11\bar{2}0)$ surfaces. μ is the magnetic moment in units of bohr magneton

N atoms	$(10\bar{1}0)$ surface		$(11\bar{2}0)$ surface	
	Charge	μ	Charge	μ
N1	7.13	0.805	7.52	0.459
N2	8.09	0.031	7.58	0.365
N3	8.09	0.031	7.91	0.078

The non-polar $(10\bar{1}0)$ surface orientation of Mg doped AlN favors FM ground state, but FM stability is sensitive with Mg doping location, bond length changes and the distance between Mg atoms. Compare to the case of Mg doped $(10\bar{1}0)$ surface, a strong FM

ground state is realized on Mg doped $(11\bar{2}0)$ surface. The nature of magnetism due to surface effects and the mechanism behind the strong FM state on Mg doped AlN non-polar $(11\bar{2}0)$ surface will be discussed in detail in the following section.

4.3.3 Mg doped AlN $(11\bar{2}0)$ surface

The Mg doping in the substitution of Al introduces the magnetism in AlN $(11\bar{2}0)$ surface. The observed magnetic moment is $\sim$ 1 μB and it is found to be independent of Mg doping location. The site preference of Mg dopant is calculated by introducing Mg at surface (site 1), subsurface (site 2) and at the bulk like position (site 3) as shown in Fig. 4.2(a). The corresponding relative energies of site 1, site 2 and site 3 with respect to site 3 are -0.93 eV, -0.19 eV and 0 eV respectively. These relative energies indicate that Mg atom preferred to be doped on surface compare to the other locations due to the weak bonding between anions and cations on surface, similar to the case of Mg doped $(10\bar{1}0)$ surface. The formation energy for doping Mg_{Al} on surface is found to be -0.7 eV and it shows the capability of Mg doping on surface. The total DOS of Mg doped $(11\bar{2}0)$ surface in Fig. 4.6(a) exhibits the asymmetry between spin up and spin down states and reveals the magnetic behavior of Mg doped AlN $(11\bar{2}0)$ surface. From the net spin density plot as shown in Fig. 4.6(b), magnetic moments are mainly contributed by surface N atoms surrounding Mg. Due to the structural relaxation, Mg_{Al} introduces an expansion in the bond lengths between Mg and its surrounding N atoms (N1, N2, N3). The bond lengths between Mg and its surrounding N atoms N1, N2 and N3 on Mg doped $(11\bar{2}0)$ surface are expanded by 13%, 12% and 10% respectively compare with the bond lengths between Al and N atoms on pristine surface. This bond

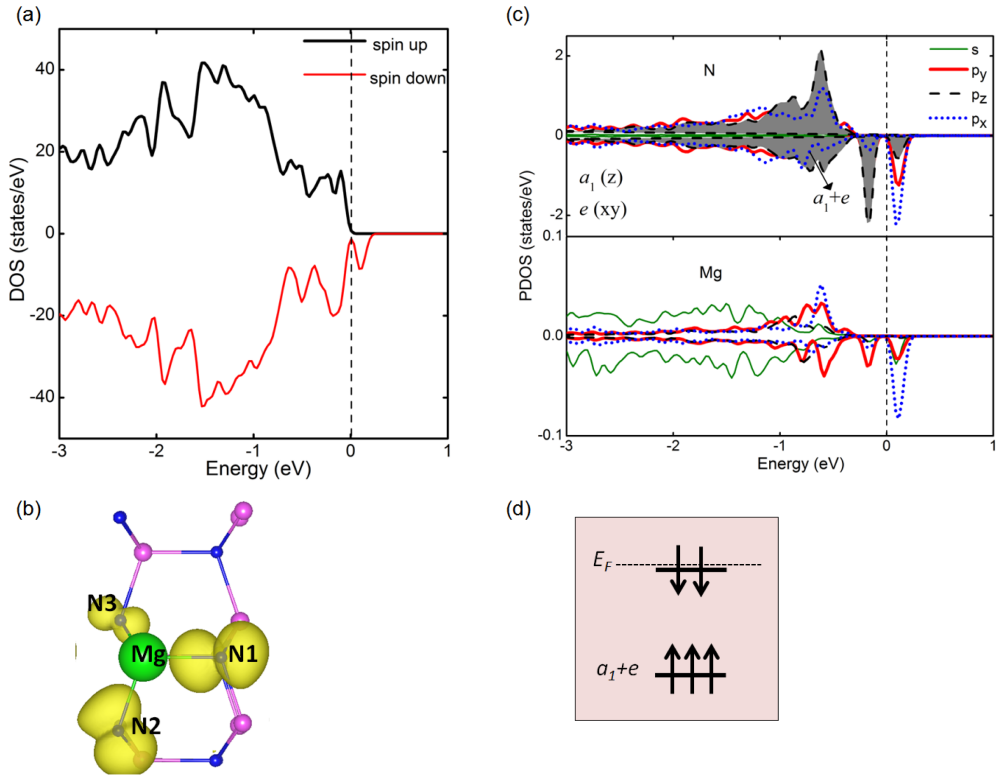

Figure 4.6: Total DOS (a), net spin density plot (b), PDOS of sum of N atoms surrounding Mg and Mg atoms (c), and schematic energy level diagram (d) of Mg doped AlN $(11\bar{2}0)$ surface.

length difference clearly indicates that Mg doping on $(11\bar{2}0)$ surface has large influence on both N1 and N2 surface atoms and introduces the strong localization of magnetic moments compare to that of other N atoms. The magnetic moment and valence charge of N atoms surrounding Mg on $(11\bar{2}0)$ surface are shown in Table (1.1). The valence charge and magnetic moment are found to be same for both surface N atoms (N1 and N2), but negligible magnetic moment arises from N3 atom. The PDOS of spin polarized N and Mg atoms shown in Fig. 4.6(c) exhibits that the magnetic moments are mainly derived from 2*p* orbitals of N atoms. Furthermore, the overlap of the peaks of 2*p* orbitals of N atoms and *sp* orbital of Mg atom reveals a *sp-p* interaction between Mg and its surrounding N atoms.

The magnetic interaction on Mg doped AlN $(11\bar{2}0)$ surface is examined by introducing a pair of Mg atoms at different distances around the surface region. Firstly, two Mg atoms are doped in the 1^{st} layer at various distances such as 3.09 Å, 4.39 Å and 5.4 Å. The energy differences between AFM state and FM state ($\triangle E$) for two Mg atoms at distances 3.09 Å, 4.39 Å and 5.4 Å are found to be 77 meV, 17 meV and -11 meV respectively. These $\triangle E$ values clearly indicate the strong FM nature on Mg doped AlN $(11\bar{2}0)$ surface at the nearest neighbor distance of Mg atoms. The stability of ferromagnetism on Mg doped $(11\bar{2}0)$ surface is high compare to the case of Mg doped $(10\bar{1}0)$ surface. In addition, ferromagnetism remains to be stabilized in the 2^{nd} layer of Mg doped $(11\bar{2}0)$ surface with $\triangle E$ of 75 meV for Mg atoms at 3.09 Å distance. However, the strength of ferromagnetism is decreased as the distance between Mg atoms increases on Mg doped $(11\bar{2}0)$ surface similar to the case of Mg doped $(10\bar{1}0)$ surface.

The mechanism and the origin of strong ferromagnetism on Mg doped AlN $(11\bar{2}0)$

surface have been analyzed by considering energy level diagrams and the charge hopping between Mg-N clusters. From the PDOS of spin polarized atoms as shown in Fig. 4.6(c), the schematic energy level diagram of Mg doped $(11\bar{2}0)$ surface is drawn as in Fig. 4.6(d). Since s orbital of N atoms is located deep in the host valence band of Mg doped $(11\bar{2}0)$ surface, we assumed that the a_2 state derived from s orbital has negligible effect on the magnetic interaction. The defect states around the Fermi level are mainly derived from p_x, p_y and p_z orbitals and these orbitals located at the same energy level on an average. Therefore the combination of a_1 and e states, derived from p_x, p_y and p_z orbitals is represented as triply degenerate a_1+e state in the energy level diagram as shown in Fig. 4.6(d). Due to the spin polarization effect, a_1+e state splits into spin up and spin down states. The spin up a_1+e state is completely filled and spin down a_1+e state is partially filled due to the hole introduced by Mg. The partially filled spin down a_1+e state allows the direct charge hopping between Mg-N clusters in FM coupling as shown in Fig. 4.7(a) and leads to the more energy gain. However in AFM coupling, parallel spins are at different energy levels as shown in Fig. 4.7(b) and thus it weakens the hopping strength due to a super exchange type of interaction. This results in less energy gain in AFM coupling than that of FM coupling, and favors the strong ferromagnetism on Mg doped AlN $(11\bar{2}0)$ surface for Mg pair at nearest neighbor distance. Nevertheless, the strength of ferromagnetism is found to be changed on Mg doped AlN $(11\bar{2}0)$ surface for different distances of Mg atoms. When the distance between Mg atoms increases, the spin density around the overlap region between Mg-N clusters reduces and that weakens the hopping interaction. This results in a weak stable FM state in Mg doped AlN $(11\bar{2}0)$ surface as the distance between Mg atoms increases.

The magnetic phenomena is found to be same for both Mg doped AlN $(11\bar{2}0)$ and Mg

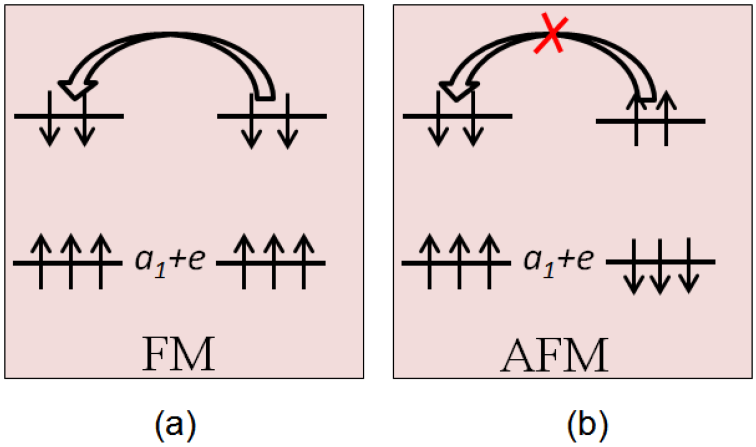

Figure 4.7: Schematic energy level diagrams of ferromagnetic coupling (a) and antiferromagnetic coupling (b) of Mg doped AlN $(11\bar{2}0)$ surface.

doped AlN $(10\bar{1}0)$ surfaces, but the energy level splitting and the corresponding charge hopping between defect levels are different from one surface to other surface. The role of energy level splitting and the localized nature of defect states in stabilizing the ferromagnetism has been analyzed on Mg doped AlN $(11\bar{2}0)$ surface, and compared with the case of Mg doped AlN $(10\bar{1}0)$ surface. The weak stable FM state is realized on Mg doped AlN $(10\bar{1}0)$ surface, while the strength of ferromagnetism is found to be high on Mg doped $(11\bar{2}0)$ surface. From the spin density plots of both Mg doped $(10\bar{1}0)$ and Mg doped $(11\bar{2}0)$ surfaces as shown in Fig. 4.3(b) and Fig. 4.6(b) respectively, it is noticed that the two Mg atoms on $(10\bar{1}0)$ surface can only be connected by N atoms of low spin density region. Whereas, on Mg doped $(11\bar{2}0)$ surface, Mg-N clusters are interacted through surface N atoms of high spin density distribution. The high spin density overlap region between Mg-N clusters on $(11\bar{2}0)$ surface indicates the strong *sp-p* interaction and attains a strong FM state. But the weak *sp-p* interaction or low spin density overlap region between Mg-N clusters on $(10\bar{1}0)$ surface results in a weak stable FM state compare to the case of Mg doped $(11\bar{2}0)$ surface. Moreover in the 2^{nd} layer of Mg doped

$(11\bar{2}0)$ surface, the two Mg atoms are connected by surface N atoms of high spin density and results in a strong FM state. These observations show an evidence that the stability of ferromagnetism depends on the way the Mg atoms connected to each other from one surface to another surface of Mg doped AlN. Since, the localization of magnetic of moments varies from one surface to other surface due to various surface effects, the different stable FM states have been observed.

The mechanism of different stable FM states is further examined in both Mg doped non-polar surfaces from the keen observation of schematic DOS as shown in Figs. 4.8. It is noticed that the separation between occupied and unoccupied spin down states is larger in Mg doped $(10\bar{1}0)$ surface (Fig. 4.8(a)) compare to the case of Mg doped $(11\bar{2}0)$ surface (Fig. 4.8(b)). Therefore in the FM coupling, the virtual charge transfer from occupied to unoccupied spin down states as shown in Figs. 4.8(b) gives more energy gain in Mg doped AlN $(11\bar{2}0)$ surface compare to the case of Mg doped AlN $(10\bar{1}0)$ surface as shown in Fig. 4.8(a). On the other hand, the exchange splitting between occupied spin up and occupied spin down states is more or less similar with the separation between occupied and unoccupied spin down states on Mg doped AlN $(10\bar{1}0)$ surface. Hence, attaining the strong ferromagnetism on Mg doped $(10\bar{1}0)$ surface is rather difficult due to the high competition between FM and AFM interaction. Nevertheless, on Mg doped $(11\bar{2}0)$ surface, the exchange splitting between occupied spin up and occupied spin down states is found to be larger than the separation between occupied and unoccupied spin down states. This weakens the super exchange type of interaction in AFM coupling and reduces the competition between antiferromagnetism and ferromagnetism, leads to the strong ferromagnetism on Mg doped $(11\bar{2}0)$ surface. Even though FM ground state is observed in both Mg doped AlN non-polar surfaces, the strength of ferromagnetism is

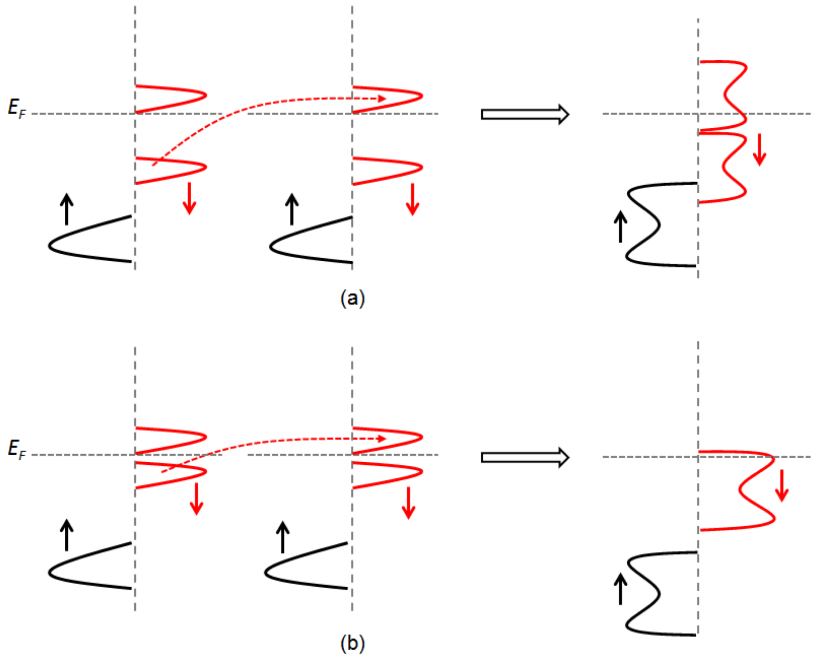

Figure 4.8: Schematic DOS of both Mg doped AlN $(10\bar{1}0)$ surface (a) and Mg doped AlN $(11\bar{2}0)$ surface (b) for the case of ferromagnetic arrangement of Mg-N clusters.

decided by the interplay among different factors such as localized nature of magnetic moments, energy level splitting, distance between the dopants and the *sp-p* interaction between Mg-N clusters etc.

4.4 Chapter summary

The present study reveals the origin and mechanism of ferromagnetism in different Mg doped AlN non-polar surfaces. The charge hopping between partially filled spin down states in both the surfaces favors the ferromagnetic ground state. However the stability of ferromagnetism changes from one surface to the other surface due to different localization of magnetic moments, overlap region between Mg-N clusters and the energy level splitting. In case of Mg doped $(10\bar{1}0)$ surface, the low spin density overlap region or weak *sp-p* interaction between Mg-N clusters result in a weak stable ferromagnetic state. Whereas, the localization of magnetic moments and the high spin density overlap between Mg-N clusters on Mg doped $(11\bar{2}0)$ surface favor a strong ferromagnetic ground state. Unlike the other magnetic semiconductors, non-polar surface orientation stabilizes the ferromagnetic state in Mg doped AlN and indicates the intrinsic nature of ferromagnetism. Since the stability of ferromagnetism is sensitive with the surface effects introduced by Mg doped AlN non-polar surface orientation, strong ferromagnetism might be possible by tuning the surface effects.

Chapter 5

Electronic and magnetic properties of Mg doped AlN polar surfaces

5.1 Introduction

The electronic and magnetic nature of Mg doped AlN polar surfaces have been extensively studied in this chapter to analyze the influence of surface effects on the magnetism of Mg doped AlN in polar surface orientation. Usually nitride based crystals prefer to grow in a polar direction in most of the experiments. The significant changes in the electronic and magnetic properties have been observed in various systems along polar surface orientation [39, 40, 42, 114–116]. Similarly, the electronic and magnetic properties of Mg doped AlN may vary along polar surface orientation.

In this chapter, one of the low indexed polar surface of AlN such as $(000\bar{1})$ surface has

been considered. The polar surface orientations contain dangling bonds (DBs) especially on the surface of nitride based semiconductors. These unsaturated DBs favored to be reconstructed or passivated to minimize the surface energy [117]. The stable reconstructed or passivated surfaces can be determine by following the electron counting model [118]. The variation in the electronic and magnetic properties has been observed in several magnetic semiconductor polar surfaces [120, 121] due to effect of passivation and reconstruction. Therefore, both passivated and reconstructed Mg doped AlN $(000\bar{1})$ surfaces have been considered in order to understand the origin of magnetism and the effect of passivation and reconstruction on the electronic and magnetic properties of polar surfaces of nitrides. In the passivated $(000\bar{1})$ surface, the DBs are saturated by pseudo hydrogen atoms [119]. The $(000\bar{1})$ surface is reconstructed by considering Al adatom that is bonded to three N atoms on surface such as Al at H3 location, which was predicted as the most stable reconstructed $(000\bar{1})$ surface for all Al-chemical potential range [113].

5.2 Computational details

The optimized wurtzite AlN structure with lattice constants a = 3.13 Å and c = 5.014 Å is used to model the passivated $(000\bar{1})$ surface (p-$(000\bar{1})$ surface) and reconstructed $(000\bar{1})$ surface (r-$(000\bar{1})$ surface). A slab model with a thickness of 10 atomic layers in a 2×2 supercell is considered for a single defect in both p-$(000\bar{1})$ and r-$(000\bar{1})$ surfaces. The electron wave function is expanded using plane waves with a cutoff energy of 500 eV. A Gamma centered $6\times6\times1$ K-point meshes are adopted to sample the irreducible Brillouin zone. A 3×3 supercell of p-$(000\bar{1})$ surface and a 4×4 supercell of r-$(000\bar{1})$ surface

are considered to analyze the magnetic interaction between two Mg dopants. In these supercells, the incorporation of two Mg atoms corresponds to a surface Mg coverage of 22% and 25% for Mg doped p-$(000\bar{1})$ and Mg doped r-$(000\bar{1})$ surfaces respectively. In addition, a vacuum region of 12 Å is used to minimize the interaction of adjacent surfaces. During the relaxation process, atoms in the bottom four layers of all surfaces are fixed, and the positions of other atoms are fully relaxed using the conjugate gradient algorithm [103] until the maximum force on a single atom is less than 0.01 eV/Å. A bulk like behavior is attained at the central layers.

5.3 Results and discussion

5.3.1 Pristine, passivated and reconstructed AlN $(000\bar{1})$ surfaces

The pristine AlN polar $(000\bar{1})$ surface contains only one type of ion on top layer of the surface as shown in Fig. 5.1(a). In principle, the termination with less number of unsaturated bonds is considered as the most stable one [114] and thus $(000\bar{1})$ surface with N-termination is identified as the most stable surface. The DBs of surface N atoms results in a magnetic moment of $2\ \mu B$ for a 2×2 supercell of pristine $(000\bar{1})$ surface. The total DOS in Fig. 5.1(b) exhibits an imbalance between spin up and spin down states around the Fermi level and indicates the magnetic nature of a surface. The inset of Fig. 5.1(b) shows the net spin density of $(000\bar{1})$ surface, in which magnetic moments are mainly localized around the DBs of surface N atoms. Even though magnetism is observed in pristine AlN $(000\bar{1})$ surface, magnetism due to surface DBs is not usually stable. Since our intension is to identify the origin of magnetism due to Mg_{Al}, the DBs

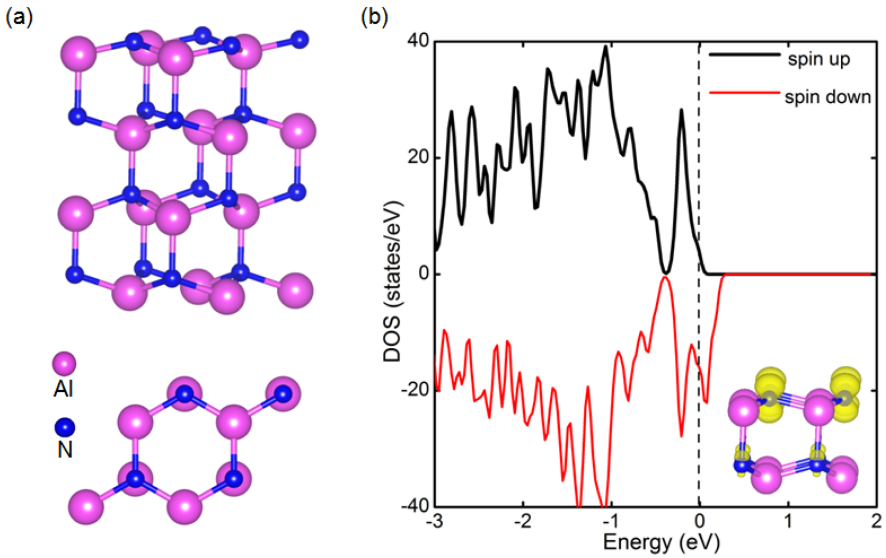

Figure 5.1: Modelling of pristine $(000\bar{1})$ surface and its top view (bottom picture) (a), the corresponding total DOS (b) and inset of (b) shows the net spin density plot.

of pristine AlN $(000\bar{1})$ surface are saturated by passivation and reconstruction.

A pseudo hydrogen of charge 0.75 *es* is considered to saturate the DBs of each surface N atom of $(000\bar{1})$ surface and the resultant p-$(000\bar{1})$ surface is shown in Fig. 5.2(a). The corresponding DOS of p-$(000\bar{1})$ surface in Fig. 5.2(b) shows the symmetric spin up and spin down states and indicates the non-magnetic nature. Similarly, the r-$(000\bar{1})$ surface, in which one Al atom added at the hallow position of three surface N atoms as shown in Fig. 5.2(c) saturates the DBs of pristine surface. The corresponding total DOS of r-$(000\bar{1})$ surface as shown in Fig. 5.2(d) exhibits the non-magnetic nature.

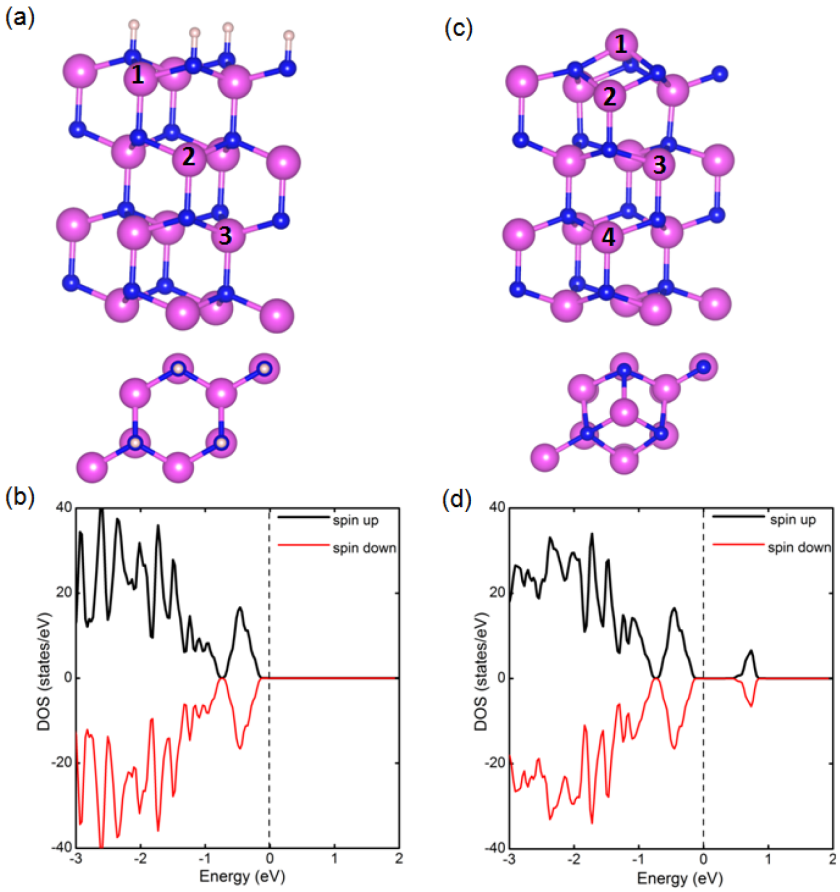

Figure 5.2: Modelling of passivated $(000\bar{1})$ surface with different doping locations of Mg represented in numbers and its topview (a), total DOS of passivated $(000\bar{1})$ surface (b), modelling of reconstructed $(000\bar{1})$ surface with different doping locations of Mg represented in numbers and its topview (c), and total DOS of reconstructed AlN $(000\bar{1})$ surface (d).

5.3.2 Mg doped passivated AlN $(000\bar{1})$ surface

Firstly, a single Mg atom is introduced in the substitution of Al at different locations of a non-magnetic p-$(000\bar{1})$ surface of AlN as shown in Fig. 5.2(a). The sites 1, 2 and 3 in a p-$(000\bar{1})$ slab represent the doping sites of Mg at surface, subsurface and at the bulk like position respectively. The relative energies for doping Mg at sites 1, 2 and 3 with respect to site 3 are 0.02 eV, -0.1 eV, 0 eV respectively. These relative energies indicate that the Mg prefers to be doped at site 2 compared to other locations. The Mg_{Al} defect results in a net magnetic moment of $0.9\ \mu B$ irrespective of any doping locations in a slab. The formation energy for doping Mg on subsurface is calculated from Eq. (4.1) and it is found to be 0.14 eV. The total DOS of Mg doped at subsurface is shown in Fig. 5.3(a). The asymmetric spin up and spin down states show the magnetic behavior, in which spin up states are completely filled and spin down states are partially filled around the Fermi level. The magnetic moments are mainly localized on N atoms (N1, N2, N3) surrounding Mg as shown in Fig. 5.3(b). Due to the same coordination of N atoms, magnetic moments are equally distributed on N atoms surrounding Mg, and the localized nature of magnetic moments on Mg doped p-$(000\bar{1})$ surface is found to be similar with the case of Mg doped bulk AlN. The states around the Fermi level are mainly derived from 2*p* orbitals of N atoms as shown in PDOS (Fig. 5.3(c)). The partially filled spin down states are prominently derived from p_x, p_y orbitals and the negligible contribution raised from the p_z orbital. The overlap between the peaks of *s* and *p* orbital of Mg and *p* orbital of N atoms clearly shows the *sp*-*p* interaction between Mg and N atoms similar to the case of Mg doped AlN non-polar surfaces.

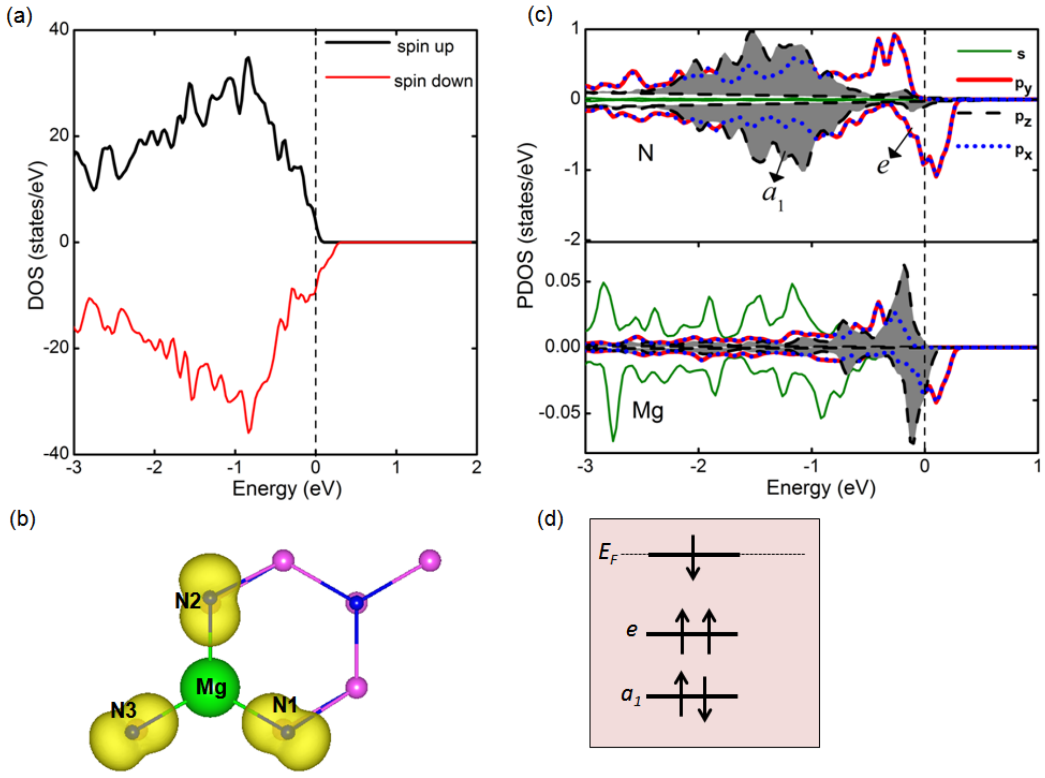

Figure 5.3: Total DOS (a), net spin density plot (b), PDOS of sum of N atoms surrounding Mg and Mg atoms (c), and schematic energy level diagram (d) of Mg doped passivated AlN $(000\bar{1})$ surface.

The mechanism behind the magnetic coupling between Mg-N clusters on Mg doped p-$(000\bar{1})$ surface needs to be cleared for the collective magnetism, even though we have found localized magnetic moments on N atoms surrounding Mg. The magnetic interaction between Mg-N clusters has been considered at different locations of a slab such as at surface, subsurface and at the bulk like position for two Mg atoms at a distance of 3.13 Å. The energy differences between AFM and FM states ($\triangle E$) at surface, subsurface, and at bulk like position are found to be 44 meV, 49 meV and 56 meV respectively. Since these $\triangle E$ values are greater than the thermal energy at room temperature (K_BT = 26 meV), it is possible to get strong ferromagnetism at any location of Mg doped AlN p-$(000\bar{1})$ surface. In order to analyze the magnetic interaction among Mg-N clusters, firstly the energy level diagram of Mg doped p-$(000\bar{1})$ surface has been examined. From the PDOS as shown in Fig. 5.3(c), *s* orbital is located deep in the valence band and thus the effect of a_2 state derived from *s* orbital is neglected in the magnetic interaction similar to the case of Mg doped non-polar surfaces. Among p orbitals, spin up and spin down states derived from p_z orbital are filled, and the state corresponding to p_z orbital is considered as singly occupied a_1 state. The partially filled states are prominently derived from p_x, p_y orbitals and located at the same energy level. The state derived from p_x, p_y orbitals is considered as doubly degenerate *e* state. Due to the spin polarization effect, the *e* state splits into spin up and spin down states, in which spin up *e* state is occupied by two electrons of p_x, p_y orbitals and spin down *e* state is partially filled due to the hole created by Mg_{Al}. The corresponding energy level diagram of Mg doped p-$(000\bar{1})$ surface is shown in Fig. 5.3(d). The a_1 state, occupied by two electrons of p_z orbital is located at the lower energetic level than partially filled *e* state. Since spin down *e* state is partially filled around the Fermi level, there is a possibility of virtual charge hopping between spin down *e* states of Mg-N clusters in FM coupling as shown in Fig. 5.4(a).

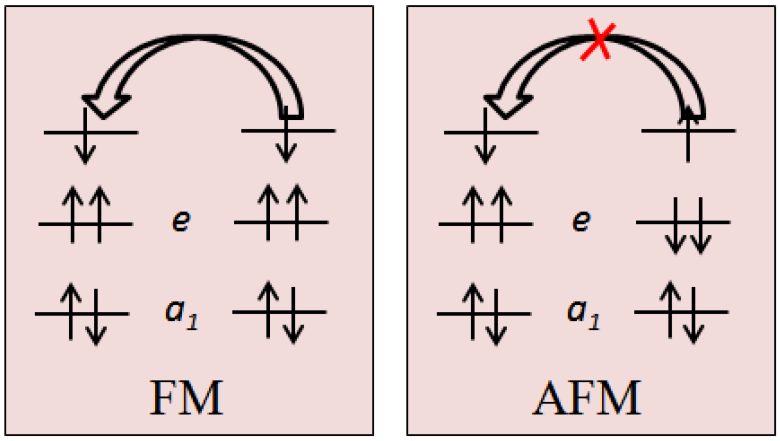

Figure 5.4: Schematic energy level diagrams of ferromagnetic coupling (a) and antiferromagnetic coupling (b) of Mg doped passivated AlN $(000\bar{1})$ surface.

Whereas, in AFM coupling, since parallel spins are at different energy levels, there is no possibility of direct charge hopping between the states of parallel spins as shown in Fig. 5.4(b). This leads to a low energy gain in AFM coupling than that of FM coupling, and results in a stable FM ground state on Mg doped AlN p-$(000\bar{1})$ surface. The stability of ferromagnetism corresponding to two Mg atoms at a nearest neighbor distance is found to be same at any location on surface due to the same chemical environment. Since the energy difference between AFM and FM states is in the range of ∼40-50 meV, and it is similar with that of Mg doped bulk AlN [62], there is a possible route to attain room temperature ferromagnetism in Mg doped p-$(000\bar{1})$ surface.

5.3.3 Mg doped reconstructed AlN $(000\bar{1})$ surface

The Mg_{Al} defect has been introduced at different locations in a non-magnetic reconstructed $(000\bar{1})$ surface (r-$(000\bar{1})$ surface) of AlN as shown in Fig. 5.2(c). The sites 1,

2, 3 and 4 represent the doping locations of Mg at reconstructed position, surface, sub-surface and at the bulk like position respectively. The relative total energies for doping Mg_{Al} at sites 1, 2, 3 and 4 with respect to site 4 are -2.46 eV,-0.45 eV,-0.26 eV and 0 eV respectively. These relative energies clearly show that Mg prefers to be doped at reconstructed position compared to the other locations. The corresponding formation energy is found to be -1.09 eV, and exhibits the easiness of doping Mg on surface compared to the case of Mg doped bulk AlN. The total DOS of Mg doped r-$(000\bar{1})$ surface is shown in Fig. 5.5(a). The imbalance between spin up and spin down states around the Fermi level indicates the magnetic nature of the surface. The spin up states are completely filled and spin down states are partially filled due to the hole created by Mg and results in a magnetic moment of $\sim\ 0.99\ \mu B$. The net spin density plot in Fig. 5.5(b) shows that the magnetic moments are mainly localized on lower coordinated surface N atoms near Mg. The surface N atoms (N1, N2, N3) surrounding Mg are strongly bind to Mg and forms a type of closed shell structure. These atoms take enough charge from Mg and transfers the hole to lower coordinated surface N atom (N4). Hence, the magnetic moments are unequally distributed on N atoms of Mg doped r-$(000\bar{1})$ surface due to the different coordination, compared to the case of Mg doped p-$(000\bar{1})$ surface. Different from non-polar surfaces, the defect states on Mg doped r-$(000\bar{1})$ surface have more extended nature due to the Mg_{Al} at reconstructed position, which acts like an adatom. Generally, it was believed that the adatoms on surface have more extending nature [120] due to a different type of chemical environment compared to the case of pristine surfaces. From PDOS of surface N atom and Mg atom as shown in Fig. 5.5(c), the states around the Fermi level are mainly derived from *p* orbitals of N atoms and the magnetic moment is prominently localized on surface N atom (N4). Even though, there is no much overlap between the

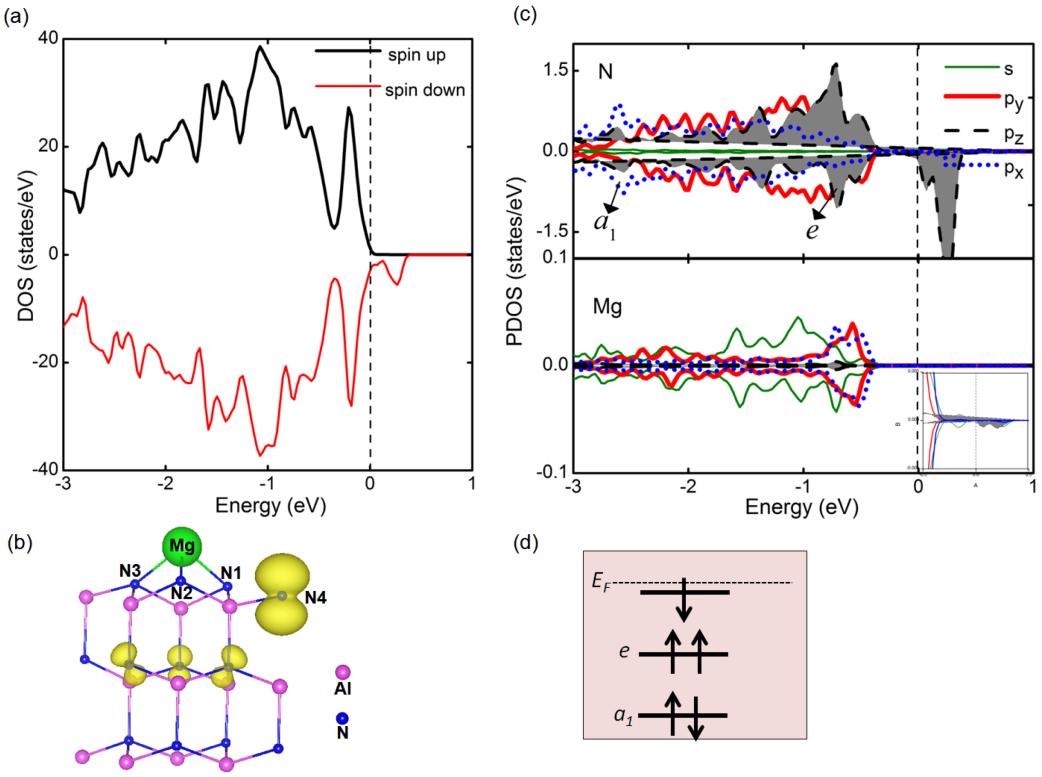

Figure 5.5: Total DOS (a), net spin density plot (b), PDOS of sum of N atoms surrounding Mg and Mg atoms (c), and schematic energy level diagram (d) of Mg doped reconstructed AlN $(000\bar{1})$ surface.

peaks of orbitals of Mg and N4 atoms as shown in inset of Fig. 5.5(c), the strong interaction between Mg to N1, N2 and N3 atoms causes the transfer of hole from Mg to N4 atom. This results in a more extended nature of defect states in Mg doped r-$(000\bar{1})$ surface. The surface environment and localized nature of magnetic moments on Mg doped r-$(000\bar{1})$ surface are found to be significantly different from Mg doped p-$(000\bar{1})$ surface and Mg doped non-polar surfaces. For Mg doped non-polar and Mg doped p-$(000\bar{1})$ surfaces, the magnetic moments are mainly localized on N atoms near to Mg. Whereas for Mg doped r-$(000\bar{1})$ surface, the magnetic moments are prominently dominated by lower coordinated surface N atom rather than N atoms near Mg. These results indicate that the reconstruction significantly changes the localized nature of magnetism on Mg doped r-$(000\bar{1})$ surface, different from the case of Mg doped p-$(000\bar{1})$ surface. Hence, it is very crucial to take it into account the crystal growth condition that is whether the film is reconstructed or passivated in order to understand the nature of magnetism at the low-dimension especially for the case of nitride based magnetic semiconductors.

The magnetic interaction between Mg-N clusters is analyzed on Mg doped r-$(000\bar{1})$ surface by considering Mg atoms at the most favorable location of the surface. Since Mg prefers to be doped at reconstructed location compared to other locations, four Mg atoms are introduced at a reconstructed positions in a 4×4 supercell with a distance of $6.26\mathring{A}$. The doping of four Mg atoms in a 4×4 supercell corresponds to a surface Mg coverage of 25%. Interestingly, a strong ferromagnetism is observed with an energy difference $\triangle E$ of 146 meV. The mechanism of this strong ferromagnetism has been analyzed using energy level diagrams. From PDOS of spin polarized N atoms of Mg doped r-$(000\bar{1})$ surface as shown in Fig. 5.5(c), *s* orbital is located deep in valence band and thus it was neglected in the magnetic interaction. The defect states near the Fermi level of Mg doped

r-$(000\bar{1})$ surface are prominently derived from 2*p* orbitals of N atoms, which are split into singly occupied a_1 state and doubly degenerate *e* state. Among those states, a_1 state is completely filled by the electrons of p_x orbital as shown in PDOS (Fig. 5.5(c)). The doubly degenerate *e* state is partially filled due to the unpaired electrons in p_z orbital. The corresponding schematic energy level diagram of Mg doped r-$(000\bar{1})$ surface is shown in Fig. 5.5(d). Since the spin down *e* state is partially filled, there is a possibility of charge hopping between parallel spin down states of Mg-N clusters and results in a stable FM ground state similar to that of other surfaces. Since Mg at reconstructed position acts like an adatom, and Mg_{Al} introduces the localized magnetic moments on N4 atom rather than N atoms (N1, N2, N3) near Mg, the FM state remains stabilized on Mg doped r-$(000\bar{1})$ surface for Mg atoms doped at a distance of ~ 6 $\mathring{A}$.

5.4 Chapter summary

In this chapter, the electronic and magnetic properties of Mg doped AlN have been investigated in a polar surface orientation with different surface environments such as passivation and reconstruction. The passivated Mg doped AlN surface introduces an equal distribution of magnetic moments on N atoms surrounding Mg similar to that of Mg doped bulk AlN. Whereas in case of Mg doped reconstructed surface, the magnetic moments are unequally distributed on N atoms due to different coordination. Ferromagnetism is found to be stable in both Mg doped passivated and reconstructed $(000\bar{1})$ surfaces due to the possibility of charge hopping between defect levels of parallel spin. Nevertheless, the stability of ferromagnetism is significantly varied from Mg doped passivated to Mg doped reconstructed surfaces. The Mg atom at reconstructed position

behaves like an adatom and results in a long ranged ferromagnetic state due to the extended nature of defect state.

The existence of ferromagnetic ground state in both Mg doped passivated and Mg doped reconstructed AlN $(000\bar{1})$ surfaces further supports the intrinsic nature of ferromagnetism in Mg doped AlN. Since the ferromagnetic stability changes with the surface environment of Mg doped AlN, it is very crucial to take into account the crystal growth condition in order to understand the nature of ferromagnetism. The sensitivity of stability of ferromagnetism with the surface environment of Mg doped AlN polar surface, paves a way to get strong ferromagnetism by tuning the surface effects.

Chapter 6

Electronic and magnetic properties of Mg doped AlN semi-polar surfaces

6.1 Introduction

In recent years, several theoretical studies on magnetic semiconductors are mainly investigated the magnetism along non-polar or polar surface orientations. Other than non-polar and polar surfaces of magnetic semiconductors, the semi-polar surface orientation could also have an effect on the magnetic property. The recent experimental study proposed that the semi-polar $(10\bar{1}1)$ orientation might also have an impact on the FM behavior of Mg doped AlN zigzag nanowires [70]. To date, as of our knowledge there were no theoretical studies on the magnetism of semi-polar surfaces of magnetic semiconductors. Usually, the modeling of semi-polar surfaces of wurtzite semiconductors is

a challenging due to their complex crystal structures. Nevertheless, the theoretical aspect of magnetism along semi-polar orientation and its contribution to the magnetism of Mg doped AlN need to be cleared for practical applications. Therefore in this chapter, I have tried to shed the insights of the electronic and magnetic properties of Mg doped AlN semi-polar $(10\bar{1}1)$ surface.

6.2 Computational details

The optimized wurtzite AlN structure with lattice constants a = 3.13 Å and c = 5.014 Å is used to model the slab of $(10\bar{1}1)$ surface. A slab model with a thickness of 10 atomic layers and a 1×3 supercell are considered for a single defect in passivated $(10\bar{1}1)$ surface. The electron wave function is expanded using plane waves with a cutoff energy of 500 eV. A Gamma centered $6 \times 4 \times 1$ K-point meshes are used to sample the irreducible Brillouin zone. The magnetic interaction between two Mg atoms has been analyzed in a 2×3 supercell of passivated Mg doped $(10\bar{1}1)$ surface, which corresponds to a surface Mg coverage of 33%. In addition, a vacuum region of 12 Å is adopted to minimize the interaction of adjacent surfaces. During relaxation process, atoms in the bottom four layers of all surfaces are fixed, and the positions of other atoms are fully relaxed using the conjugate gradient algorithm [103] until the maximum force on a single atom is less than 0.01 eV/Å. A bulk like behavior is attained at the central layers.

6.3 Results and discussion

6.3.1 Pristine and passivated AlN $(10\bar{1}1)$ semi-polar surfaces

The pristine AlN semi-polar $(10\bar{1}1)$ surface contains same type of ions with different coordination on the surface as shown in Fig. 6.1 (a). Since N-termination contains less number of dangling bonds (DBs) than Al-termination, the N terminated $(10\bar{1}1)$ surface is considered. The surface environment on semi-polar surface is different from non-polar surface and polar surfaces. In non-polar surfaces, the top layer of the surface contains Al-N pair, and polar surfaces contain one type of ion with same coordination at the top layer, which is seen in the previous chapters. Unlike the non-polar and polar surfaces of AlN, the N-terminated semi-polar $(10\bar{1}1)$ surface contains two different coordinated anions N1 and N2 per unit cell as shown in Fig. 6.1 (a). N1 and N2 are two coordinated and three coordinated atoms respectively, which contain net DBs. Whereas, at the central layers that is at the bulk like position of a $(10\bar{1}1)$ slab, N atom is four coordinated. Due to the DBs of surface N atoms, the pristine $(10\bar{1}1)$ surface results in a magnetic moment of 2.25 μB per 1×1 supercell. The corresponding DOS in Fig. 6.1(b) shows the asymmetric spin up and spin down states around the Fermi level and indicates the magnetic nature of pristine $(10\bar{1}1)$ surface. The inset of Fig. 6.1(b) is the net spin density of pristine semi-polar surface, shows that the magnetic moments are mainly derived from DBs of surface N atoms. These DBs generally prefer to be saturated through passivation or reconstruction to minimize the surface energy. Nevertheless, due to the complex structure of $(10\bar{1}1)$ surface, it is challenging to find all the possible reconstructed configurations, which requires more number atoms and also more computational power especially to study the magnetic coupling. The difficulty in finding the stable reconstructed

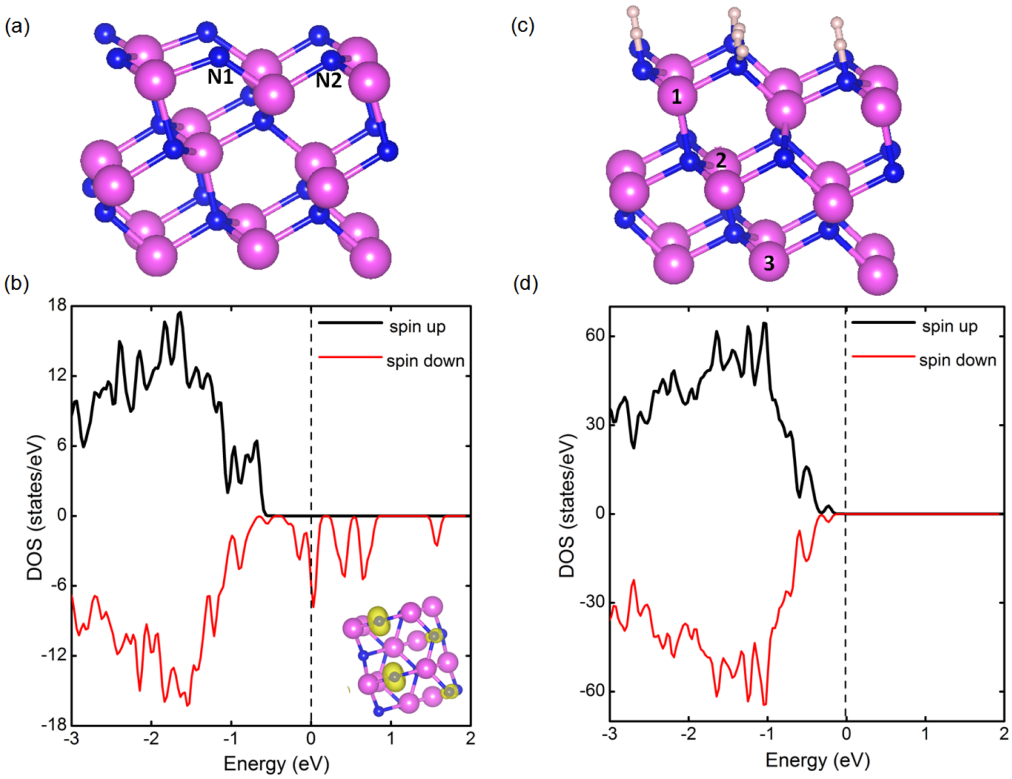

Figure 6.1: Modelling of pristine $(10\bar{1}1)$ surface (a), the corresponding total DOS of pristine $(10\bar{1}1)$ surface (b). N1 and N2 atoms are the different coordinated surface N atoms and inset of (b) is the net spin density plot. Modelling of passivated AlN $(10\bar{1}1)$ surface with different doping locations of Mg represented in numbers (c) and its top view, total DOS of passivated $(10\bar{1}1)$ surface (d).

configurations for the nitride semi-polar surfaces can be estimated from the study of GaN semi-polar surfaces [122]. Therefore, in this chapter, only AlN passivated $(10\bar{1}1)$ surface (p-$(10\bar{1}1)$ surface) has been considered as shown in Fig. 6.1 (c). A charge of 0.75 *es* is used to saturate each DB of surface N atom. Due to the complete saturation of DBs, zero magnetic moment is realized on p-$(10\bar{1}1)$ surface. From the DOS as shown in Fig. 6.1 (d), the symmetric spin up and spin down states indicates a non-magnetic behavior of p-$(10\bar{1}1)$ surface. The unpaired states around the Fermi level of pristine $(10\bar{1}1)$ surface (Fig. 6.1 (b)) are disappeared for the case of p-$(10\bar{1}1)$ surface (Fig. 6.1 (d)). This p-$(10\bar{1}1)$ surface has been considered to examine the electronic and magnetic properties due to doping of Mg_{Al}.

6.3.2 Mg doped passivated AlN $(10\bar{1}1)$ surface

The Mg_{Al} defect has been introduced in a 1×3 supercell of p-$(10\bar{1}1)$ surface at different locations as shown in Fig. 6.1 (c). The numbers 1, 2 and 3 represent the Mg_{Al} doping sites at surface, subsurface and at the bulk like position in a slab respectively. The relative energies at sites 1, 2 and 3 with respect to site 3 are -0.14 eV, -0.2 eV and 0 eV respectively. These energy values indicate that the Mg atom preferred to be doped at the subsurface, similar to the case of Mg doped p-$(000\bar{1})$ surface. The capability of doping Mg_{Al} in p-$(10\bar{1}1)$ surface is estimated from the formation energy and it is found to be 0.24 eV for single defect. The doping of Mg_{Al} introduces a magnetic moment of $\sim$ $0.99\ \mu B$. The imbalance between spin up and spin down states as shown in the total DOS of Mg doped p-$(10\bar{1}1)$ surface (Fig. 6.2 (a)), indicates the magnetic behavior. The magnetic moments are prominently dominated by N atoms (N1, N2, N3) and equally

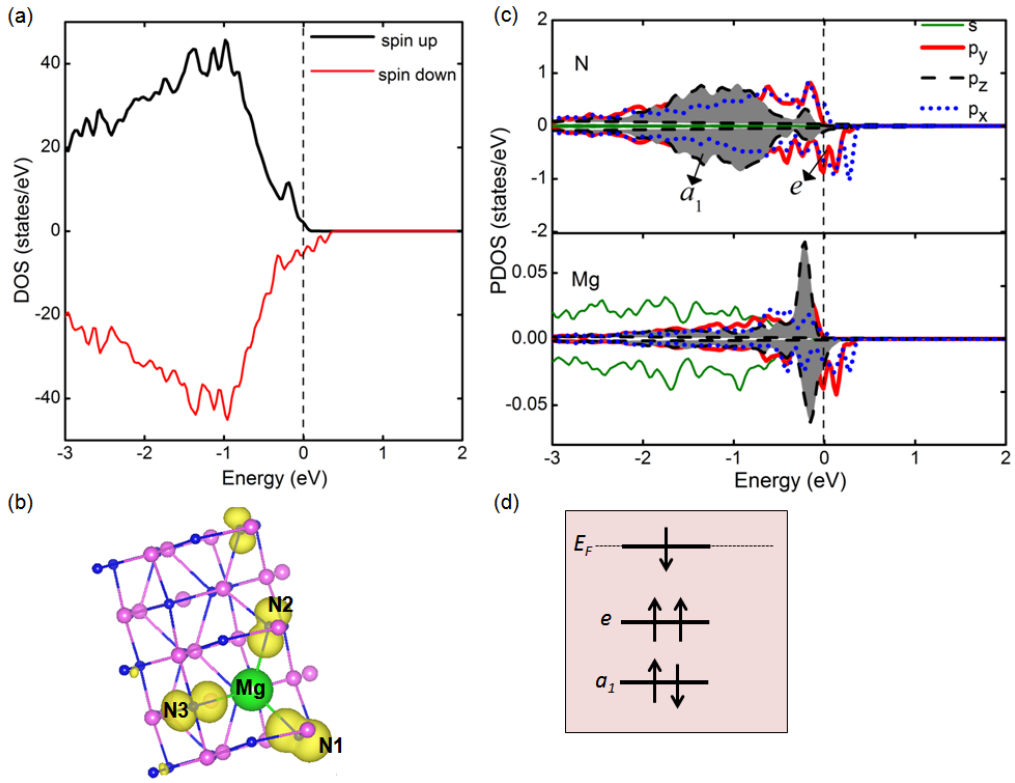

Figure 6.2: Total DOS (a), net spin density plot (b), PDOS of sum of N atoms surrounding Mg and Mg atoms (c), and schematic energy level diagram (d) of Mg doped passivated AlN $(10\bar{1}1)$ surface.

distributed on N atoms surrounding Mg as shown in spin density plot (Fig. 6.2 (b)) similar to that of Mg doped p-$(000\bar{1})$ surface. From PDOS as shown in Fig. 6.2 (c), magnetic moments are mainly derived from *2p* orbitals of N atoms surrounding Mg. The overlap between the peaks of *sp* and *p* orbital of Mg and *p* orbital of N atom around the Fermi level indicates the *sp-p* interaction between Mg and its surrounding N atoms.

The magnetic interaction between two Mg-N clusters is examined by introducing a pair of Mg atoms at a distance of 3.13 Å. Similar to the case of other Mg doped AlN surfaces, FM ground state is observed on Mg doped AlN p-$(10\bar{1}1)$ surface with an energy of 43

meV lower than the energy of AFM state. The magnetic coupling among Mg-N clusters has been analyzed by considering the energy level diagram of Mg doped p-$(10\bar{1}1)$ surface and the hopping interaction between Mg-N clusters on the surface. From PDOS (Fig. 6.2 (c)), it shows that spin up states are completely filled and spin down states are partially filled. Among those states, a_1 state derived from p_z orbital is fully occupied and it has negligible contribution to the magnetic moment. Whereas, the partially filled states around the Fermi level are mainly derived from p_x , p_y orbitals and these orbitals are located at the same energy level. The state derived from p_x, p_y orbitals is considered as doubly degenerate e state. The corresponding schematic energy level diagram of Mg doped p-$(10\bar{1}1)$ surface is shown in Fig. 6.2 (d). Since the high energy level spin down e state is partially filled, there is a possibility of direct virtual charge hopping between spin down e states of Mg-N clusters in FM arrangement as shown in Fig. 6.3 (a). This leads to the more energy gain than that of AFM coupling as shown in Fig. 6.3 (b). In AFM coupling, parallel spin states are at different energy levels and it gives less energy gain than that of FM coupling. As a result, strong FM state has been observed on Mg doped AlN p-$(10\bar{1}1)$ surface. Moreover, the energy difference between FM and AFM states is found to be similar irrespective of any location in a slab that is at the surface, subsurface or at the bulk like position due to the same chemical environment.

The magnetic nature of Mg doped AlN p-$(10\bar{1}1)$ surface is analogous with the magnetic nature of Mg doped AlN p-$(000\bar{1})$ surface. The energy difference between FM and AFM state is always in the range of 40-50 meV in a slab for two Mg atoms at nearest neighbor distance. The long ranged FM nature on Mg doped p-$(10\bar{1}1)$ surface might be possible compared to that of other surfaces due to the more extended nature of defect states on Mg doped AlN p-$(10\bar{1}1)$ surface as shown in spin density plot (Fig. 6.2 (b)). Nevertheless,

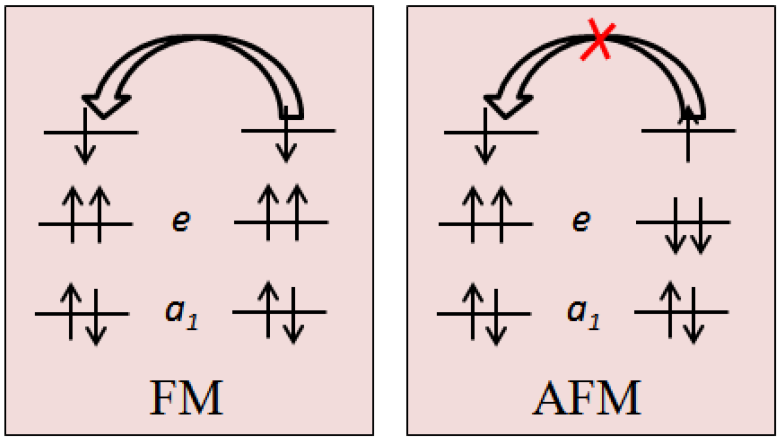

Figure 6.3: Schematic energy level diagrams corresponding to the ferromagnetic coupling (a) and antiferromagnetic coupling (b) between Mg-N clusters in Mg doped passivated AlN $(10\bar{1}1)$ surface.

a very big supercell of Mg doped p-$(10\bar{1}1)$ surface must require to study the long range nature of ferromagnetism, and the computational cost to deal with big supercells is very high. Thus for Mg doped p-$(000\bar{1})$ surface, the magnetic interaction is not considered at large distances of Mg atoms.

6.3.3 Comparison of ferromagnetic stability in various Mg doped AlN surfaces

The formation energies of all Mg doped AlN surfaces are in the range between -1.0 to 0.2 eV, and realized that the doping of Mg on any surface is easier compared to the case of bulk doping (formation energy of bulk doping is 0.37 eV). Interestingly, FM ground state is observed in Mg doped AlN irrespective of any surface orientation, and emphasis

the intrinsic nature of ferromagnetism in Mg doped AlN. However, stability of ferromagnetism changes in different surface orientations. The variation in the FM stability for different surface orientations at different locations of Mg atoms is shown in Fig. 6.4. If we exclude the reconstructed Mg doped $(000\bar{1})$ surface which has completely different surface environment, the strong ferromagnetism is observed in Mg doped $(11\bar{2}0)$ surface and a weak stable FM state is identified in Mg doped $(10\bar{1}0)$ surface. The different stable FM states of various surfaces are further analysed by considering schematic diagrams of DOS of several Mg doped surfaces as shown in Fig. 6.5. The interplay between following three factors have been examined for each surface. (1) exchange splitting between occupied spin up (ε_{up}) and spin down (ε_{dn}) states, (2) energy level splitting between occupied (ε_{dn}) and unoccupied spin down (ε^{0}_{dn}) states, and (3) the band width (w) of occupied spin down state.

The existence of strong localized nature and a narrow band width (w) of partially filled spin down states in Mg doped $(11\bar{2}0)$ surface as shown in Fig. 6.5(a), promote the strong ferromagnetism compared to the case of other surfaces. Whereas, in Mg doped $(10\bar{1}0)$ surface, the splitting between occupied spin up and occupied spin down ($\varepsilon_{up} - \varepsilon_{dn}$) states is almost same as the splitting between occupied spin down and empty spin down ($\varepsilon_{dn} - \varepsilon^{0}_{dn}$) states as shown in Fig. 6.5(b). This introduces a high competition between AFM and FM coupling and thus results in a weak FM stability. On the other hand, partially filled spin down states favor the hopping of same spin electron, and stabilize the strong ferromagnetism in both Mg doped polar p-$(000\bar{1})$ and Mg doped semi-polar p-$(10\bar{1}1)$ surfaces. In case of Mg doped polar p-$(000\bar{1})$ and Mg doped semi-polar p-$(10\bar{1}1)$ surfaces, the band width (w) of partially filled spin down state is wider as shown in Fig. 6.5(c) compared to that of Mg doped $(11\bar{2}0)$ surface (Fig. 6.5(a)). Since, the

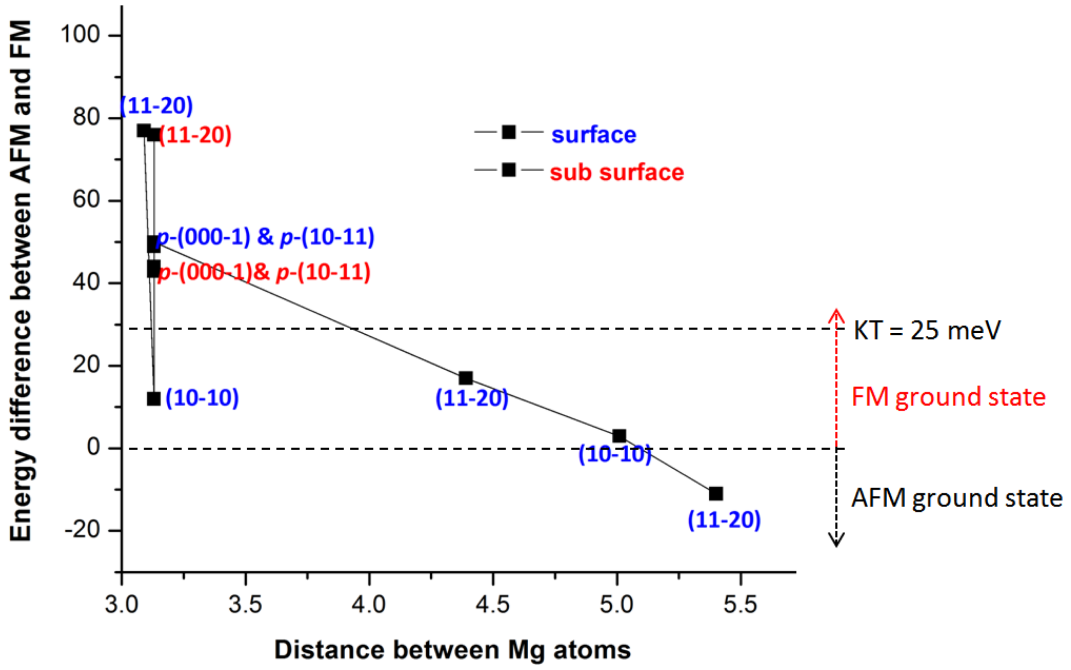

Figure 6.4: The variation in the stability of ferromagnetic state for different surfaces at different distances of Mg atoms. KT is the thermal energy at the room temperature. Positive value of Y-axis indicates the stability of ferromagnetic state.

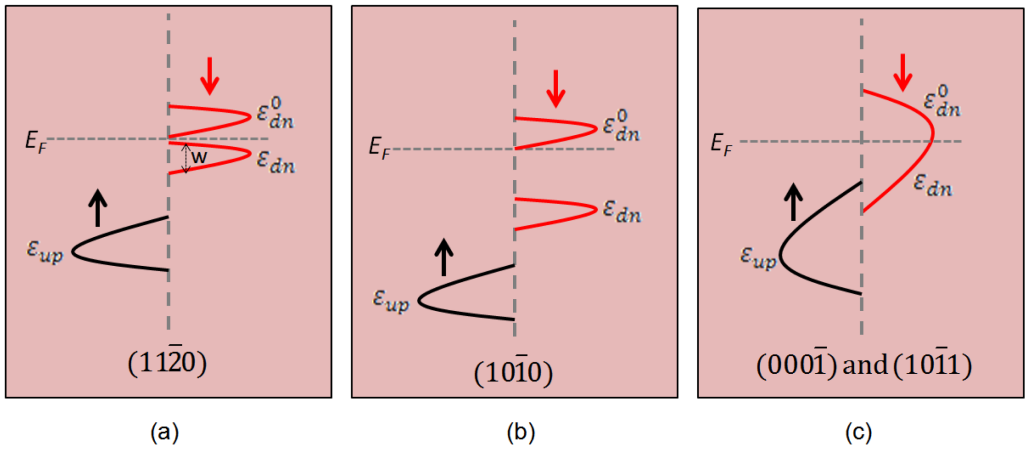

Figure 6.5: Schematic diagrams for DOS of non-polar $(11\bar{2}0)$ surface (a), non-polar $(10\bar{1}0)$ surface (b), and polar p-$(000\bar{1})$ and semi-polar p-$(10\bar{1}1)$ surfaces (c) of Mg doped AlN.

band width is large in Mg doped p-$(000\bar{1})$ and Mg doped p-$(10\bar{1}1)$ surfaces, it allows the possibility of charge hopping between parallel spin states in AFM coupling in addition to the case of FM coupling. In other words, the large band width increases the competition between FM and AFM coupling on Mg doped p-$(000\bar{1})$ and Mg doped p-$(10\bar{1}1)$ surfaces compared to the case of Mg doped $(11\bar{2}0)$ surface. Therefore, even though FM sate is stable with $\triangle E$ of $\sim$ 45 meV on both Mg doped p-$(000\bar{1})$ and Mg doped p-$(10\bar{1}1)$ surfaces, it is less stable than that of Mg doped $(11\bar{2}0)$ surface ($\triangle E$ = 75 meV). These observations indicate that the variation in the surface environment from one surface to other surface results in a different localization of magnetic moments and energy level splitting, which significantly affect the stability of ferromagnetism in different surface orientations of Mg doped AlN.

6.4 Chapter summary

In this chapter, the electronic and magnetic properties of Mg doped AlN semi-polar surface have been extensively studied and compared with that of other Mg doped AlN surfaces. The existence of stable ferromagnetism in Mg doped AlN semi-polar surface supports the intrinsic nature of ferromagnetism in Mg doped AlN. The localization of magnetic moments and energy level splitting favor the ferromagnetic ground state in Mg doped p-$(10\bar{1}1)$ surface, analogous to the case of Mg doped polar surface p-$(000\bar{1})$. The direct charge hopping between partially filled spin down states around the Fermi level stabilizes the strong ferromagnetic ground state. However, the observed ferromagnetism is less stable in Mg doped $(10\bar{1}1)$ surface due to the large band width of partially filled spin down states compared to that of Mg doped $(11\bar{2}0)$ surface. The energy level

splitting, localization of magnetic moments and band width of defect states etc. are significantly influenced by the surface effects in different surface orientations of Mg doped AlN, which result in different stable ferromagnetic states. The sensitivity of stability of ferromagnetism with surface orientation further paves a way to attain a strong ferromagnetism in Mg doped AlN by tuning the surface effects.

Chapter 7

Electronic and magnetic properties of Be and K doped AlN surfaces

7.1 Introduction

The electronic and magnetic properties of Mg doped AlN from bulk to surfaces have been extensively discussed in the previous chapters. The mechanism of ferromagnetism in Mg doped AlN is systematically analyzed based on energy level diagrams and the hopping interaction between defect energy levels. The doping of Mg in AlN (Mg_{Al}) introduces a hole and left the spin down states of 2*p* orbitals of N atoms to be partially filled. The energy level splitting due to doping of Mg_{Al}, stabilizes the ferromagnetism in AlN from bulk to surface. The possibility of direct charge hopping between partially filled spin down states of Mg-N clusters favors FM ground state and showed an intrinsic nature of ferromagnetism in Mg doped AlN. These studies motivated further to explore

the prospect of ferromagnetism in other alkali or alkaline earth metal doped surfaces. In chapter 3, the electronic and magnetic properties have been discussed for the other alkali and alkaline earth metals doped AlN such as Be and K doped bulk AlN. In Be doped AlN, the strong binding between Be and host anions in the valence band, does not allow any gap states and shows a non-magnetic behavior. Whereas, K_{Al} doping in bulk AlN, results in a weak stable FM state. However, since significant changes in the magnetism have been noticed in various systems from bulk to low-dimension [6, 7, 38–40, 42, 43, 46, 47], in this chapter, the electronic and magnetic properties of Be and K doped AlN surfaces have been discussed and compared with that of bulk. The observed mechanism of magnetism in Mg doped AlN is extended to analyze the nature of magnetism of Be and K doped AlN surfaces.

7.2 Computational details

The optimized wurtzite AlN structure with lattice constants a = 3.13 Å and c = 5.014 Å is employed to model the slab of all Be and K doped AlN surfaces. A slab model with a thickness of 10 atomic layers in a 2×2 supercell is considered for a single defect in non-polar $(10\bar{1}0)$, $(11\bar{2}0)$ and polar p-$(000\bar{1})$ surfaces. A 1×3 supercell is considered for semi-polar p-$(10\bar{1}1)$ surface. A Gamma centered $6 \times 6 \times 1$ is employed for non-polar and p-$(000\bar{1})$ surfaces and a $6 \times 4 \times 1$ K-point mesh is used to sample the irreducible Brillouin zone of p-$(10\bar{1}1)$ surface. The electron wave function is expanded using plane waves with a cutoff energy of 500 eV. The magnetic interaction between two Be or two K dopants is analyzed in a 3×3 supercell of AlN non-polar and p-$(000\bar{1})$ surfaces and a 2×3 supercell is chosen for semi-polar p-$(10\bar{1}1)$ surface. In these supercells, the

two Be or two K atoms incorporation correspond to a surface doping coverage of 25%, 22%, 25% and 33% for $(10\bar{1}0)$, $(11\bar{2}0)$, p-$(000\bar{1})$ and p-$(10\bar{1}1)$ surfaces respectively. In addition, a vacuum region of 12 Å is used to minimize the interaction of adjacent surfaces. During relaxation process, atoms in the bottom four layers of all surfaces are fixed, and the positions of other atoms are fully relaxed using the conjugate gradient algorithm [103] until the maximum force on a single atom is less than 0.01 eV/Å. A bulk like behavior is attained at the central layers of a slab. The DBs on top of polar and semi-polar surfaces are saturated by using pseudo hydrogen atoms.

The capability of Be or K doping in the substitution of Al for various AlN surfaces is calculated from the formation energy as shown in Eq. (7.1) [48],

$$E_{Form} = E_{Dope} - E_{Ideal} + n(\mu_{Al} - \mu_X) \tag{7.1}$$

where E_{Dope} and E_{Ideal} are the total energies of doped and undoped surfaces respectively. n is the number of X (Be or K) atoms added, or equivalently the number of Al atoms removed. μ_X and μ_{Al} are the chemical potentials of X and Al atoms respectively. The chemical potential of X is considered from its bulk phase as $\mu_X = \mu_X^{Bulk}$ and chemical potential of Al is calculated from $\mu_{Al} = \mu_{AlN}^{Bulk} - \frac{1}{2}\mu_{N_2}$ [105]. Here μ_{AlN}^{Bulk} is considered as the total energy of bulk AlN per unit cell and μ_{N_2} is the total energy of N_2 molecule.

7.3 Results and discussion

7.3.1 Be doped AlN surfaces

Firstly, the electronic and magnetic properties have been examined for various Be doped AlN surfaces such as non-polar $(10\bar{1}0)$, $(11\bar{2}0)$, polar p-$(000\bar{1})$ and semi-polar p-$(10\bar{1}1)$ surfaces. The doping locations of Be_{Al} in all AlN surfaces are considered similar to that of Mg doped AlN surfaces. For AlN non-polar $(10\bar{1}0)$ and $(11\bar{2}0)$ surfaces, the most favorable location of Be_{Al} is considered at the top layer of the surface and it is at the subsurface in case of polar p-$(000\bar{1})$ and semi-polar p-$(10\bar{1}1)$ surfaces. Interestingly, Be_{Al} introduces the magnetism in AlN non-polar surfaces in contrast from Be doped bulk AlN. The total DOS of Be doped non-polar $(10\bar{1}0)$ and $(11\bar{2}0)$ surfaces are shown in Fig. 7.1(a) and 7.1(b) respectively. The DOS clearly shows a spin imbalance between spin up and spin down states and it results in a magnetic moment of $\sim 1\ \mu B$. The similar nature of magnetism has been realized in C doped SnO2 from its bulk to surface [47]. In bulk SnO2, C doping introduces a non-magnetic state, whereas it shows a magnetic nature on SnO2 surface due to surface effects.

However, unlike the non-polar surfaces of Be doped AlN, magnetism disappears on Be doped polar p-$(000\bar{1})$ and Be doped semi-polar p-$(10\bar{1}1)$ surfaces. This clearly indicates that the magnetism in Be doped AlN non-polar surfaces is the surface effect. The total DOS of Be doped polar surface is shown in Fig. 7.1(c). The symmetric spin up and spin down states exhibit the non-magnetic nature similar to that of Be doped bulk AlN. The magnetic property in Be doped semi-polar p-$(10\bar{1}1)$ surface is found to be same as the magnetic property of Be doped polar p-$(000\bar{1})$ surface. Since in Be doped p-$(000\bar{1})$ and

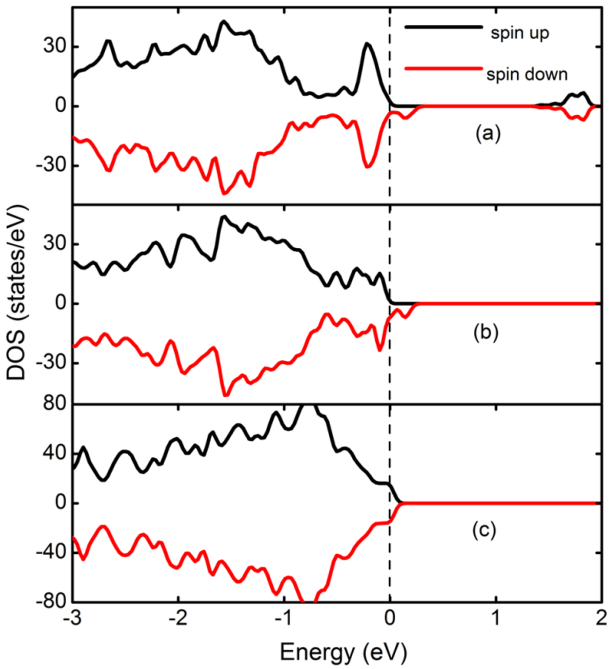

Figure 7.1: Total DOS of $(10\bar{1}0)$ (a), $(11\bar{2}0)$ (b), and p-$(000\bar{1})$ (c) surfaces of Be doped AlN

Be doped p-$(10\bar{1}1)$ surfaces, the surface effects are screened by pseudo hydrogen atoms, and the interaction between Be and surrounding N atoms on the subsurface is found to be similar to that of Be doped bulk AlN. The bond length between Be and its nearest N atom in Be doped bulk AlN is 1.83 Å. At the subsurface location of Be doped p-$(000\bar{1})$ and Be doped p-$(10\bar{1}1)$ slabs, the bond length between Be to nearest N atom is only changed by $\sim 2.2\%$ compared to that of bulk, and remains in a non-magnetic state similar to the case of Be doped bulk AlN. Nevertheless, the doping of Be in non-polar surfaces, allows the large structural relaxation on the surface, and the bond length between Be-N atoms is changed by $\sim 9\%$ compared to that of bulk. The weak interaction of Be with its surrounding surface N atoms, allows the gap states around the Fermi-level in Be doped non-polar surfaces. Due to the existence of lower coordination and the large structural relaxation at the surface, Be_{Al} defect invokes the magnetism in AlN non-polar surfaces. The doping of Be_{Al} in AlN non-polar surfaces, results in a magnetic moment of $\sim 1\ \mu B$ similar to the case of Mg doped AlN non-polar surfaces. The magnetic moments of Be doped $(10\bar{1}0)$ and Be doped $(11\bar{2}0)$ surfaces are mainly localized on surface N atoms near Be (Be-N cluster) as shown in Fig. 7.2(a) and 7.2(c) respectively. The partial DOS of both Be doped $(10\bar{1}0)$ and Be doped $(11\bar{2}0)$ surfaces are shown in Fig. 7.2(b) and Fig. 7.2(d) respectively. The magnetic moments are mainly derived from 2*p* orbitals of N atoms, and the negligible contribution arises from Be atom. Similar to the *sp-p* interaction between Mg and N atoms, the overlap between the peaks of *s* and *p* orbitals of Be and *p* orbital of N atoms shows an existence of *sp-p* interaction in Be doped AlN surface.

The magnetic coupling between Be-N clusters has been analyzed by introducing a pair of Be atoms at a distance of 3.13 Å for both Be doped $(10\bar{1}0)$ and Be doped $(11\bar{2}0)$

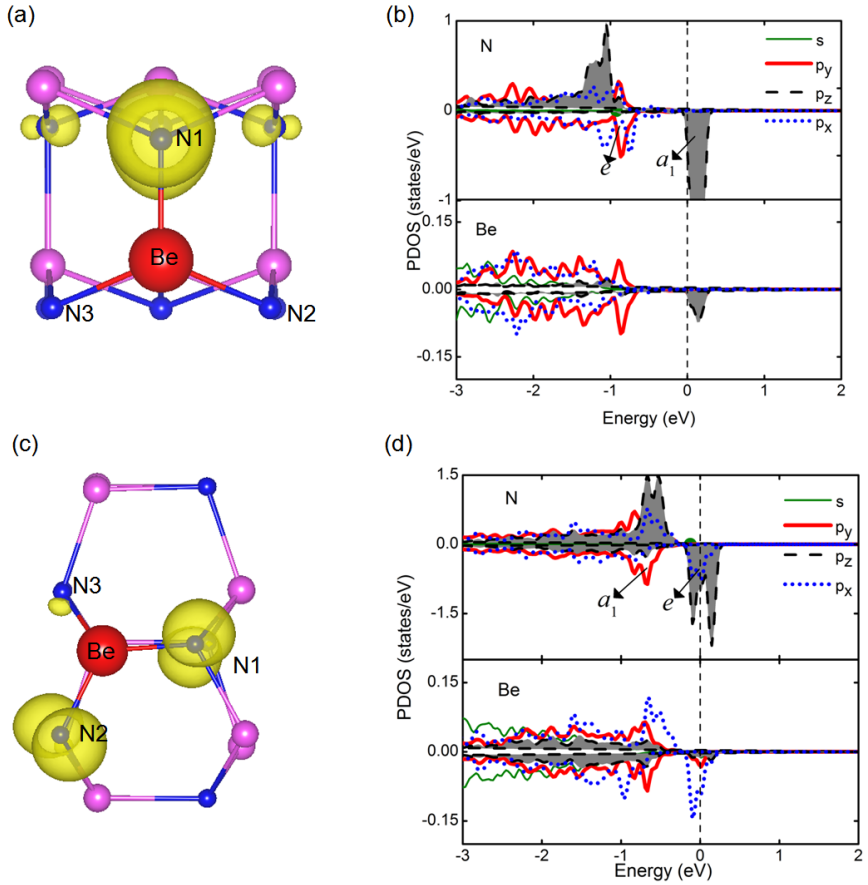

Figure 7.2: Net spin density (a) and PDOS of Be and N atoms (b) of Be doped $(10\bar{1}0)$ surface, net spin density (c) and PDOS of Be and N atoms (d) of Be doped $(11\bar{2}0)$ surface.

surfaces. The energy differences between FM and AFM states for both Be doped $(10\bar{1}0)$ and Be doped $(11\bar{2}0)$ surfaces are found to be 14 meV and 140 meV respectively. The magnetic interaction between Be-N clusters is analyzed based on energy level splitting and the hopping mechanism similar to the case of Mg doped AlN. In the PDOS of Be doped $(10\bar{1}0)$ surface as shown in Fig. 7.2(b), p_x and p_y orbitals are filled and the corresponding state is considered as doubly degenerate e state. While, singly occupied a_1 state derived from p_z orbital is partially filled. Whereas, in case of Be doped $(11\bar{2}0)$ surface, p_y orbital is filled and other two orbitals p_x, p_z are partially filled and degenerate. The a_1 state derived from p_y orbital is at the lower energy level than doubly degenerate e state derived from p_x and p_z orbitals as shown in Fig. 7.2(d). Since spin down a_1 state is empty in case of Be doped $(10\bar{1}0)$ surface, weak stable FM state is observed due to the only possibility of indirect charge hopping between spin down e and a_1 states. The strong localized nature of spin down a_1 state and the large splitting between spin down a_1 and spin down e states, weaken the hopping interaction between defect states. This exchange splitting results in a weak stable FM state in Be doped $(10\bar{1}0)$ surface. Nevertheless, in Be doped $(11\bar{2}0)$ surface, the existence of partially filled spin down e states allows the direct charge hopping between Be-N clusters and highly stabilizes the FM state.

The localized nature of magnetic moments and the energy level splitting of Be-N clusters vary from one surface to other surface, and consequences different stable FM states on Be doped $(10\bar{1}0)$ and Be doped $(11\bar{2}0)$ surfaces. Since in Be doped AlN, stability of ferromagnetism is sensitive with the surface effects, it might be possible to attain ferromagnetism at low-dimension by tuning the surface effects. Moreover, from the Eq. (7.1), the calculated formation energies of Be doped $(10\bar{1}0)$ and Be doped $(11\bar{2}0)$

surfaces are found to be -3.62 eV and -3.18 eV respectively. These formation energies indicate the possibility of more Be doping concentration to attain a strong FM state. However, since magnetism is not an intrinsic property of Be doped AlN and it varies from one surface to other surface, specific crystal surface orientation should be required to attain ferromagnetism in Be doped AlN at the low-dimension.

7.3.2 K doped AlN surfaces

The alkali metal K is introduced in the substitution of Al at different surface orientations of AlN similar to the case of Be and Mg doped AlN. The doping of K_{Al} in AlN results in a magnetic moment of $\sim 2\ \mu B$ for all surfaces due to the two holes created by K_{Al} defect. The total DOS of K doped $(10\bar{1}0)$, $(11\bar{2}0)$ and p-$(000\bar{1})$ surfaces are shown in Fig. 7.3 (a), 7.3 (b) and 7.3 (c) respectively. The spin imbalance between spin up and spin down states around the Fermi level indicates the magnetic nature of all K doped surfaces. Magnetic moments are prominently derived from N atoms (K-N cluster), but the localization of magnetic moments varies form one surface to other surface as shown in right side of Fig. 7.3. Similar to Mg doped AlN surfaces, magnetic moments of both K doped $(10\bar{1}0)$ and K doped $(11\bar{2}0)$ surfaces are unequally distributed and strongly localized on surface N atoms. In case of K doped polar p-$(000\bar{1})$ surface, magnetic moments are equally distributed on N atoms surrounding K. The magnetic property of K doped p-$(10\bar{1}1)$ surface is found to be similar with the magnetic property of K doped p-$(000\bar{1})$ surface. The PDOS of spin polarized N atoms of each surface are shown in Fig. 7.4. In case of K doped $(10\bar{1}0)$ surface (Fig. 7.4(a)), the existence of partially filled states near the Fermi level allow the direct charge hopping between the K-N clusters,

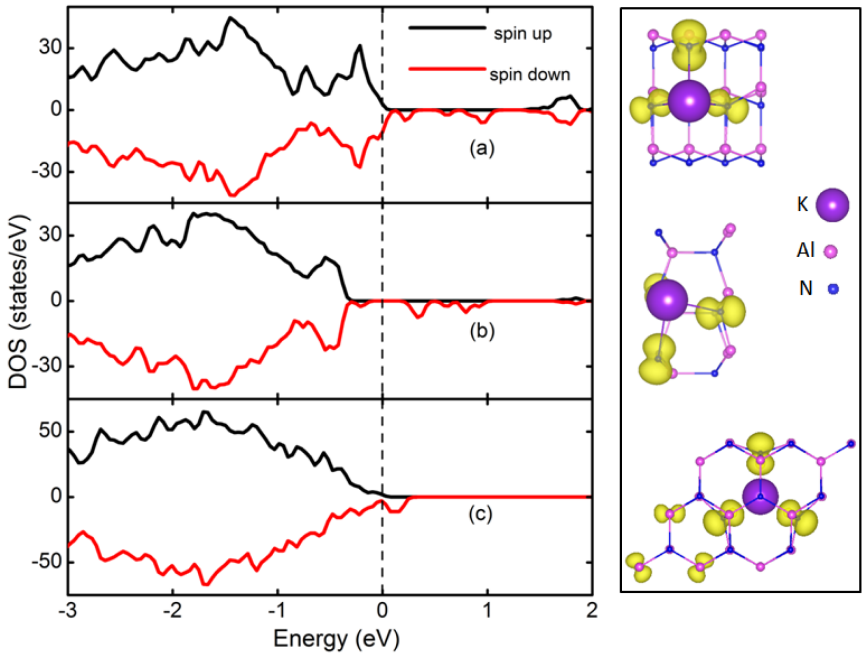

Figure 7.3: Total DOS of $(10\bar{1}0)$ (a), total DOS of $(11\bar{2}0)$ (b), and total DOS of p-$(000\bar{1})$ (c) surfaces of K doped AlN, and their corresponding spin density plots are shown at the right side.

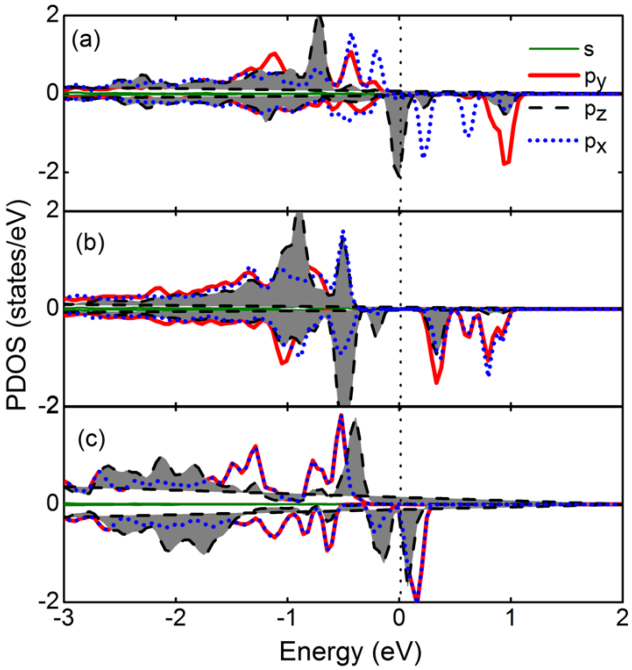

Figure 7.4: PDOS of K and N atoms for $(10\bar{1}0)$ (a), $(11\bar{2}0)$ (b), and p-$(000\bar{1})$ (c) surfaces of K doped AlN.

and stabilizes the FM state with an energy difference of 149 meV. Similarly, the non-polar K doped $(11\bar{2}0)$ and the polar K doped p-$(000\bar{1})$ surfaces exhibit the strong FM state due to the existence of partially filled spin down states around the Fermi level as shown in Fig. 7.4(b) and Fig. 7.4(c) respectively. The energy difference between FM and AFM states for both K doped $(11\bar{2}0)$ and K doped p-$(000\bar{1})$ surfaces are 414 meV and 417 meV respectively. Similar to the polar and semi-polar surfaces of Be and Mg doped AlN, the magnetic nature of K doped semi-polar p-$(10\bar{1}1)$ surface is found to be same as the magnetic nature of K doped polar p-$(000\bar{1})$ surface. The strong FM state is observed on K doped AlN surfaces compared to the case of Be and Mg doped AlN surfaces due to the more number of holes introduced by K_{Al} defect. Nevertheless, the formation energies of K doped AlN $(10\bar{1}0)$, $(11\bar{2}0)$, p-$(000\bar{1})$ and p-$(10\bar{1}1)$ surfaces are found to be 1.3 eV, 1.3 eV, 5.85 eV and 5.96 eV respectively. These formation energy values are high and thus AlN may not allow high K doping concentration to attain strong ferromagnetism.

7.4 Chapter summary

The magnetic phenomenon observed in Mg doped AlN is successfully extended to understand the nature of magnetism in other alkali and alkaline earth metals doped AlN. The variation in the surface environment from one surface to other surface significantly changes the magnetic nature. Magnetism is obtained on Be doped non-polar surfaces, and the non-magnetic behavior is noticed in Be doped passivated polar and semi-polar surfaces. The nature of localization of magnetic moments in Be doped AlN non-polar surfaces is found to be same as that of Mg doped AlN non-polar surfaces. Similarly,

the electronic and magnetic properties have been investigated for the case of K-doped AlN surfaces. The more number of holes introduced by K_{Al} allows the strong ferromagnetic state on K doped $(10\bar{1}0)$ surface, compared to the case of Be or Mg doped $(10\bar{1}0)$ surfaces. The existence of partially filled degenerate states stabilizes the ferromagnetic state on K doped AlN surfaces. Nevertheless, the high doping concentration of K is hard to achieve in AlN due to the high formation energies, and thus it is difficult to attain strong ferromagnetism in K doped AlN for practical applications. Since the proposed mechanism of magnetism in Mg doped AlN has been successfully extended to understand the magnetic property of Be and K doped AlN systems from bulk to low-dimension, I strongly believe that the same magnetic phenomenon can be applicable to understand the nature of magnetism for the other non-magnetic elements doped nitride based semiconductors.

Chapter 8

Conclusion remarks

In this thesis, an extensive study has been carried out to reveal the nature of magnetism and understand the influence of surface effects on the magnetism of non-magnetic element doped semiconductors using first-principles calculations. I have considered AlN as a prototype material and analyzed the electronic and magnetic properties of various non-magnetic alkali and alkaline earth metals doped AlN. The focus of my investigation is to unveil the origin and nature of ferromagnetism in Mg doped AlN, which was observed experimentally in normal and zigzag nanowires. Since at the low-dimension, the electronic and magnetic properties can be strongly affected by the surface effects, the influence of surface effects on the magnetism of Mg doped AlN is thoroughly scrutinized by considering different Mg doped AlN surfaces such as non-polar, polar and semi-polar surfaces. The origin and mechanism of ferromagnetism have been analyzed in Mg doped AlN from bulk to different surfaces. The similar magnetic phenomenon has been extended to understand the nature of magnetism of other alkali and alkaline

earth metals doped AlN surfaces.

Firstly, the electronic and magnetic properties have been examined in the bulk AlN by doping Mg, K and Be atoms. In Mg or K doped AlN, magnetic moments are prominently derived from N atoms surrounding the dopant. The $2p$ orbitals of N atoms in Mg-N or K-N clusters are partially filled due to the holes introduced by dopants. The direct charge hopping between degenerate partially filled spin down states of Mg-N clusters favors strong ferromagnetic ground state in Mg doped AlN. Nevertheless, the indirect charge hopping between partially filled spin down states results in a weak stable ferromagnetic state in K doped AlN. Unlike Mg doped AlN or K doped AlN, since Be has smaller ionic radius and same electronegativity as of Al, the doping of Be in bulk AlN does not allow any gap states around the Fermi level and results in a non-magnetic state.

Secondly, the influence of surface effects on the electronic and magnetic properties of Mg doped AlN has been discussed by considering different surfaces such as non-polar, polar and semi-polar surfaces. Ferromagnetic ground state is identified in Mg doped AlN irrespective of any surface orientation. The possibility of direct charge hopping between degenerate partially filled spin down states of Mg-N clusters, stabilized the ferromagnetic ground state in Mg doped AlN surfaces. However, the stability of ferromagnetism is changed for different surfaces due to various surface effects. The interplay among the localization of magnetic moments, energy level splitting and *sp-p* interaction between Mg-N clusters, vary from one surface to other surface and leads to the different stable ferromagnetic states. The weak stable ferromagnetic state is obtained on Mg doped non-polar $(10\bar{1}0)$ surface and the strong ferromagnetic state is realized on non-polar $(11\bar{2}0)$ surface, passivated and reconstructed polar $(000\bar{1})$ surfaces, and semi-polar $(10\bar{1}1)$ surface of Mg doped AlN.

The scenario behind the different stable ferromagnetic states has been analyzed systematically. The magnetic interaction between Mg-N clusters is found to be sensitive with structural relaxation. The spin density around the overlap region between Mg-N clusters varies with the structural relaxation, and results in different stable ferromagnetic states on Mg doped $(10\bar{1}0)$ surface before and after relaxation. The increase in the bond length between Mg-N clusters upon relaxation, weakens the interaction between Mg-N clusters and results in a weak stable ferromagnetic state on Mg doped non-polar $(10\bar{1}0)$ surface. In Mg doped $(11\bar{2}0)$ surface, strong ferromagnetic state is observed due to the possibility of strong interaction between Mg-N clusters through surface N atoms of high spin density. Moreover, the large splitting is noticed between occupied and unoccupied spin down states in the case of Mg doped $(10\bar{1}0)$ surface, and it weakens the hopping interaction in ferromagnetic coupling. Whereas, the negligible splitting between occupied and unoccupied spin down states favors the strong ferromagnetic ground state on Mg doped $(11\bar{2}0)$ surface. Similarly, for polar and semi-polar Mg doped AlN surfaces, the direct charge hopping between partially occupied spin down states favors the strong ferromagnetism. The observation of ferromagnetism in Mg doped AlN surfaces further supports the recent experimental studies on Mg doped AlN.

Finally, the proposed mechanism of magnetism in Mg doped AlN has been further extended to analyze the nature of magnetism in other alkali and alkaline earth metals AlN doped surfaces. In contrast to Be doped bulk AlN, the magnetic order has been realized on Be doped AlN non-polar surfaces. Similar to non-polar surfaces of Mg doped AlN, weak ferromagnetic state is observed on Be doped non-polar $(10\bar{1}0)$ surface, and the strong ferromagnetism is noticed in Be doped non-polar $(11\bar{2}0)$ surface. However, the polar and semi-polar surfaces of Be doped AlN exhibit a non-magnetic nature similar to

that of Be doped bulk AlN. In K doped AlN surfaces, the partially filled spin down states favor the strong ferromagnetic ground state in all surface orientations. Nevertheless, the formation energies of doping K in AlN are found to be high in bulk as well as at the surface.

The present study of surface magnetism of Mg, Be and K doped AlN systems led us to acquire the knowledge of nature of magnetism in non-magnetic element doped semiconductors due to various surface effects. Among Be, K and Mg dopants; Mg doping introduces the strong localized nature of defect states, and the existence of partially filled degenerate states at the high energy level stabilized the ferromagnetism from bulk to surface of Mg doped AlN. The present study and the recent experimental observations of room temperature ferromagnetism in Mg doped AlN strongly encourage the further directions of Mg doped AlN for the possible spintronic applications. Moreover, since the stability of ferromagnetism in Mg doped AlN is sensitive with the surface effect, it could be possible to get high stable ferromagnetism by tuning the surface effects. One of such studies is identified in the case of Mg doped AlN reconstructed $(000\bar{1})$ surface, which exhibits a stable and long ranged ferromagnetism.

Although an extensive study has been done to understand and identify the origin of magnetism in non-magnetic element doped semiconductors, still there is a lot more space remains to be filled for better spintronic applications in the future. Especially, since DFT is a ground state theory, I did not study the temperature effects, phase transition etc., and those will need to be cleared in the future. Since the present study supports the ferromagnetism in Mg doped AlN, we need to have considerable attention especially in the experimental direction to enhance its applications for opto-magnetic applications. Furthermore, the stability of ferromagnetism on each surface orientation of Mg doped

AlN indicates the possibility of forming magnetic Mg doped AlN superlattices for the potential spintronic applications.

References

[1] I. Žutić, J. Fabian and S. Das Sarma, Rev. Mod. Phys. **76**, 323 (2004).

[2] H. Ohno, A. Shen, F. Matsukura, A. Oiwa, A. Endo, S. Katsumoto, and Y. Iye, Appl. Phys. Lett. **69**, 363 (1996).

[3] D. Chiba, K. Matsukura, and H. Ohno, Appl. Phys. Lett. **82**, 3020 (2003).

[4] K. W. Edmonds, K. Y. Wang, R. P. Campion, A. C. Neumann, N. R. S. Rarley, B. L. Gallagher, and C. T. Foxon, Appl. Phys. Lett. **82**, 4991 (2002).

[5] T. Dietl, H. Ohno, F. Matsukura, J. Cibert, and D. Ferrand, Science **287**, 1019 (2000).

[6] M. L. Reed, N. A. El-Masry, H. H. Stadelmaier, M. K. Ritums, M. J. Reed, C. A. Parker, J. C. Roberts, S. M. Bedair, Appl. Phys. Lett. **79**, 3473 (2001).

[7] Q. Wang, Q. Sun, and P. Jena, Phys. Rev. Lett. **95**, 167202 (2005).

[8] P. Sharma, A. Gupta, K. V. Rao, F. J. Owens, R. Sharma, R. Ahuja, J. M. O. Guillen, B. Johansson and G. A. Gehring, Nat. Mater. **2**, 673 (2003).

[9] Y. Matsumoto, M. Murakami, T. Shono, T. Hasegawa, T. Fukumura, M. Kawasaki, P. Ahmet, T. Chikyow, S. Koshihara, and H. Koinuma, Science **291**, 854 (2001).

[10] M. Hashimoto, Y. -K. Zhou, M. Kanakura and H. Asahi, Solid State Commun. **122**, 37 (2002).

[11] J. S. Lee, J. D. Lim, Z. G. Khim, Y. D. Park, S. J. Pearton, S. N. G. Chu, J. Appl. Phys. **93**, 4512 (2003).

[12] C. Liu, F. Yun and H. Morkoç, J. mat. science : Materials in electronics **16**, 555 (2005).

[13] J. Philip, A. Punnoose, B. I. Kim, K. M. Reddy, S. Layne, J. O. Holmes, B. Satpati, P. R. LeClair, T. S. Santos and J. S. Moodera, Nat. Mater. **5**, 298 (2006).

[14] S. Kuroda, N. Nishizawa, K. Takita, M. Mitome, Y. Bando, K. Osuch and T. Dietl, Nat. Mater. **6**, 440 (2007).

[15] C. N. R. Rao and F. L. Deepak, J. Mater. Chem. **15**, 573 (2005).

[16] X. Y. Cui, J. E. Medvedeva, B. Delley, A. J. Freeman, N. Newman and C. Stampfl, Phys. Rev. Lett. **95**, 256404 (2005).

[17] X. Y. Cui, J. E. Medvedeva, B. Delley, A. J. Freeman, and C. Stampfl, Phys. Rev. B **75**, 155205 (2007).

[18] K. Ueda, H. Tabata, and T. Kawai, Appl. Phys. Lett. **79**, 988 (2001).

[19] L. -H. Ye, A. J. Freeman, and B. Delley, Phys. Rev. B **73**, 033203 (2006).

[20] D. L. Hou, X. J. Ye, H. J. Meng, H. J. Zhou, X. L. Li, C. M. Zhen, and G. D. Tang, Appl. Phys. Lett. **90**, 142502 (2007).

[21] R. Q. Wu, G. W. Peng, L. Liu, Y. P. Feng, Z. G. Huang, and Q. Y. Wu, Appl. Phys. Lett. **89**, 062505 (2006).

[22] J. H. Lee, I. H. Choi, S. Shin, S. Lee, J. Lee, C. Whang, S. C. Lee, K. R. Lee, J. H. Baek, K. H. Chae, and J. Song, Appl. Phys. Lett. **90**, 032504 (2007).

[23] D. B. Buchholz, R. P. H. Chang, J. H. Song, and J. B. Ketterson, Appl. Phys. Lett. **87**, 082504 (2005).

[24] H. -K. Seong, J. -Y. Kim, J. -J. Kim, S. -C. Lim, S. -R. Kim, U. Kim, T. -E. Park, and H. -J. Choi, Nano. Lett. **7**, 3366 (2007).

[25] H. Pan, J. B. Yi, L. Shen, R. Q. Wu, J. H. Yang, J. Y. Lin, Y. P. Feng, J. Ding, L. H. Van, and J. H. Yin, Phys. Rev. Lett. **99**, 127201 (2007).

[26] C. -F. Yu, T. -J. Lin, S. -J. Sun, and H. Chou, J. Phys. D **40**, 6497 (2007).

[27] L. Shen, R. Q. Wu, H. Pan, G. W. Peng, M. Yang, Z. D. Sha, and Y. P. Feng, Phys. Rev. B **78**, 073306 (2008).

[28] I. S. Elfimov, A. Rusydi, S. I. Csiszar, Z. Hu, H. H. Hsieh, H. -J. Lin, C. T. Chen, R. Liang, and G. A. Sawatzky, Phys. Rev. Lett. **98**, 137202 (2007).

[29] K. Yang, Y. Dai, B. Huang and M. -H. Whangbo, Appl. Phys. Lett. **93**, 132507 (2008).

[30] J. B. Yi, C. C. Lim, G. Z. Xing, H. M. Fan, L. H. Van, S. L. Huang, K. S. Yang, X. L. Huang, X. B. Qin, B. Y. Wang, T. Wu, L. Wang, H. T. Zhang, X. Y. Gao, T. Liu, A. T. S. Wee, Y. P. Feng, and J. Ding, Phys. Rev. Lett. **104**, 137201 (2010).

[31] M. Venkatesan, C. B. Fitzgerald, and J. M. D. Coey, Nature (London) **430**, 630 (2004).

[32] N. H. Hong, N. Poirot, and J. Sakai, Phys. Rev. B **77**, 033205 (2008).

[33] C. Madhu, A. Sundaresan, and C. N. R. Rao, Phys. Rev. B **77**, 201306R (2008).

[34] M. Khalid, M. Ziese, A. Setzer, P. Esquinazi, M. Lorenz, H. Hochmuth, M. Grundmann, D. Spemann, T. Butz, G. Brauer, W. Anwand, G. Fischer, W. A. Adeagbo, W. Hergert, and A. Ernst, Phys. Rev. B **80**, 035331 (2009).

[35] B. Song, J. C. Han, J. K. Jian, H. Li, Y. C. Wang, H. Q. Bao, W. Y. Wang, H. B. Zuo, X. H. Zhang, S. H. Meng, and X. L. Chen, Phys. Rev. B **80**, 153203 (2009).

[36] S. Dhar, O. Brandt, A. Trampert, K. J. Friedland, Y. J. Sun, and K. H. Ploog, Phys. Rev. B **67**, 165205 (2003).

[37] K.Sato and H. K. -Yoshida, Jpn. J. Appl. Phys. **39**, L555 (2000).

[38] Q. Wang, Q. Sun, P. Jena, and Y. Kawazoe, Phys. Rev. Lett. **93**, 155501 (2004).

[39] N. Sanchez, S. Gallego, and M. C. Munoz, Phys. Rev. Lett. **101**, 067206 (2008).

[40] X. Chen, D. Huang, W. -J. Deng, Y. -J. Zhao, Phys. Lett. A **373**, 391 (2009).

[41] R. Hanafin, T. Archer, and S. Sanvito, Phys. Rev. B **81**, 054441 (2010).

[42] E. Liu, N. Zhao, J. Li, X. Du, and C. Shi, J. Phys. Chem. **115**, 3368 (2011).

[43] G. Huang, and J. Wang, J. Appl. Phys. **111**, 043907 (2012).

[44] X. G. Zhao, Z. Tang, and W. X. Hu, Surf. Sci. **608**, 97 (2013).

[45] M. Zając, J. Gosk, M. Kamińska, A. Twardowski, T. Szyszko, and S. Podsiadło, Appl. Phys. Lett. **79**, 2432 (2001).

[46] Q. Wang, Q. Sun, P. Jena, and Y. Kawazoe, Appl. Phys. Lett. **87**, 162509 (2005).

[47] G. Rahman and V. M. García-Suárez, Appl. Phys. Lett. **96**, 052508 (2010).

[48] H. J. Xiang and S. H. Wei, Nano Lett. **8**, 1825 (2008).

[49] P. Dev, H. Zeng, and P. Zhang, Phys. Rev. B **82**, 165319 (2010).

[50] R. González-Hernández, A. González-Garcia, and W. López-Pérez, Comput. Mater. Sci. **83**, 217 (2014).

[51] C. Zener, Phys. Rev. **81**, 4 (1951).

[52] P. W. Anderson, Phys. Rev. **79**, 350 (1950).

[53] M. A. Ruderman and C. Kittel, Phys. Rev. **96**, 99 (1954).

[54] C. Zener, Phys. Rev. **82**, 403 (1951).

[55] P. Kacman, Semicond. Sci. Technol. **16**, 4 (2001).

[56] P. Dev, Y. Xue, and P. Zhang, Phys. Rev. Lett. **100**, 117204 (2008).

[57] P. Dev, and P. Zhang, Phys. Rev. B **81**, 085207 (2010).

[58] I. Slipukhina, Ph. Mavropoulos, S. Blügel, and M. Ležaić, Phys. Rev. Lett. **107**, 137203 (2011).

[59] G. M. Dalpian, S. -H. Wei, X. G. Gong, Antônio J. R. da Silva and A. Fazzio, Solid State Comm. **138**, 353 (2006).

[60] I. S. Elfimov, S. Yunoki, and G. A. Sawatzky, Phys. Rev. Lett. **89**, 216403 (2002).

[61] B. Gu, N. Bulut, T. Ziman, and S. Maekawa, Phys. Rev. B **79**, 024407 (2009).

[62] R. Q. Wu, G. W. Peng, L. Liu, Y. P. Feng, Z. G. Huang and Q. Y. Wu, Appl. Phys. Lett. **89**, 142501 (2006).

[63] D. Mishra, B. P. Mandal, R. Mukherjee, R. Naik, G. Lawes and B. Nadgorny, Appl. Phys. Lett. **102**, 182404 (2013).

[64] A. J. Fischer, A. A. Allerman, M. H. Crawford, K. H. A. Bogart, S. R. Lee, R. J. Kaplar, W. W. Chow, S. R. Kurtz, K. W. Fullmer and J. J. Figiel, Appl. Phys. Lett. **84**, 3394 (2004).

[65] S. Rajan, P. Waltereit, C. Poblenz, S. J. Heikman, D. S. Green, J. S. Speck, and U. K. Mishra, IEEE Electron Device Lett. **25**, 247 (2004).

[66] Y. Taniyasu, M. Kasu and T. Makimoto, Nature **441**, 325 (2006).

[67] M. L. Nakarmi, N. Nepal, C. Ugolini, T. M. Altahtamouni, J. Y. Lin, Appl. Phys. Lett. **89**, 152120 (2006).

[68] G. Callsen, M. R. Wagner, T. Kure, J. S. Reparaz, M. Bugler, J. Brunnmeier, C. Nenstiel, A. Hoffmann, M. Hoffmann, J. Tweedie, Z. Bryan, S. Aygun, R. Kriste, R. Collazo, Z.Sitar, Phys. Rev. B **86**, 075207 (2012).

[69] R. E. Jones, K. M. Yu, S. X. Li, W. Walukiewicz, J. W. Ager, E. E. Haller, H. Lu and W. J. Schaff, Phys. Rev. Lett. **96**, 125505 (2006).

[70] Y. Y. Hui, J. Ye, R. Lortz, K. S. Teng, and S. P. Lau, Phys. Status Solidi A **209**, 1998 (2012).

[71] Y. Xu, B. Yao, D. Liu, W. Lei, P. Zhu, Q. Cui, and G. Zou, Cryst. Eng. comm. **15**, 3271 (2013).

[72] J. Xiong, P. Guo, F. Guo, X. Sun, and H. Gu, Mat. Lett. **117**, 276 (2014).

[73] G. Kresse and J. Hafner, Phys. Rev. B **49**, 14251 (1994).

[74] M. Born and J. R. Oppenhermer, Ann. Physik **84**, 457 (1927).

[75] P. Hohenberg and W. Kohn, Phys. Rev. B **136**, 864 (1964).

[76] W. Kohn and L. Sham, Phys. Rev. **140**, A1133 (1965).

[77] I. Robertson, M. Payne, and V. Heine, J. Phys. -Condes. Matter **3**, 8351 (1991).

[78] J. P. Perdew and Y. Wang, Phys. Rev. B **45**, 13244 (1992).

[79] J. Perdew, J. Chevary, S. Vosko, K. Jackson, M. Pederson, D. Singh, and C. Fiolhais, Phys. Rev. B **46**, 6671 (1992).

[80] J. P. Perdew, K. Burke and M. Ernzerhof, Phys. Rev. Lett. **77**, 3865 (1996).

[81] D. J. Chadi and M. L. Cohen, Phys. Rev. B **8**, 5747 (1973).

[82] H. J. Monkhorst and J. D. Pack, Phys. Rev. B **13**, 5188 (1976).

[83] J. C. Phillips, Phys. Rev. **112**, 685 (1958).

[84] M. L. Cohen and V. Heine, Solid State Phys. **24**, 37 (1970).

[85] M. T. Yin and M. L. Cohen, Phys. Rev. B **25**, 7403 (1982).

[86] D. J. Singh, L. Nordstrom, "Planes, Pseudopotentials, and the LAPW methd", Springer (2006).

[87] G. B. Bachelet, D. R. Hamann and M. Schluter, Phys. Rev. B **26**, 4199 (1982).

[88] D. Vanderbilt, Phys, Rev. B **41**, 7892 (1990).

[89] P. E. Blöchl, Phys. Rev. B **50**, 17953 (1994).

[90] M. P. Teter, M. C. Payne, and D. C. Allan, Phys. Rev. B **40**, 1225 (1989).

[91] H. X. Liu, S. Y. Wu, R. K. Singh, L. Gu, D. J. Smith, N. Newman, N. R. Dilley, L. Montes, and M. B. Simmonds, Appl. Phys. Lett. **85**, 4076 (2004).

[92] D. Kumar, J. Antifakos, M. G. Blamire, and Z. H. Baber, Appl. Phys. Lett. **84**, 5004 (2004).

[93] L. -J. Shi, L. -F. Zhu, Y. -H. Zhao, and B. -G. Liu, Phy. Rev. B **78**, 195206 (2008).

[94] W. Jia, P. Han, M. Chi, S. Dang, B. Xu, and X. Liu, J. Appl. Phys. **101**, 113918 (2007).

[95] Y. Zhang, W. Liu, P. Liang, H. Niu, Solid State Comm. **147**, 254 (2008).

[96] F. -Y. Ran, M. Subramanian, M. Tanemura, Y. Hayashi and T. Hihara, Appl. Phys. Lett. **95**, 112111 (2009).

[97] K. Li, X. Du, Y. Yan, H. Wang, Q. Zhan, and H. Jin, Phys. Lett. A **374**, 3671 (2010).

[98] J. T. Luo, Y. Z. Li, X. Y. Kang, F. Zeng, F. Pan, P. Fan, Z. Jiang, Y. Wang, J. Alloys Compd. **586**, 469 (2014).

[99] G. Kresse and H. Hafner, Phys. Rev. B **47**, 558 (1993).

[100] G. Kresse and J. Furthmuller, Comput. Mater. Sci. **6**, 15 (1996).

[101] R. Long and N. J. English, Phys. Rev. B **80**, 115212 (2009).

[102] J. O-Guillén, S. Lany, S. V. Barabash, and A. Zunger, Phys. Rev. Lett. **96**, 107203 (2006).

[103] W. H. Press, B. P. Flannery, S. A. Teukolsky, and W. T. Vetterling, New Numerical Recipes (Cambridge University Press, New York, 1986).

[104] Z. Xie, H. Wang, G. Liu, W. Yang, L. Lin, J. Y. Fang, and L. An, J. Phys. Chem. C **111**, 17169 (2007).

[105] C. Stampfl and C. G. Van de Walle, Phys. Rev. B **65**, 155212 (2002).

[106] Á. Szabó, N. T. Son, E. Janzén, and A. Gali, Appl. Phys. Lett. **96**, 192110 (2010).

[107] K. Yang, R. Wu, L. Shen, Y. P. Feng, Y. Dai, and B. Huang, Phys. Rev. B **81**, 125211 (2010).

[108] Y. Zhang, W. Liu, and H. Niu, Phys. Rev. B **77**, 035201 (2008).

[109] R. Han, W. Yuan, H. Yang, X. Du, Y. Yan, and H. Jin, J. Magn. Mag. Mat. **326**, 45 (2013).

[110] H. Jin, Y. Dai, B. Huang and M. -H. Whangbo, Appl. Phys. Lett. **94**, 162505 (2009).

[111] G. Ciatto, A. Di Trolio, E. Fonda, L. Amidani, F. Boscherini, M. Thomasset, P. Alippi, and A. A. Bonapasta, Appl. Phys. Lett. **101**, 252101 (2012).

[112] M. C. Munoz, S. Gallego, and N. Sanchez, Joint European Magnetic Symposia (Jems) **303**, 012001 (2011).

[113] M. S. Miao, A. Janotti, and C. G. Van de Walle, Phys. Rev. B **80**, 155319 (2009).

[114] M. C. Muñoz, S. Gallego and N. Sanchez, J. Phys.: Conf. Ser. **303**, 012001 (2011).

[115] S. Chen, N. V. Medhekar, J. Garitaonandia, and K. Suzuki, J. Phys. Chem. C, **116** 8541 (2012).

[116] P. Panigrahi, T. Hussain, C.M. Araujo and R. Ahuja, J. Phys.: Condens. Matter **26**, 265801 (2014).

[117] G. P. Srivastava, Rep. Prog. Phys. **60**, 561 (1997).

[118] M. D. Pashley, Phys. Rev. B **40**, 10481 (1989).

[119] X. Huang, E. Lindgren, and J. R. Chelikowsky, Phys. Rev. B **71**, 165328 (2005).

[120] G. Fischer, N. Sanchez, W. Adeagbo, M. Lüders, Z. Szotek, W. M. Temmerman, A. Ernst, W. Hergert, and M. C. Muñoz, Phys. Rev. B **84**, 205306 (2011).

[121] S. Pal, T. Jasper-Tönnies, M. Hack, and E. Pehlke, Phys. Rev. B **87**, 085445 (2013).

[122] W. -J. Lee, Y. -S. Kim, Phys. Rev. B **84**, 115318 (2011).

Electronic and magnetic properties of alkali and alkaline earth metals doped AlN: bulk to surfaces

SANDHYA CHINTALAPATI

NATIONAL UNIVERSITY OF SINGAPORE

2015